University of Louisville
ThinkIR: The University of Louisville's Institutional Repository

Electronic Theses and Dissertations

5-2014

Next generation RFID telemetry design for biomedical implants.

Andre Johan Faul
University of Louisville

Follow this and additional works at: https://ir.library.louisville.edu/etd

Part of the Electrical and Computer Engineering Commons

Recommended Citation
Faul, Andre Johan, "Next generation RFID telemetry design for biomedical implants." (2014). *Electronic Theses and Dissertations.* Paper 428.
https://doi.org/10.18297/etd/428

This Doctoral Dissertation is brought to you for free and open access by ThinkIR: The University of Louisville's Institutional Repository. It has been accepted for inclusion in Electronic Theses and Dissertations by an authorized administrator of ThinkIR: The University of Louisville's Institutional Repository. This title appears here courtesy of the author, who has retained all other copyrights. For more information, please contact thinkir@louisville.edu.

المنارة للاستشارات

www.manaraa.com

NEXT GENERATION RFID TELEMETRY DESIGN FOR BIOMEDICAL IMPLANTS

By

Andre Johan Faul

BEng (Electronic Engineering), University of Pretoria, 1983

BEng Hons (Electronic Engineering), University of Pretoria, 1987

A Dissertation

Submitted to the Faculty of the

J.B. Speed School of Engineering of the University of Louisville

in Partial Fulfillment of the Requirements for the Degree of

Doctor of Philosophy

Department of Electrical and Computer Engineering

University of Louisville

Louisville, Kentucky

May 2014

المنارة للاستشارات

www.manaraa.com

المنارة للاستشارات
www.manaraa.com

NEXT GENERATION RFID TELEMETRY DESIGN FOR BIOMEDICAL IMPLANTS

By

Andre Johan Faul

BEng (Electronic Engineering), University of Pretoria, 1983

BEng Hons (Electronic Engineering), University of Pretoria, 1987

A Dissertation Approved on

April 9, 2014

by the following Dissertation Committee:

_____
John Naber (Dissertation Director)

_____
Kevin Walsh

_____
Bruce Alphenaar

_____
William Hnat

_____
Robert Keynton

المنارة للاستشارات
www.manaraa.com

DEDICATION

This dissertation is dedicated to my lovely wife Annatjie and my four wonderful children, Andre, Madri, Christiaan and Leonard, and to my mother, Leonore. Your patience and support helped me to finally complete this work.

المنارة للاستشارات
www.manaraa.com

ACKNOWLEDGEMENTS

I would like to express my sincere thanks to my dissertation chair and mentor, Dr. John Naber, for his patience and countless hours of helping me in my research. I would like to thank my committee members, Dr. Kevin Walsh, Dr. Bruce Alphenaar, Dr. Robert Keynton and Dr. Bill Hnat for their input and suggestions. I appreciate the detailed and valuable comments that Dr. Hnat made on my dissertation.

My work would have been much more difficult if I did not receive selfless help from a number of people. Doug Jackson spent several hours manufacturing the small antennas and other printed circuit boards that I needed. Doug and Chris Isert also provided valuable technical input. Dr. Julia Aebersold, Dr. Kevin Walsh and Joseph Lake helped me to master the ball-bonding machine and Tommy Roussel kept the server running so that I could perform the antenna simulations and circuit design. To all my utmost thanks and appreciation.

المنارة للاستشارات
www.manaraa.com

ABSTRACT

NEXT GENERATION RFID TELEMETRY DESIGN FOR BIOMEDICAL IMPLANTS

Andre J. Faul

April 9, 2014

The design and development of a Radio Frequency Identification (RFID) based pressure-sensing system to increase the range of current Intra-Ocular Pressure (IOP) sensing systems is described in this dissertation. A large number of current systems use near-field inductive coupling for the transfer of energy and data, which limits the operational range to only a few centimeters and does not allow for continuous monitoring of pressure. Increasing the powering range of the telemetry system will offer the possibility of continuous monitoring since the reader can be attached to a waist belt or put on a night stand when sleeping.

The system developed as part of this research operates at Ultra-High Frequencies (UHF) and makes use of the electromagnetic far field to transfer energy and data, which increases the potential range of operation and allows for the use of smaller antennas. The system uses a novel electrically small antenna (ESA) to receive the incident RF signal. A four stage Schottky circuit rectifies and multiplies the received RF signal and provides DC power to a Colpitts oscillator. The oscillator is connected to a pressure sensor and

المنارة للاستشارات
www.manaraa.com

provides an output signal frequency that is proportional to the change in pressure. The system was fabricated using a mature, inexpensive process.

The performance of the system compares well with current state of the art, but uses a smaller antenna and a less expensive fabrication process. The system was able to operate over the desired range of 1 m using a half-wave dipole antenna. It was possible to power the system over a range of at least 6.4 cm when the electrically small antenna was used as the receiving antenna.

المنارة للاستشارات
www.manaraa.com

TABLE OF CONTENTS

ACKNOWLEDGEMENTS iv

ABSTRACT v

LIST OF TABLES x

LIST OF FIGURES xii

CHAPTER 1. INTRODUCTION 1

1.1 Motivation..... 1

1.2 General Discussion of Wireless Implantable Technology 3

1.3 Design Limitations 8

1.4 Design method 8

1.5 Novelty of this work 9

1.6 Research purpose 9

CHAPTER 2. BACKGROUND: IMPLANTABLE DEVICES USING RFID 10

2.1 Introduction 10

2.2 Near Field Devices 12

2.3 Far Field Devices..... 13

2.4 RF Rectification 17

2.5 Electrically Small Antennas 19

CHAPTER 3. RFID THEORY 25

3.1 Introduction 25

المنارة للاستشارات
www.manaraa.com

3.2 Electrically small antennas 33

3.3 RF rectification 36

3.4 Oscillators 38

CHAPTER 4. OSCILLATOR LOCK-IN 40

4.1 Background 40

4.2 Oscillator designs and lock-in tests 42

CHAPTER 5. ESA DESIGN AND DEVELOPMENT 50

5.1 Background 50

5.2 Design and simulation 50

5.3 Half-wavelength Dipole Antennas 51

5.4 Electrically Small Antennas 55

5.4.1 Commercial RFID System Evaluation 56

5.4.2 ESA design and development 60

5.4.3 Commercial antenna tests 82

CHAPTER 6. CIRCUIT DESIGN AND DEVELOPMENT 86

6.1 Application Specific Integrated Circuit (ASIC) Designs 86

6.2 Oscillator Design 88

6.2.1 Voltage Controlled Oscillator (VCO) 88

6.2.2 RC Multi-vibrator Oscillator 89

6.2.3 Colpitts Oscillator 90

6.2.4 Spiral Inductor Characterization 98

6.2.5 Discrete Oscillator 101

6.3 Energy Harvesting Circuit Design 104

6.3.1 ASIC 1: Schottky and MOSFET rectifier/multiplier implementation .. 106

6.3.2 ASIC 2 – Multi-stage Greinacher rectifier circuits. 115

المنارة للاستشارات
www.manaraa.com

6.3.3 ASIC 3 – Multi-stage Dickson Rectifier Circuits 120

6.4 Voltage Regulator 135

6.4.1 Background 135

6.4.2 Simulation and Layout 136

CHAPTER 7. SYSTEM TESTING AND RESULTS 144

7.1 IC pin layout and bonding diagram 144

7.2 Final Circuit Testing 146

7.2.1 Dickson rectifier/multiplier and regulator 146

7.2.2 Spiral inductor 147

7.2.3 Colpitts oscillator 148

7.2.4 System performance 152

CHAPTER 8. CONCLUSION AND FUTURE WORK 159

8.1 Conclusion 159

8.2 Future work 161

REFERENCES 162

CURRICULUM VITAE 168

المنارة للاستشارات
www.manaraa.com

LIST OF TABLES

Table 1. Comparison of RFID telemetry systems. 11

Table 2. Rectifier Performance. 19

Table 3. Comparison of simulated and measured dipole antenna parameters. 53

Table 4. Reading distance of Alien IC with different antenna configurations. 59

Table 5. Comparison of simulated and measured parameters of ESA's. 61

Table 6. Comparison of simulated and measured antenna parameters. 63

Table 7: Measured ESA parameters and performance. 67

Table 8. Antenna (b) characteristics during tuning. 68

Table 9. Antenna (d) characteristics during tuning. 69

Table 10. Theoretical, Simulated and measured Q for antennas (a) and (d). 75

Table 11. Capacitance vs resistance values for RC oscillator. 90

Table 12. Spiral inductor characteristics. 101

Table 13. Comparison of simulated and measured oscillator parameters. 103

Table 14. Direct RF-to-DC conversion test results. 113

Table 15. Radiated RF-to-DC conversion test results. 114

Table 16. Eight-stage Greinacher half-wave rectifier test results. 118

Table 17. Eight-stage Greinacher half-wave rectifier with impedance match test results. 118

المنارة للاستشارات
www.manaraa.com

Table 18. Sixteen-stage Greinacher half-wave rectifier test results. 118

Table 19. DC output voltage at distances of 0.5 m and 1 m. 119

Table 20. Multi-stage Dickson rectifier circuit bonding table. 122

Table 21. RF-to-DC test results with circuit in PGA package..... 124

Table 22. DC voltage generated with circuit on 50 Ω test fixture. 125

Table 23. DC voltages generated with antennas oriented for maximum output..... 126

Table 24. DC output voltage of Dickson half-wave rectifiers. 128

Table 25. DC voltages measured across storage capacitor. 129

Table 26. Resistor values of regulator circuits..... 140

Table 27. Pin descriptions for test IC..... 145

Table 28. Oscillator output frequency and power with different inductors. 149

Table 29. Oscillation frequency and DC characteristics of Colpitts oscillator. 150

Table 30. Comparison of calculated, simulated and measured oscillator frequency..... 153

Table 31. Comparison of measured and calculated oscillator frequency. 156

Table 32. Oscillation frequency and output power vs powering distance. 157

Table 33. Comparison with current state of the art..... 160

المنارة للاستشارات
www.manaraa.com

LIST OF FIGURES

Figure 1. Typical RFID transponder architecture. 3

Figure 2. Power and data transmitted through inductive coupling using load modulation[12]. 6

Figure 3. Far-field RFID using backscatter modulation [12]. 7

Figure 4. CMOS Temperature sensing system [21]. 14

Figure 5. UHF RFID transponder and antenna[16]. 15

Figure 6. Wireless temperature sensor[17]. 15

Figure 7. Stent and implant showing discrete RF powering circuit[6]. 16

Figure 8. Intraocular pressure monitor with monopole antenna[7]. 16

Figure 9. Intraocular pressure and temperature sensor[19]. 17

Figure 10. Operating range versus antenna size for RFID telemetry systems 20

Figure 11. (a) Impinj "Button" antenna, (b) HF (3 – 30 MHz) antenna, (c) Alien Technology "Square Antenna", 22.5 mm x 22.5 mm, (d) Alien Technology "Squiggle" antenna, 95 mm x 8.2 mm. 21

Figure 12. Half of a meander line dipole shown[29]. 21

Figure 13. Gain versus area for optimized non-uniform meander line antennas – from 3 cm x 3 cm to 6 cm x 6 cm[29]. 22

المنارة للاستشارات
www.manaraa.com

Figure 14. Meander antenna iterations – (a)Reference antenna, Fr = 267 MHz; (b) Planar antenna 1, Fr = 295.3 MHz; (c) Planar antenna 2, Fr = 154.9 MHz.[30]. 23

Figure 15. Impedance matching through phase reversal[31]. 24

Figure 16. Source and transmission line with antenna showing detachment of electric field lines.[13]. 27

Figure 17. Range of commercial RFID devices[35]. 30

Figure 18. Performance limitation of RFID systems[40]. 32

Figure 19. Current distribution on wire dipoles[13]. 33

Figure 20. Two-stage Greinacher half-wave rectifier circuit. 37

Figure 21. Two-stage Dickson half-wave rectifier. 38

Figure 22. MOSFET Colpitts oscillator. 39

Figure 23. (a) RC multi-vibrator oscillator. (b) Colpitts oscillator. 43

Figure 24. (a) RC multi-vibrator oscillator layout. (b) Colpitts oscillator layout. 44

Figure 25. Multi-vibrator oscillator lock-in test setup. 44

Figure 26. RC multi-vibrator oscillator output showing lock-in. 45

Figure 27. Colpitts oscillator lock-in test setup. 46

Figure 28. Colpitts oscillator output. 46

Figure 29. RC multi-vibrator oscillator just before lock-in. 47

Figure 30. Colpitts oscillator output just before lock-in. 48

Figure 31. RC multi-vibrator lock-in frequencies and range. 49

Figure 32. Colpitts oscillator lock-in frequencies and range. 49

Figure 33. Time domain signal illustrating lock-in. 49

Figure 34. Dipole antenna layout, 3-D visualization and radiation pattern. 51

المنارة للاستشارات
www.manaraa.com

Figure 35. Folded dipole layout, 3-D visualization and radiation pattern. 52

Figure 36. Forward transmission parameters of dipole antenna showing resonant frequency and impedance at resonance..... 52

Figure 37. Forward transmission parameters of folded dipole antenna showing resonant frequency and impedance at resonance..... 53

Figure 38. 915MHz half-wavelength wire dipole antenna. 54

Figure 39. Wire half-wave dipole forward transmission parameters showing resonant frequency and input impedance. 55

Figure 40. Alien Technology's "Squiggle" tag and "Square" tag. 56

Figure 41. Alien Technology System Test Setup. 57

Figure 42. Modifications made to Alien Technology "Squiggle" antenna..... 58

Figure 43. Alien Technology IC connected to PCB antenna and variable capacitor. 58

Figure 44. Various electrically small antenna design configurations. 60

Figure 45. Meander antenna configurations fabricated on FR-4 PCB..... 61

Figure 46. Meander dipole designs. (a) Trace width – 50 µm, separation 200 µm. (b) Optimized for impedance match, trace width 200 µm, separation 200 µm. (c) Optimized for efficiency, trace width 200 µm, separation 500 µm. (d) Optimized for impedance match, trace width 200 µm, separation 200 µm..... 62

Figure 47: Antennas (b) and (d) after tuning to 915 MHz. 64

Figure 48. Electrically small antenna test setup..... 66

Figure 49: Fabricated ESA meander dipole antennas. 66

Figure 50. Antenna (b): Cuts made for tuning. 68

Figure 51. Antenna (d): Cuts made for tuning. 69

المنارة للاستشارات
www.manaraa.com

Figure 52. Received power at antenna (d) vs. transmit power..... 70

Figure 53. Simulated forward transmission parameters and impedance for antenna (d).. 71

Figure 54. Measured parameters for antenna (d) before (top) and after (bottom) tuning. 72

Figure 55. Antenna (a) Antenna (d)..... 73

Figure 56. Return Loss: Antenna (a) Antenna (d). 73

Figure 57. Return Loss: Antenna (a) Antenna (d). 74

Figure 58. Test setup to measure ESA performance with increased transmitter power... 77

Figure 59. DC voltage generated by multistage rectifiers 77

Figure 60. Antenna configuration (b) used in saline solution test. 78

Figure 61. MoM simulation results for antenna (b) in plastic. Substrate definition is shown on right..... 79

Figure 62. FEM simulation results for antenna (b) in plastic. Substrate definition is shown on right..... 80

Figure 63. Measured results for antenna (b) in plastic..... 80

Figure 64. MoM simulation results for antenna (b) in saline solution. Substrate definition is shown on right..... 81

Figure 65. FEM simulation results for antenna (b) in saline solution. Substrate definition is shown on right..... 81

Figure 66. Measured results for antenna (b) in saline solution..... 81

Figure 67. Comparison of measured and calculated received power for three different antennas..... 83

Figure 68. Received power vs angle and distance for the Yagi antenna. 84

Figure 69. Near-field measured and calculated received power vs distance. 85

المنارة للاستشارات
www.manaraa.com

Figure 70. Block diagram of implantable transponder. 86

Figure 71. System Design Process Flow..... 87

Figure 72. Voltage controlled oscillator circuit schematic. 88

Figure 73. RC Multivibrator oscillator schematic. 89

Figure 74. SAW based Colpitts oscillator circuit schematic. 91

Figure 75. Colpitts oscillator PCB layout. 91

Figure 76. Revised discrete Colpitts oscillator circuit schematic. 92

Figure 77. Discrete Colpitts oscillator output. 92

Figure 78. Quality factor of the different coils. 93

Figure 79. Magnitude and phase response of 50-turn coil. 94

Figure 80. Colpitts circuit schematic with NMOS transistor. 95

Figure 81. Loop gain(top) and phase(bottom) response of oscillator. 96

Figure 82. Simulated oscillator output. 97

Figure 83. Colpitts oscillator circuit used for IC layout. 97

Figure 84. IC Die with spiral inductor. 98

Figure 85. (a) Inductor S11 (b) Impedance. 99

Figure 86. Inductor equivalent circuit. 99

Figure 87. Inductor Layout in ADS. 100

Figure 88. ADS Inductor simulation results. 100

Figure 89. Discrete Colpitts oscillator schematic and output signal with spectrum. 102

Figure 90. Discrete Colpitts oscillator schematic with SMT components, output and spectrum. 102

المنارة للاستشارات
www.manaraa.com

Figure 91. Discrete Colpitts oscillator schematic with SMT components and transmission lines, PCB layout at right. 103

Figure 92. Kocer et al. sixteen stage voltage multiplier. 104

Figure 93. Three-stage CMOS rectifier schematic. 105

Figure 94. Single-stage full-wave CMOS rectifier. 105

Figure 95. Two-stage Greinacher Schottky half-wave multiplier boosting voltage to 700mV 107

Figure 96. Two-stage Greinacher MOSFET half-wave multiplier with decreased performance. 108

Figure 97. Four-stage Greinacher half-wave multiplier boosting signal to 1.4V. 109

Figure 98. Two-stage Dickson half-wave multiplier using Schottky diodes. 109

Figure 99. Two-stage Dickson half-wave multiplier using MOSFETs. 110

Figure 100. Two-stage Dickson full-wave Schottky multiplier 111

Figure 101. Two-stage Dickson full-wave MOSFET multiplier. 111

Figure 102. ASIC test circuit layout. 112

Figure 103. ASIC pin layout. 112

Figure 104. Worksheet screen shot of impedance matching utility. 115

Figure 105. Multi-stage Greinacher rectifier circuit schematic. 116

Figure 106. Multi-stage Greinacher rectifier circuit layout. 116

Figure 107. Rectifier circuit 50Ω Test fixture. 117

Figure 108. Test setup for measuring DC output voltage of rectifiers/multipliers. 117

Figure 109. Two-stage, half-wave Dickson rectifier circuit schematic. 120

Figure 110. Two-stage, full-wave Dickson rectifier circuit schematic. 121

المنارة للاستشارات
www.manaraa.com

Figure 111. Multi-stage Dickson rectifier circuit layout. 121

Figure 112. Rectifier 50Ω test fixture. 122

Figure 113. Direct RF-to-DC rectifier performance comparison. 123

Figure 114. Test setup for radiated RF-to-DC conversion: circuit in PGA package. 124

Figure 116. (a) IC die fixed to antenna PCB (b) Storage capacitor added. 127

Figure 117. Test setup for determining effect of multi-meter leads. 127

Figure 118. Test setup for measuring DC voltage across storage capacitor. 129

Figure 119. Potential range for powering of implantable device. 130

Figure 120. Test setup for measuring input voltage to rectifier. 131

Figure 121. Output voltage of ESA measured on oscilloscope. 131

Figure 122. Output power of ESA measured on spectrum analyzer. 132

Figure 123. Comparison of simulated and measured DC voltages at output of 4-stage Dickson rectifier. 133

Figure 124. DC voltage generated with distance between antennas, indoors and outdoors. 135

Figure 125. Regulator circuit schematic with voltage reference on the left and regulator on the right. R_ref and R_adj taken off-chip. 137

Figure 126. Simulated line regulation: regulated voltage with R_adj = R_ref = 100 kΩ. 137

Figure 127. Simulated line regulation: regulated voltage with R_adj = R_ref =68 kΩ.. 138

Figure 128. Simulated line regulation: regulated voltage with R_adj = R_ref =270 kΩ. 138

Figure 129. Simulated load regulation. 139

المنارة للاستشارات
www.manaraa.com

Figure 130. Measured line-regulation with different resistance values for Radj and Rref. 139

Figure 131. Regulator circuit layout. 141

Figure 132. Load regulation comparison. 141

Figure 133. Load regulation – Turner regulator [67]. 141

Figure 134. Line regulation comparison. 142

Figure 135. Regulator layout with Radj=114 kΩ and Rref = 114 kΩ. 142

Figure 136. Comparison of simulated and measured load regulation. 143

Figure 137. Comparison of measured and simulated line regulation. 143

Figure 138. Final test circuit layout. 144

Figure 139. Bonding diagram (IC 89274, MOSIS run V35G-AH). 145

Figure 140. Four-stage Dickson rectifier/multiplier. 146

Figure 141. Voltage regulator with reference. 146

Figure 142. Rectifier/regulator test setup. 147

Figure 143: Spiral inductor test setup. 148

Figure 144: Spiral inductor S11 measurements. 148

Figure 145. Colpitts oscillator circuit schematic. 149

Figure 146. Oscillator test setup. 150

Figure 147. Oscillator in eight pin package. 151

Figure 148. Colpitts oscillator power consumption. 151

Figure 149. Oscillator powered from dipole antenna. 152

Figure 150. Measured oscillator output spectrum. 153

Figure 151. Simulated spectra: (a) Harmonic balance (b) Transient analysis. 153

المنارة للاستشارات
www.manaraa.com

Figure 152. Colpitts oscillator output power vs range. 154

Figure 153. Final packaged die test configuration. 155

Figure 154. Comparison of calculated and measured oscillation frequencies. 156

Figure 155. System test setup in metal container. 157

Figure 156. Test setup to determine powering and sensing range. 158

Figure 157. Oscillation frequency with changing pressure. 158

Figure 158. Size of ESA compared to half-wave dipole and a penny. 159

المنارة للاستشارات
www.manaraa.com

CHAPTER 1. INTRODUCTION

1.1 Motivation

An implantable transponder to extend the range of current Radio Frequency Identification (RFID) based telemetry systems for wireless monitoring of physiological parameters in humans and animals was designed and developed. The main focus of this research is to explore increasing the range of an existing High Frequency (HF) RFID system from 5 cm to at least 60 cm by moving to Ultra-High Frequencies (UHF). This research will advance the current state of the art that has been demonstrated using both Low Frequency (LF – 125 kHz) and High Frequency (HF – 13.56 MHz) RFID in applications such as continuous monitoring of intraocular pressure (IOP), monitoring spinal fusion progress, neural recording, and sub-retinal prostheses [1-4].

Most of the RFID-based biomedical telemetry systems make use of inductive coupling for power and data transmission in the low-to-high frequency range (125 KHz to 13.56 MHz). However, these systems are limited in their operating range since the reader and implant must be in close proximity to each other so that near-field magnetic coupling between the two antennas can take place. The distance between the reader located outside the body and the implant is limited to a few centimeters for antennas on the order of 6mm in diameter. On the other hand, RFID Systems operating at UHF,

المنارة للاستشارات
www.manaraa.com

915 - 2450 MHz, make use of the electric field in the far-field to provide power and data, which can potentially increase the range to over 60 cm as compared to similar sized antennas operating in the low frequency, near-field region. The key motivation to increase the range in RFID telemetry systems is to make possible the prospect for continuous monitoring of physiological parameters by allowing the patient to wear the reader on their belt or even place the reader next to a bed-side table for continuous night-time monitoring. Wireless far-field RFID technology can also be applied to the monitoring of bladder pressure and various cardiac pressures. A much longer-term potential application is to incorporate the sensor and UHF RFID telemetry circuitry and antenna within the confines of a stent.

The transponder is a passive device in the sense that it contains no battery and is powered by harvesting energy from the incident RF signal from the reader. The energy harvested is used to power an oscillator that transmits a signal back to the reader. The frequency of the signal transmitted by the transponder is proportional to the pressure being sensed. A block diagram of a typical RF transponder is shown in Figure 1.

المنارة للاستشارات
www.manaraa.com

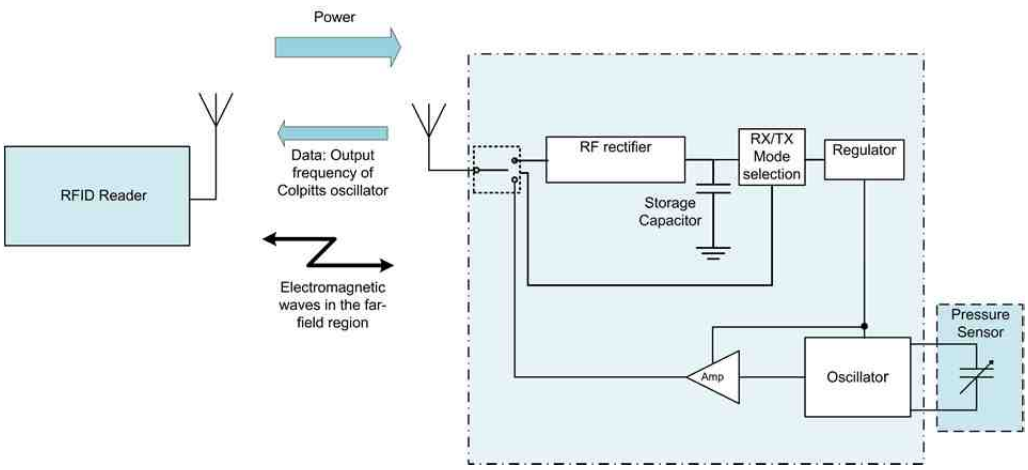

Figure 1. Typical RFID transponder architecture.

1.2 General Discussion of Wireless Implantable Technology

Current wireless implantable systems vary widely in terms of the technology being used and the operating frequency. Some of the wireless implantable systems that have recently been developed include wireless systems to record neural activity [2], continuously monitor blood glucose levels [5], monitor cardiovascular pressure [6], and monitor intraocular pressure [7]. The first two systems both make use of inductive coupling for power transfer and data communications while the latter two systems use RF energy for powering and data transfer. Systems have also been developed that make use of hybrid technology where power is delivered through inductive coupling and data is transmitted using RF signals [8].

Sensors that have been used to indicate changes in intra-ocular pressure include strain-gauge sensors and capacitive pressure sensors. Strain gauge sensors are typically used for non-invasive applications where the sensor is incorporated in soft contact lenses that can detect micrometer changes in the surface on which it is placed [9]. Micro-Electro-Mechanical-Systems (MEMS) capacitive pressure sensors are mostly used in

المنارة للاستشارات
www.manaraa.com

invasive applications where the sensor is placed in a fluid and can detect minute changes in pressure. The system described in this paper uses a MEMS capacitive pressure sensor where the transponder is placed into a lens during cataract surgery or under the sclera for Glaucoma treatment.

Implantable telemetry systems can generally be divided into two categories: near-field and far-field devices. These categories refer to the electromagnetic fields generated by the antennas. The near-field is typically defined as the region where the maximum radiated and reactive powers are equal. Although only two regions are traditionally defined in RFID systems, the space surrounding the antenna is more accurately divided into three regions [10]:

- The reactive near-field exists from the antenna to a distance of approximately $0.62\sqrt{D^3/\lambda}$, where D is the maximum dimension of the antenna and λ is the wavelength of the signal.
- The radiating near-field is defined as the distance of approximately $0.62\sqrt{D^3/\lambda}$ to $2D^2/\lambda$ from the antenna.
- The far-field is defined as the distance greater than $2D^2/\lambda$ from the antenna.

For antennas that have a maximum overall dimension that is very small compared to the wavelength, the radiating near-field region might not exist; therefore, only the near-field and far-field regions are used for most practical RFID applications. The range of the near-field region is approximated by $\lambda/2\pi$ for dipole type antennas and is traditionally used as the border between the near-field and far-field regions for RFID.

المنارة للاستشارات
www.manaraa.com

Near-field devices operate on the principle of mutual inductance between the transducer coil and the antenna of the reader. The reader antenna and the implant device coil must therefore be in close proximity to each other so that magnetic field coupling occurs. The reading range of inductively coupled systems is therefore typically only a few centimeters. In a purely inductive telemetry system, power is delivered to the transducer by inductive coupling, and data is transmitted to the reader by a method referred to as load modulation.

Some of the earlier near-field devices made use of very simple inductor-capacitor (L-C) resonant circuits to measure intraocular pressure [11]. The transducer consisted of two flat spiral coils spaced a small distance apart. Any change in the distance between the coils causes a change in the resonant frequency of the circuit. A grid-dip oscillator that acted as the reader detected the change in resonant frequency. The device had a maximum read range of only 12 mm and showed very poor long term stability. A block diagram of a near-field RFID system that makes use of the concept of inductive coupling is shown in Figure 2.

المنارة للاستشارات
www.manaraa.com

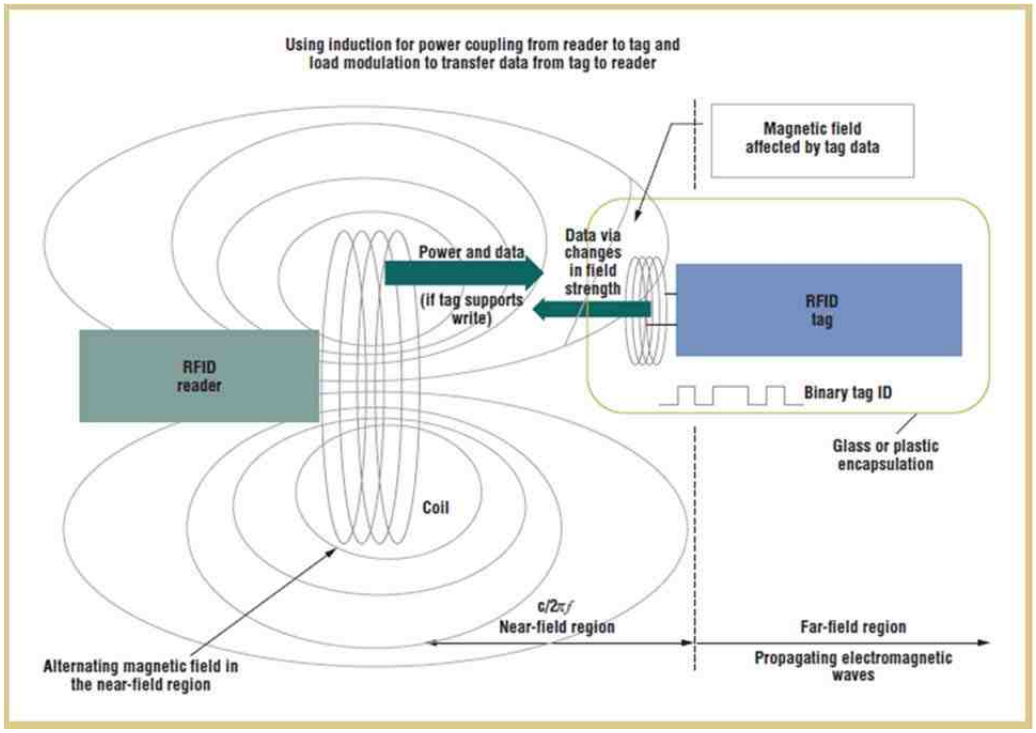

Figure 2. Power and data transmitted through inductive coupling using load modulation[12].

In hybrid inductive telemetry systems, power is delivered to the transducer via inductive coupling and data is transferred using RF links. The operating range of the hybrid inductive telemetry systems is limited by the inductively coupled power transfer. The two coils used for inductive coupling must also be oriented such that the axes of both coils coincide for maximum power transfer to occur.

Far-field devices make use of the radiated electromagnetic waves to transfer energy and data as illustrated in Figure 3. The far-field device in Figure 3 illustrates the method of electromagnetic (EM) backscatter by which the data is transferred from the transponder to the reader. Backscatter modulations operates on the principle that when an electromagnetic signal is incident on a conducting surface (antenna) that corresponds in size to a fraction of the wavelength of the signal, the incident signal will cause currents to

المنارة للاستشارات
www.manaraa.com

flow in the antenna. The currents result in standing waves on the surface of the antenna and re-radiation of a portion of the incident signal. The "backscattered" signal is modulated by changing the impedance of the RFID transponder that is attached to the antenna.

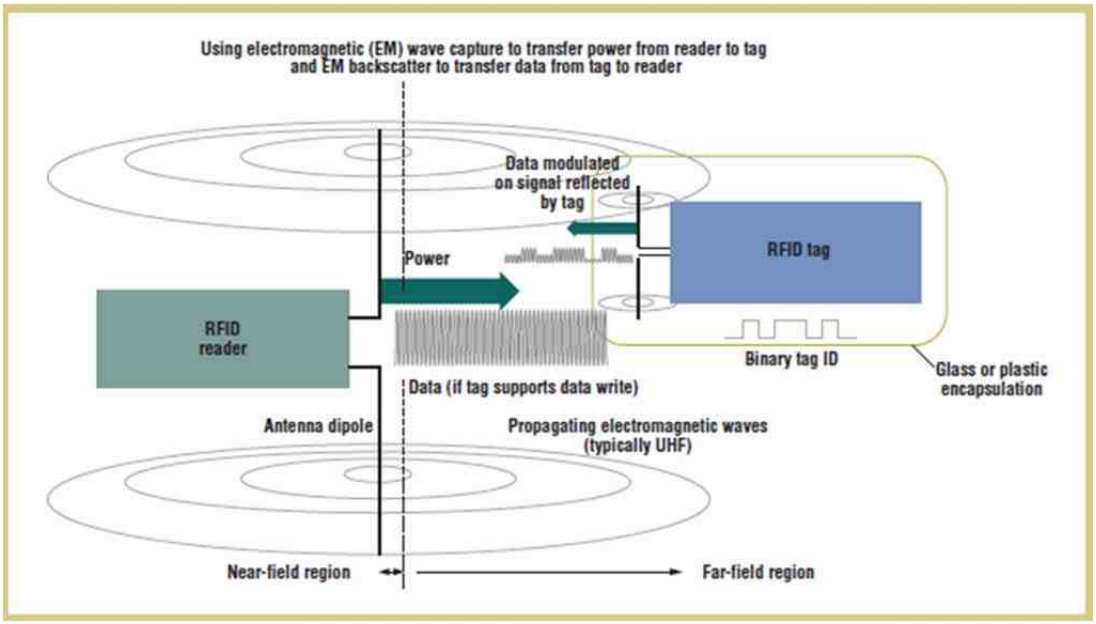

Figure 3. Far-field RFID using backscatter modulation [12].

Other methods exist where the data is transferred back to the reader by using a transmitter or oscillator on the transponder. The oscillator can be either an active oscillator that makes use of transistors or a passive oscillator that makes use of surface acoustic wave (SAW) devices. Technical details of the different far-field RFID systems will be discussed in Chapter 3.

المنارة للاستشارات
www.manaraa.com

1.3 Design Limitations

The proposed next generation system must be able to remotely power the implantable device using a license free frequency of 2450 MHz or 915 MHz and must be able to read the data from the device using the same frequency band. The transponder, including antenna, must be smaller than 9 x 6 mm and the system must be able to operate over a minimum distance of 60 cm using 1 Watt of transmitted power. The transponder described in this paper has been designed to operate at a frequency of 915 MHz. The frequency of 915 MHz was chosen because it falls within the 902 MHz to 928 MHz ISM (Industrial, Scientific and Medical) band of unlicensed frequencies and because a longer range is achieved with 915 MHz as opposed to 2.45 GHz. The longer range is due to free space attenuation that is proportional to the square of the wavelength of a signal. A longer wavelength signal (915 MHz) will suffer less free space attenuation over the same distance than a shorter wavelength signal (2.45 GHz.)

1.4 Design method

The limitations mentioned in section 1.3 are met by the design, simulation and fabrication of an Application Specific Integrated Circuit (ASIC) RFID transponder operating at a frequency of 915 MHz. Power for the transponder is derived from an energy harvesting system that contains a Radio Frequency (RF) to Direct Current (DC) converter and voltage multiplier circuit. A voltage regulating circuit that provides power for the transponder follows after the voltage multiplier. A Colpitts oscillator that is connected to a pressure sensor provides a real time indication of the pressure. The pressure sensor forms part of the tank circuit of the oscillator. A change in pressure will

المنارة للاستشارات
www.manaraa.com

therefore directly affect the operating frequency of the oscillator. The output of the oscillator is sent to an antenna that has been designed to resonate at 915 MHz and fits into an area 9 by 6 mm.

1.5 Novelty of this work

Although some studies found in the literature show an effective range in excess of 1m, none of the systems use an electrically small antenna. Far-field RFID telemetry systems that have been reported in the literature show a range of only several centimeters where antennas with sizes smaller than 54 mm^2 have been used. The aim of the proposed system is to wirelessly measure pressure in different parts of the body and to transmit the data over a distance of at least 60 cm using a transponder antenna size of 54 mm^2 and a reader power of 1 W.

1.6 Research purpose

The purpose of this study was to develop a battery-free, wireless implantable system to measure pressure in the eye. Regular monitoring of intraocular pressure is necessary for the treatment of Glaucoma, which is an eye disease that is characterized by elevated intra-ocular pressure. An estimated 60 million people worldwide suffer from Glaucoma, and the National Institutes of Health (NIH) estimates that 2 million Americans have the disease but do not know it. A wireless system provides the capability for continuous monitoring of intraocular pressure, which is currently not possible with the tonometry-based methods that are performed in clinician's offices.

المنارة للاستشارات
www.manaraa.com

CHAPTER 2. BACKGROUND: IMPLANTABLE DEVICES USING RFID

2.1 Introduction

The use of implantable medical devices has increased dramatically over the past few decades. These devices are used in various applications that include diagnostics, remote patient monitoring, surgical and to measure physiological parameters. Initially such implantable devices were connected to the monitoring devices by numerous wires. Advancements in electronics have made wireless implementation possible and decreased the physical size of electrical devices to the extent that they can easily be implanted in various places in the body. RFID implantable devices can broadly be classified into near-field (inductively coupled) and far-field (Electromagnetic wave coupled) devices. Near-field devices are limited by the range of the magnetic field, which is generally accepted to fall within a range that is less than $\lambda/2\pi$, where lambda is the wavelength of the signal and $\lambda = c/f$, with c = speed of light and the f = frequency in Hz [13]. Lower frequencies are favored for near-field systems since they have a longer wavelength and therefore a larger near-field range. At 915 MHz, the near field range is less than 52 mm. The far-field region is considered to be where the range is much greater than $\lambda/2\pi$. Table 1 summarizes some recent RFID systems including implantable devices.

المنارة للاستشارات
www.manaraa.com

Table 1. Comparison of RFID telemetry systems.

Ref	Lead Author Pub Year	Telemetry approach	Data freq	Power freq	Antenna size	Range/Reader power	Sensor
Near-field (Inductive coupling)							
[1]	Aebersold 2008	Inductive coupling	2.5 kHz	13.56 MHz	6 mm dia	1 cm	Capacitive pressure
[14]	Opasjumruskit 2006	Inductive coupling	125 kHz	125 kHz	27 mm dia	10 cm	PTAT Temperature
[8]	Graichen 2007	Hybrid	150 MHz	4 kHz	6 mm dia x 30 mm (power) 12 mm dia (data)	2- 3 cm 50 cm (data)	Strain gauges
[5]	Ahmadi 2009	Inductive coupling	13.56 MHz	13.56 MHz	4 x 8 mm	4 cm	Glucose sensor
Far-field (Electromagnetic wave coupling)							
[15]	Kocer 2006	RF	900 MHz	450 MHz	Commercial whip antenna	18.3 m (7 W)	CMOS Temp.
[16]	Karthaus 2003	RF backscatter	869 MHz	869 MHz	±50 x 50 mm	4.5 m (0.5 W)	None
[17]	Vaz 2010	RF backscatter	868 MHz	868 MHz	167 mm dipole	2 m (2 W)	CMOS temp
[6]	Chow 2010	RF	2.4 GHz	3.7 GHz	Stent – 30 mm	10 cm (3.2 W)	MEMS capacitive pressure
[7]	Chow 2010	RF	2.4 GHz	3.65 GHz	20 mm monopole	10 cm (0.9W) 50 cm (data)	Capacitive pressure
[18]	Kubendran 2011	RF	N/A	2.4 GHz	Printed square loop at 2.4 GHz	22 cm	Capacitive pressure
[19]	Yi-Chun 2011	RF backscatter	2.4 GHz	2.4 GHz	1 cm diameter loop	1.5 cm	Pressure/ temperature
[20]	Radiom 2010	RF	N/A	5.8 GHz	On chip antenna at 5.8 GHz	7.5 cm (4 W EIRP)	N/A
	This work	RF	915 MHz	915 MHz	Goal: 9 x 6 mm	Goal: 1m (1W)	Capacitive pressure

المنارة للاستشارات
www.manaraa.com

2.2 Near Field Devices

Aebersold et al. [1] were able to wirelessly measure the intraocular pressure of a rabbit using a 13.56 MHz reader to inductively power the transducer. The transducer consists of a MEMS capacitive pressure sensor that forms part of a RC multi-vibrator oscillator. The varying pressure changes the capacitance of the sensor and thereby the frequency of oscillation. The output of the oscillator is sent to a frequency divider and the output of the divider is transmitted to the reader as a 2.5 kHz signal. The instantaneous frequency of the 2.5 kHz signal corresponds to the pressure being measured. The main drawback of this system is the limited read range. The system is only able to consistently measure pressure at a maximum distance of 1 cm.

Opasjumruskit et al. [14] developed a temperature sensor for implantation in animals that makes use of inductive coupling to deliver power to the device and uses backscattering to deliver temperature data to the reader. The system operates at a frequency of 125 kHz for transmission of power and data. The sensor transponder makes use of a 27 mm diameter antenna coil to receive power and data from the reader and transmit data to the reader. The sensor was powered at a distance of 10 cm using a 60 mm diameter reader antenna coil and the read range was increased to 25 cm when a larger square reader antenna of 80 mm x 100 mm was used. The system also suffers from a limited read range.

A hybrid system for in vivo load measurement of orthopedic implants is described by Graichen et al. [8]. The system uses a low frequency of 4 kHz to power the implant. The low frequency is used to facilitate power transfer through the metal implant. A separate single loop antenna is used to transmit the strain gauge data to the reader at a

المنارة للاستشارات
www.manaraa.com

frequency of 150 MHz. The higher frequency for the data results in a data read range of almost 50 cm, but the overall system performance is limited by the 3cm maximum range for delivery of power.

Ahmadi and Jullien [5] developed an inductively coupled implantable telemetry system to continuously monitor blood glucose levels. The transducer is powered using a 13.56 MHz signal to power the transducer and load modulation is used to transmit the data back to the reader. The system has a limited read range of 4 cm.

2.3 Far Field Devices

Far-field device circuits typically include radio frequency (RF) to direct current (DC) conversion, regulation, modulation, transmission, and the sensor. Since these systems operate on the principle of using the RF energy to power the device and transmit data, they can operate over longer distances. Some of the recent developments in long range RFID systems are discussed below.

Kocer and Flynn [15, 21] developed a temperature sensing system that uses a 450 MHz signal to power the transducer and either 900 MHz or 2.3 GHz for data transmission from the transducer as shown in Figure 4. The system is powered by rectifying the incident 450 MHz signal using a cascaded arrangement of Cockcroft-Walton voltage multiplier circuits. An on-chip injection-locked voltage controlled oscillator (VCO) is used to extract a reference clock signal from the incident RF signal. A complementary to absolute temperature (CTAT) bias generator provides a control voltage for the VCO. A commercial antenna was used in the tests and it is unclear how the system will perform with an electrically small antenna. The system was tested in an anechoic chamber and a

المنارة للاستشارات
www.manaraa.com

theoretical range of 18.3 m was calculated based on a 7W transmit power. The suitability of the system for implantation was not discussed.

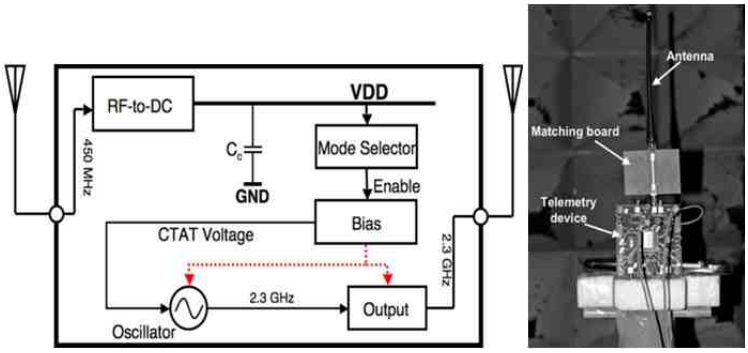

Figure 4. CMOS Temperature sensing system [21].

Karthaus and Fischer [16] developed an integrated RFID transponder with a theoretical operating range of 9.25 m using a 4 W, 915 MHz signal to power the transponder as shown in Figure 5. Power is delivered to the transponder by rectifying the incoming signal using a Schottky based voltage multiplier circuit. Communication back from the transponder is achieved using a backscatter method. The backscatter method works on the principle that the incident RF signal creates a current in the transponder antenna; therefore, a weak signal is radiated out (scattered back) from the transponder. Changing the input impedance of the transponder modulates the signal. A fairly large printed loop antenna was used for the transponder and miniaturization of the antenna was not discussed. Specific measurements of the transponder antenna are not given, but using the picture of the antenna, it is estimated to be approximately 50 mm x 50 mm.

المنارة للاستشارات
www.manaraa.com

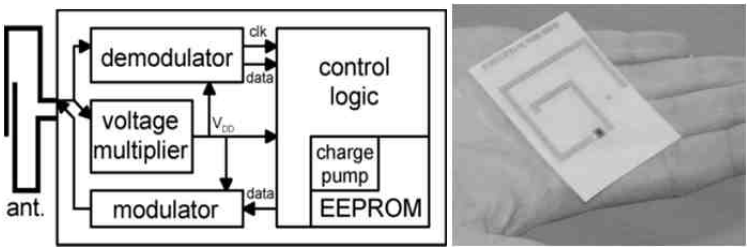

Figure 5. UHF RFID transponder and antenna[16].

Vaz et al. [17] have demonstrated the implementation of an UHF temperature transponder suitable for human body temperature monitoring. The system provides high accuracy (±0.1ºC) temperature measurement over a measured range of 2m using a 2W, 868 MHz signal to power the device. A Cockcroft-Walton (also referred to as Greinacher) voltage multiplier circuit is used to rectify the incident RF signal and provide DC power to the transponder. Data is transmitted from the transponder back to the reader using back-scatter modulation. The range reported does not take into account any attenuation of the signal by the body. A fairly large dipole antenna connected to the transducer is used and the effect of using a smaller antenna is not discussed. A circuit schematic of the system and a picture of the dipole antenna are shown in Figure 6.

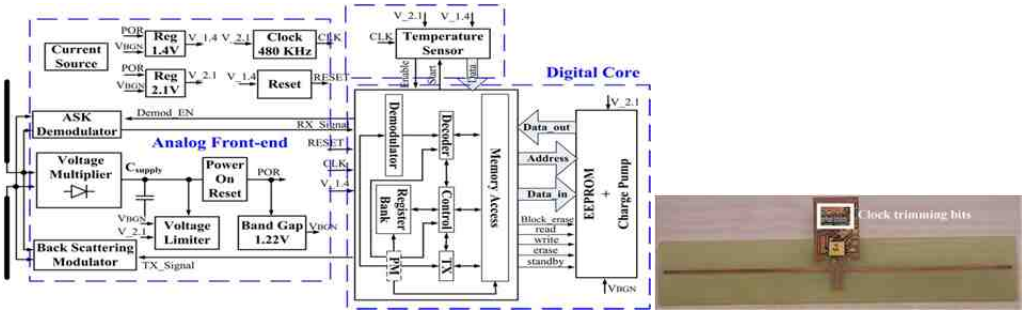

Figure 6. Wireless temperature sensor[17].

Various types of implantable devices were developed by Chow et al. [6, 7, 22]. All of their work makes use of frequencies in the GHz range. They developed an implantable cardiovascular pressure monitor that is integrated with a stent as show in Figure 7. A frequency of 3.7 GHz is used to wirelessly power the implant. The stent, with

المنارة للاستشارات
www.manaraa.com

a length of 30mm, is used as the antenna [6]. Even with this large antenna, and using a transmit power of 3.2 W, they were only able to achieve an operating range of 10cm using discrete components for the RF rectifying circuitry. They were not able to develop a fully integrated system that is able to provide enough power for the rest of the circuit to operate.

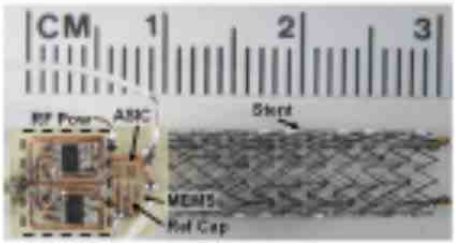

Figure 7. Stent and implant showing discrete RF powering circuit[6].

Chow et al. also developed an implantable system for measuring intraocular pressure [7] as shown in Figure 8. The system uses a frequency of 2.4 GHz for data transmission and 3.65 GHz for power delivery. A transmit power of 3.4 W was used to achieve an operating distance of 10 cm. The system uses a 20 mm monopole antenna for the implantable device.

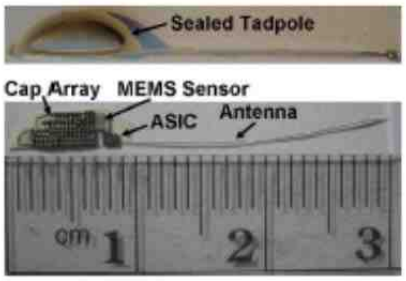

Figure 8. Intraocular pressure monitor with monopole antenna[7].

A low power wireless intraocular pressure and temperature sensing transponder was developed by Yi-Chen et al.[19]. The transponder consumes only 2.3 μW at 1.5 V during continuous monitoring of pressure and temperature. The system operates at a

المنارة للاستشارات
www.manaraa.com

frequency of 2.4 GHz and uses a 1 cm diameter loop antenna for the implant. Data from the implant is transferred to the reader by making use of Intermediate Frequency (IF) modulated backscatter. They were able to wirelessly operate the transponder through 4 mm of pork tissue, but were only able to achieve an operating range of 1.5 cm. A block diagram of the implant is shown in Figure 9.

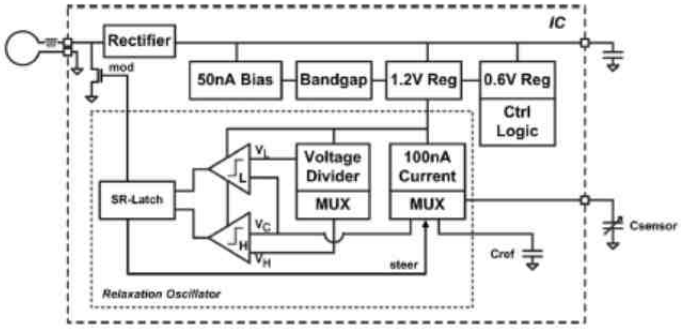

Figure 9. Intraocular pressure and temperature sensor[19].

2.4 RF Rectification

The most critical part of far-field wireless implantable transponder operation is RF powering of the device and is the limiting factor in determining the effective operating range of implantable transponders, since a low-power signal must be used to power up the device. Effective capturing of the incoming RF signal as well as efficient RF-to-DC conversion is therefore essential.

Curty et al. [23, 24] defines two efficiencies associated with rectifier circuits:

a. Conversion efficiency is given by

$$\eta_c = \frac{dc\ Output\ Power}{Incident\ RF\ power - Reflected\ RF\ power} \tag{2.1}$$

b. Overall efficiency is given by

المنارة للاستشارات
www.manaraa.com

$$\eta_o = \frac{dc\ Output\ Power}{Incident\ RF\ power} \tag{2.2}$$

The dc output power is given by $P_{dc} = V_{out}I_{out} = 4N\overline{V_D}I_{out}$, where N is the number of rectifying stages, V_D is the junction voltage of the diode and I_{out} is the current delivered to the load. The overall efficiency is not a very useful value since it considers the rectifier and antenna as one entity and does not give a true indication of the performance of the rectifier circuit. The result is very poor efficiency ratings particularly in situations where electrically small antennas are used. The conversion efficiency, as defined above, is also not particularly useful in this application since the reflected RF power cannot be measured accurately and the use of electrically small antennas is not accounted for. Curty et al. only used the overall efficiency in their paper and claims an overall efficiency of 37%, based on an incident power of 2.7 μW and an output power if 1 μW.

Chow et al. [25] defines the overall efficiency of a rectifier circuit using

$$\eta = \frac{V_{out}I_{out}}{2NI_sB_1\left(\frac{V_0}{V_T}\right)e^{\left(-\frac{V_{out}}{2NV_T}\right)}} \tag{2.3}$$

where V_{out} is the output voltage, I_{out} is the output current, N is the number of stages, I_s is the diode saturation current, V_T is the diode thermal voltage, and $B_1(V_o/V_T)$ is the first order modified Bessel function. It is assumed that V_o refers to the peak input RF voltage since no definition for V_o is given. The origin of Equation 2.3 is not clear and no explanation or reference could be found as to how the equation is derived in any of Chow's papers or in his PhD dissertation. Equation 2.3 is however never used by Chow

المنارة للاستشارات
www.manaraa.com

to calculate rectifier efficiency. They use the phrase "Power Conversion Efficiency" (PCE), then calculate the overall efficiency as defined by Curty. They claim an overall efficiency of 11.3% based on an incident power of 20 mW and an output power of 2.25 mW.

Yi-Chun et al. [19] do not specifically state the efficiency of their rectification, but they do give the incident power as -10.5 dBm and the output dc power as 2.3 µW. Based on the incident and output power given, the overall efficiency is calculated as 2.6%. Radiom et al. [20] also do not specify an efficiency, but it is calculated to be 5.2% based on their stated incident power of -19.4 dBm and output power of 0.6 µW. The rectifier circuit is used to only power a voltage sensing circuit, a voltage regulator, and a power-on-reset circuit, resulting in the low power consumption. A summary of the performances of current systems is shown in Table 2.

Table 2. Rectifier Performance.

Lead Author Pub year	Rectifier type	Storage capacitor	Voltage generated	Current supplied	Efficiency
Curty 2005	Three stage full wave diode connected MOSFET (0.5 µm silicon-on-sapphire process)	None	1 V	1 µA	Overall: 37%
Chow 2011	Two-stage half-wave p-type Schottky diodes (130 nm CMOS process)	20 µF	1 V	37 µA	Overall: 11.3%
Yi-Chun 2011	Six-stage half-wave zero-Vt diode connected NMOS (130 nm CMOS process)	None	1.5 V	1.5 µA	Overall: 2.6%
Radiom 2010	Nine-stage full-wave diode connected MOSFET (UMC 0.18 µm process)	6 nF	1.8 V	0.33 µA	Overall: 5.2%

2.5 Electrically Small Antennas

One of the applications for the transponder described in this paper is to wirelessly measure the pressure in the eye. In order to fit in the anterior chamber of the eye, the

المنارة للاستشارات
www.manaraa.com

antenna cannot be larger than 9mm long by 6mm wide. The desired area of operation for RFID implantable devices is shown in Figure 10.

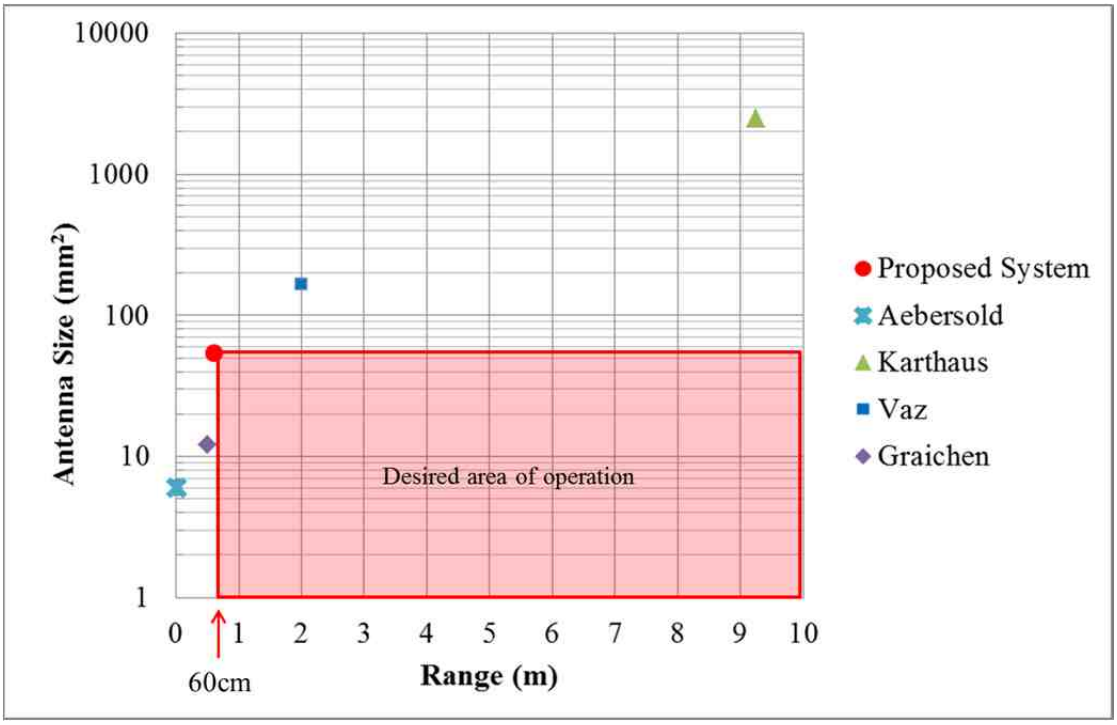

Figure 10. Operating range versus antenna size for RFID telemetry systems Aebersold[1], Karthaus[16], Vaz[17], Graichen[8].

Some commercial antenna structures used in commercial RFID applications, but not used or developed for biomedical applications, are shown in Figure 11. All the antennas shown, except for (b), operate at frequencies between 840 MHz and 960 MHz.

المنارة للاستشارات
www.manaraa.com

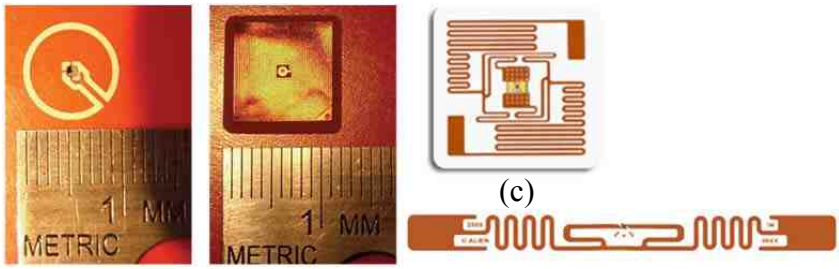

(a) (b) (c) (d)

Figure 11. (a) Impinj "Button" antenna, (b) HF (3 – 30 MHz) antenna, (c) Alien Technology "Square Antenna", 22.5 mm x 22.5 mm, (d) Alien Technology "Squiggle" antenna, 95 mm x 8.2 mm.

Seminal work on electrically small antennas (ESAs) were performed by Chu[26] and Wheeler[27] in the 1940s. They established the theoretical foundations for the fundamental limitations of electrically small antennas, with specific reference to the gain (G) and quality factor (Q) of the antenna. Various definitions for electrically small antennas exist, but any antenna in which its greatest dimension is less than a quarter wavelength is considered to be electrically small. Some recent works on ESA design are discussed.

Marrocco et al. [28, 29] used an evolutionary design approach by means of the genetic algorithm (GA). Their starting point was a non-uniform meander line antenna with optimization parameters identified as shown in Figure 12.

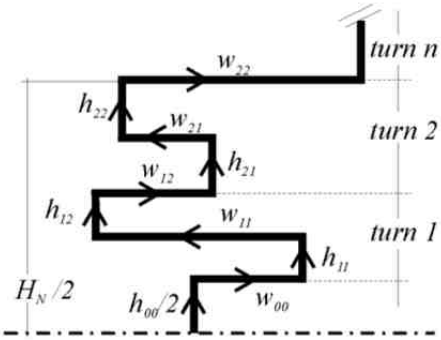

Figure 12. Half of a meander line dipole shown[29].

المنارة للاستشارات
www.manaraa.com

Their findings are summarized as follow:

- The gain decreases for increasing number of turns *N*.
- The gain approaches the gain of a straight dipole as the total height *H* increases.
- Most of the power is dissipated near the center of the antenna where the currents are the highest.
- The radiation resistance is mainly affected by the vertical segments.
- The loss resistance is primarily determined by the wire diameter and the total wire length.
- For fixed area (W_{max} x H_{max}) the optimum gain is obtained with an antenna design that has the highest radiation resistance and the smallest total wire length as shown in Figure 13.

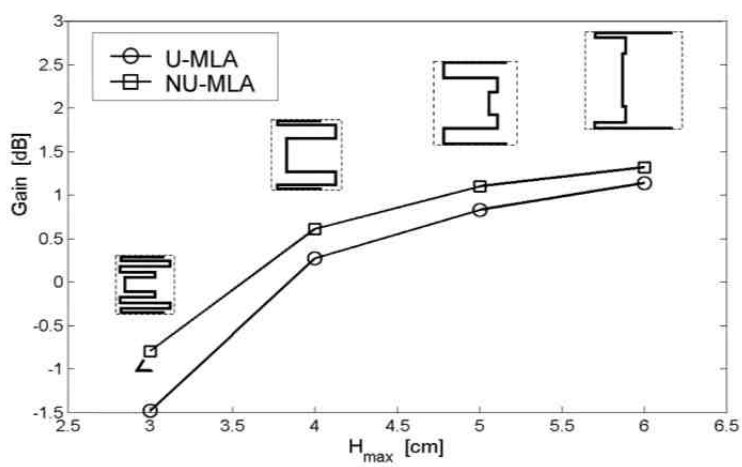

Figure 13. Gain versus area for optimized non-uniform meander line antennas – from 3 cm x 3 cm to 6 cm x 6 cm[29].

A variety of antenna geometries were studied by Best and Morrow[30] to investigate the way in which the current vector alignment affects the resonant frequency

المنارة للاستشارات
www.manaraa.com

of the antenna. All antennas shown in Figure 14 have the same planar area, total wire length and wire diameter.

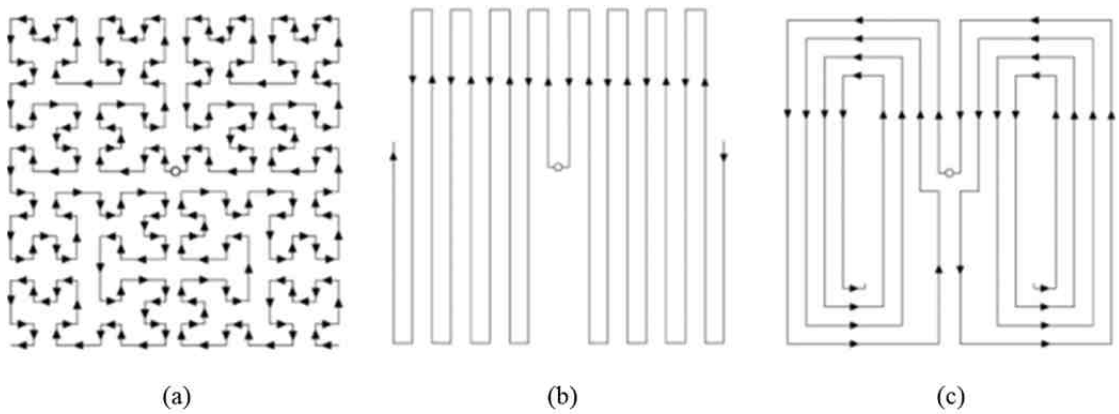

Figure 14. Meander antenna iterations – (a)Reference antenna, Fr = 267 MHz; (b) Planar antenna 1, Fr = 295.3 MHz; (c) Planar antenna 2, Fr = 154.9 MHz.[30].

Although the current differs in its relative direction throughout the antenna structure, the current is in phase over the length of the wire. Current vectors in closely coupled parallel sections that are in-phase and in opposing directions tend to cancel, reducing the self-inductance and the effective length of the wire. The reduction in effective length increases the resonant frequency of the antenna. The current vectors that are in-phase, and in the same direction reinforce each other and thereby increase the self-inductance and the effective length of the wire. The increase in effective length decreases the resonant frequency of the antenna. Best and Morrow found that the resonant frequency of the antenna is determined by the current vector alignment within each dipole arm, the capacitive coupling between dipole arms, and the relative location of the antenna feed point.

Gosalia et al.[31] designed and implemented a 6 x 6 mm planar meander dipole antenna for use in an intraocular retinal prosthesis. They started with a prototype antenna measuring 52.5 x 52.5 mm that was later scaled down by a factor of 10 to operate at a

المنارة للاستشارات
www.manaraa.com

frequency of 1.41 GHz. Phase reversal was used to do impedance matching; when a full wave dipole is fed a quarter wavelength from one end, the current phase distribution is significantly different from a center fed dipole. In the case of a planar meander line antenna, phase reversal improves the directivity in the broadside direction and provides impedance matching close to full wave resonant frequency.

In order to implement phase reversal, instead of moving the feed point, one of the arms of the dipole is shortened incrementally until a good match to 50 ohms is obtained as shown in Figure 15.

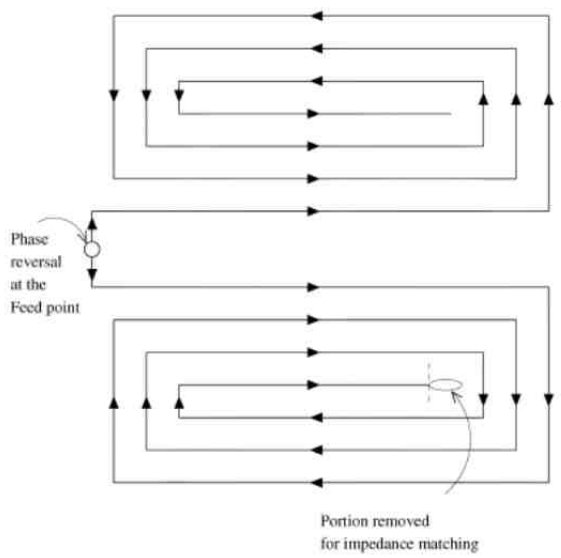

Figure 15. Impedance matching through phase reversal[31].

The antenna Q was not a focus of the study; however it was noted that the antenna shows a high directive gain at the expense of bandwidth, resulting in very high Q antenna. The resonant frequency was decreased by increasing the losses in the substrate and was implemented by using a substrate with a higher permittivity. The meander dipole, when compared to a patch antenna, provided superior performance.

المنارة للاستشارات
www.manaraa.com

CHAPTER 3. RFID THEORY

3.1 Introduction

Radio Frequency Identification (RFID) has been around for decades in different forms. During World War 2, the British used RFID principles to identify friendly aircraft using the IFF (Identify Friend or Foe) system [12]. In the United States, the Los Alamos National Laboratory developed access control systems in the 1960s that were closely related to modern RFID. Since then, the use of RFID has become pervasive in modern society. Radio Frequency Identification is widely used today in diverse applications such as inventory control, theft prevention, road toll collection, animal identification and recently as implantable medical devices [25].

Radio Frequency Identification systems can broadly be classified in terms of their operation as near-field (inductive magnetic field coupling) or far-field (EM radiated field coupling). The transponders or implantable devices used in either of these two classifications can further be divided into passive and active devices. Passive devices contain no battery or self-contained powering component, but require an external field source to provide power to the transponder. Active devices contain a battery that provides power to the transponder. Passive devices are preferred in implantable applications because batteries contain toxic chemicals that can leak out over the lifetime of the implant and cause harm to the patient. Batteries are also fairly large and limit the extent

المنارة للاستشارات
www.manaraa.com

to which implantable devices can be miniaturized. The system proposed in this research is a far-field, passive transponder system and the theoretical discussion will therefore be limited to these type of systems.

The theory that forms the basis for the transmission and reception of electromagnetic waves is traced back to James Clerk Maxwell in 1873 [13]. He developed the famous "Maxwell's Equations" that unified the theories of electricity and magnetism. The electric and magnetic fields and their relationships are given by [32]

$$\nabla\times\mathbf{H}=\dot{\mathbf{B}}+\mathbf{J} \qquad \oint \mathbf{H}\cdot d\mathbf{s}=\int(\dot{\mathbf{D}}+\mathbf{J})\cdot d\mathbf{a} \qquad (3.1),$$

$$\nabla\times\mathbf{E}=-\dot{\mathbf{B}} \qquad \oint \mathbf{E}\cdot d\mathbf{s}=-\int \dot{\mathbf{B}}\cdot d\mathbf{a} \qquad (3.2),$$

$$\nabla\cdot\mathbf{D}=\rho \qquad \oint \mathbf{D}\cdot d\mathbf{a}=\int \rho\, dV \qquad (3.3),$$

$$\text{and } \nabla\cdot\mathbf{B}=0 \qquad \oint \mathbf{B}\cdot d\mathbf{a}=0 \qquad (3.4),$$

where **H** is the magnetic field strength, **B** is the magnetic flux density, **J** is the current density, **E** is the electric field strength, **D** is the electric flux density, and ρ is the charge density.

Antennas are used to couple electric signals to free space. Any time varying current in a wire will result in electromagnetic radiation [13]. If a time varying voltage source is connected to a two-conductor transmission line, then time varying electric and magnetic fields will be created between the conductors. These fields create electromagnetic waves that travel along the transmission line. An antenna connected to the transmission line will radiate the electromagnetic fields into free space. Launching of electric field lines from an antenna is shown in Figure 16.

المنارة للاستشارات
www.manaraa.com

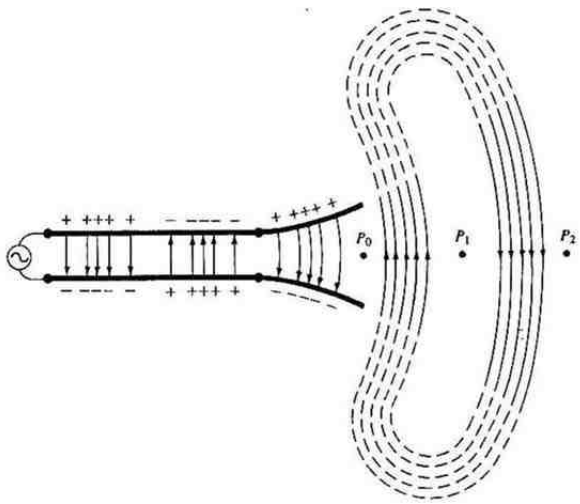

Figure 16. Source and transmission line with antenna showing detachment of electric field lines.[13].

Once the electric fields lines separate from the antenna, they form free-space waves that travel outwardly from the antenna. The waves travel through space and are subject to a free-space path loss that is equal to $(\lambda/4\pi r)^2$, where λ is the wavelength of the signal and r is the distance from the transmitting antenna[33].

The space surrounding the antenna is divided into three regions: the near-field, the intermediate field and the far-field [13]. The near-field is defined as the region within a radian distance $r < \lambda/2\pi$. The intermediate-field exists for a radian distance $r > \lambda/2\pi$ and the far-field is defined as the region where $r >> \lambda/2\pi$. The boundary distance of $\lambda/2\pi$ defines the transition between reactive (stored) energy and radiating energy and is also the limit for near-field inductive coupling.

The basis for inductive coupling of energy is found in Faraday's law given by

$$\oint_c \boldsymbol{E} \cdot d\boldsymbol{l} = -\frac{d}{dt}\int_s \boldsymbol{B} \cdot d\boldsymbol{s} \tag{3.5}$$

المنارة للاستشارات
www.manaraa.com

where $\boldsymbol{B}$ is the magnetic flux density that crosses an incremental area *ds* of a surface *s* that is bounded by a closed contour *c*, and $\boldsymbol{E}$ is the electric field.

Faraday's law states that the voltage induced in a closed loop is equal to the time rate of change of the magnetic flux that penetrates the surface *s* whose perimeter is the contour *c*. The induced voltage is directly proportional to the frequency of the magnetic field and implies that better performance can be expected at higher frequencies. This relationship is only true if the two antennas are within the near-field radian distance so that magnetic coupling is possible, and is therefore not useful for radian distances greater than $\lambda/2\pi$. Effective transfer of energy over longer distances using electrically small antennas is therefore only possible when the electromagnetic signal is captured in the far-field.

The Friis free-space transmission formula gives the relationship between the received power and the transmitted power in an RF transmission system. For antennas that are matched in terms of polarization and are aligned for maximum directional radiation and reception, the Friis transmission relationship is given by

$$P_R = \left(\frac{\lambda}{4\pi r}\right)^2 P_T G_T G_R \tag{3.6}$$

where P_R = received power, P_T = transmit power, G_T = transmit antenna gain, G_R = receive antenna gain, λ = wavelength of the frequency used and r = distance between the two antennas [10]. The distance (or range) r, between the two antennas is directly related to the wavelength of the frequency being used. Considering transmission frequencies of 915 MHz and 2.45 GHz respectively, a range increase by a factor of 2450/915 = 2.7

المنارة للاستشارات
www.manaraa.com

times is expected if 915 MHz is used instead of 2.45 GHz. Solving Equation 3.6 for *r* yields

$$r = \left(\frac{\lambda}{4\pi}\right)\sqrt{\frac{P_T G_T G_R}{P_R}} \tag{3.7}$$

If $P_T = 1\ W$, $G_T = G_R = 1$ and $P_R = 1\ \mu W$, a range of 26.1 m for a frequency of 915 MHz is obtained and a range of 9.71 m for a frequency of 2.45 GHz. The calculation confirms a range improvement by factor of 2.7 using 915 MHz. The range improvement at 915 MHz is one of the reasons why a frequency of 915MHz was chosen for this application.

Yawen et al. [34] has estimated the body tissue attenuation from inside the human body for different frequency bands using 5cm thick porcine tissue and a saline solution. An attenuation of 16.49 dB can be expected at frequencies between 902 and 928 MHz and an attenuation of 37.5 dB can be expected at frequencies between 2.4 and 2.5 GHz. The attenuation factors show that an additional 21 dB attenuation needs to be accounted for and the power needs to be increased by a factor of 126 if a frequency of 2.45 GHz is used instead of 915 MHz.

The free space and body attenuation indicates that a frequency if 915 MHz will provide at least a factor of 2.7 increase in range over 2.45 GHz. In the final analysis, the increased size of the antenna at 915 MHz must also be taken into account. The approximate area of the proposed antenna will be 0.1 square inches. This corresponds to extrapolated ranges of 1.6 feet at 2.45 GHz and 4.2 feet at 915 MHz. The extrapolated ranges give a range factor increase of 2.63 that is compatible with the range factor

المنارة للاستشارات
www.manaraa.com

increase calculated using the Friis free-space equation. A comparison of antenna sizes and range for actual commercial devices are shown in Figure 17.

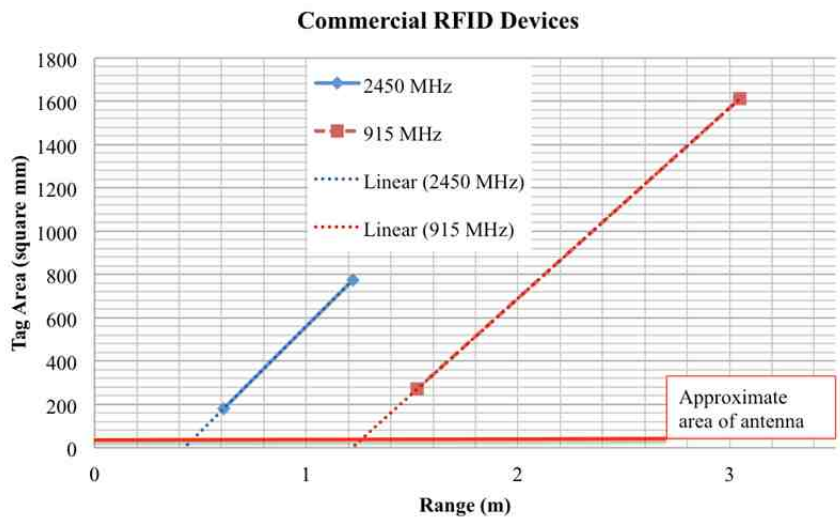

Figure 17. Range of commercial RFID devices[35].

The effect of the body on the RF signal will essentially be twofold. Any fluids, due to the dielectric loading effect, will detune the antenna, and the body tissue will attenuate both the incoming and outgoing signals. As an example to further illustrate the body effect, consider the case of implantation of the device in the eye. Assuming that the device will be implanted in the aqueous humor (anterior chamber) just before the lens of the eye, the liquid in the chamber will have an inductive loading effect on the antenna. The antenna will therefore have to be made to be more capacitive in the air in order to counter the inductive loading of the liquid in the anterior chamber [36].

The effect of the eye is determined by calculating the received power with the eye as the transmission medium and comparing that to the received power through free space. The received power at the implant is given by [37]

المنارة للاستشارات
www.manaraa.com

$$P_R = \frac{P_T G_T G_R \eta^2}{r^2 \omega^2 \mu^2} \tag{3.8}$$

where η is the intrinsic impedance of the medium through which the signal is transmitted, ω is the radian frequency of the signal, and μ is the magnetic permeability in H/m. This equation is valid if the antennas are matched in terms of polarization and are aligned for maximum directional radiation and reception.

It is assumed that the antennas are matched and that $G_T = G_R = 1$. The intrinsic impedance is given by [38]

$$\eta = \sqrt{\frac{j\omega\mu}{\sigma + j\omega\varepsilon}} \tag{3.9}$$

where σ = conductivity of the medium in Siemens/m and $\varepsilon = \varepsilon_r \varepsilon_o$ = permittivity in Farad/m.

With the placement of the device in the anterior chamber, the cornea, the fluid in the chamber, and the eyelid will be the tissues that affect the signal. Dielectric properties for the fluid in the anterior chamber could not be found, so it was assumed that the dielectric properties for the fluid and the chamber are identical.

Considering the cornea first, the conductivity is 1.4008 S/m at a frequency of 915MHz and the relative permittivity is 55.172 [39]. Using these values, and assuming that the relative permeability of the cornea is 1, the intrinsic impedance was calculated to be $48\angle 13.273^{\circ}$.

المنارة للاستشارات
www.manaraa.com

Considering the worst case (unity antenna gains), the received power is given by

$$P_R = \frac{P_T \eta^2}{r^2 \omega^2 \mu^2} = \frac{\left(48\angle 13.273^\circ\right)^2}{(2\pi \times 915 \times 10^6)^2 (4\pi \times 10^{-7})^2} \frac{P_T}{r^2} = (277.36 \times 10^{-6} \angle 26.5^\circ) \frac{P_T}{r^2}. \quad (3.10)$$

Using a transmit power of 1 W and a distance of 1 m, the received power is 277 µW or -5.57 dBm. To compare this to free space transmission, the Friis free space transmission equation, equation 3.6, is used with $G_T = G_R = 1$. With a transmit power of 1W at 915MHz, the power received at a distance of 1m is then 680µW or -1.67 dBm. The cornea adds about 3.9 dB attenuation to the signal. Provision will have to be made for approximately 3.9 dB attenuation of the signal in both the forward and reverse directions if the device is implanted in the anterior chamber of the eye.

Wireless powering of the implantable device/sensor is the limiting factor in the range that can be achieved with RIFD systems. Performance limitations for commercial RFID devices in free space are illustrated in Figure 18. The range limitation shown in Figure 18 is for a 915MHz system with a transmit power of 4W (36dBm).

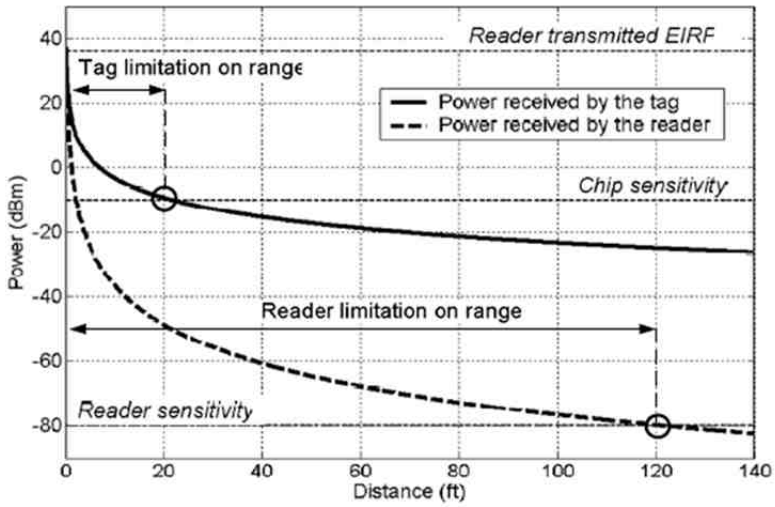

Figure 18. Performance limitation of RFID systems[40].

المنارة للاستشارات
www.manaraa.com

The reader sensitivity is specified as -80dBm and the tag sensitivity as -10dBm with a tag antenna gain of 2dBi. An implantable wireless sensor will be subject to the same limitations with the added attenuation of the body tissue. The range can be improved by increasing the rectifier efficiency, reducing the power consumption of the implant and increasing the efficiency (gain) of the implant antenna.

3.2 Electrically small antennas

Antennas are used to couple electrical signals with free space. The simplest and cheapest antenna is a wire antenna used in a dipole configuration. The classic wire dipole consists of two equal lengths of wire that is center-fed with a two-wire transmission line. The most efficient standing wave pattern of the current is obtained when the total length of the dipole is equal to half the wavelength of the signal. Current distributions for different dipole lengths are shown in Figure 19.

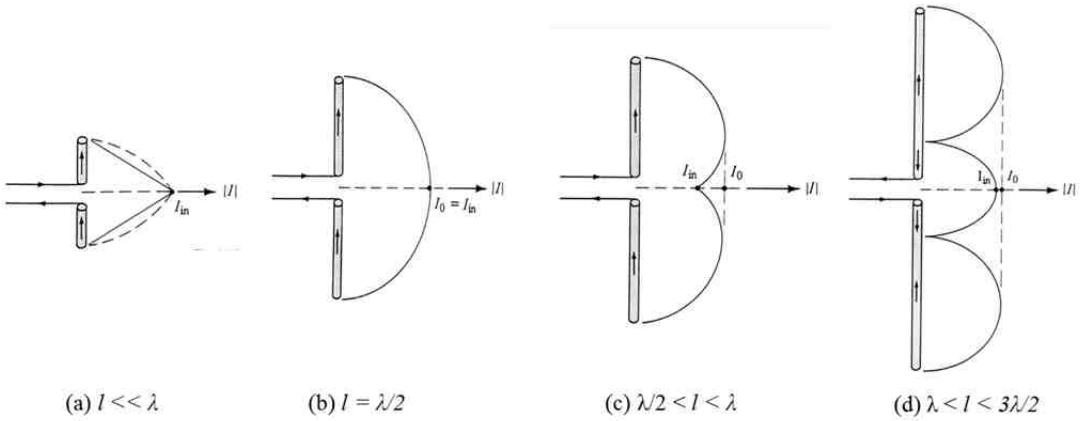

Figure 19. Current distribution on wire dipoles[13].

The ideal current distribution is shown in Figure 18 (b). It is a sinusoidal standing wave pattern with nulls at the end of the dipole arms and provides the most efficient coupling of the electrical signal to free-space. In some applications, such as IOP sensing

المنارة للاستشارات
www.manaraa.com

devices, the size of a half-wavelength antenna is impractical. The wavelength of an electromagnetic signal is given by

$$\lambda = \frac{\upsilon}{f} = \frac{c}{\sqrt{\mu_r \varepsilon_r} f} \tag{3.11}$$

where υ is the velocity of propagation, μ_r is the relativity permeability of the medium, ε_r is the relative permittivity of the medium, c is the velocity of propagation in free space and f is the frequency of the signal. In free space this reduces to $\lambda = c/f$. A half-wavelength antenna at 915MHz will have a total length of 164mm, which is much too large for implantation in the eye, and electrically small antennas will have to be used for these types of applications.

An antenna is considered to be electrically small when its maximum dimension is less than $\lambda/2\pi$ [27]. An Electrically Small Antenna (ESA) is not as efficient as a half-wavelength antenna and actually has several characteristics that limit its performance such as low radiation resistance, high reactance, narrow bandwidth, and increased loss in the matching network [41]. An ESA can still be used effectively in applications where a half-wavelength antenna is too large.

The performance of an ESA is characterized by its size, quality factor Q and gain G. The size will, in most cases, be determined by the application. In the case of an intra-ocular implant, the size is limited to 6.5mm x 6mm for implantation in the eye. If implanted under the eyelid, it is limited to 10mm x 10mm. The quality factor of an antenna is defined as the ratio of the energy stored in the antenna to the energy radiated by the antenna [42]. The Q of antenna is an indication of the performance of an antenna and the physical limitations of antenna size on the gain. An antenna with a high Q value

المنارة للاستشارات
www.manaraa.com

will store large amounts of reactive energy in the near field. The stored energy and high Q will result in high currents, large resistive losses, and narrow bandwidth. The gain of an antenna is generally defined as the ratio of the radiation intensity in a given direction to the radiation intensity of a lossless isotropic antenna.

An equation to determine the Q factor of electrically small antennas was first developed by Wheeler in 1947 [27]. His work was later generalized by Chu [26] and an exact expression for the smallest possible Q for a linearly polarized electrically small antenna was derived by McLean [43] and is given by

$$Q = \frac{1}{(ka)^3} + \frac{1}{ka}, \tag{3.12}$$

where k is the wave number ($2\pi/\lambda$) and a is the radius of the smallest sphere that encloses the antenna. Equation 3.12 shows that the Q of an antenna is inversely proportional to the physical size of the antenna. Electrically small antennas will always have a high Q and narrow bandwidth.

Just as they have a lower limit for Q, electrically small antennas have an upper limit for gain given by[44]

$$G = (ka)^2 + 2ka. \tag{3.13}$$

The gain is directly proportional to the physical size of the antenna. Equations 3.12 and 3.13 implies that the optimum antenna design will be one in which the antenna makes the maximum use of its allocated space. The physical limitations on the performance of electrically small antennas are important parameters that should be taken into account in the design of these types of antennas.

المنارة للاستشارات
www.manaraa.com

The impedance of an antenna should be matched to that of the load to allow for maximum transfer of power. Maximum power will be transferred when the impedance of the load is the complex conjugate of the impedance of the antenna. In conventional RF system design, a nominal impedance of 50Ω is typically used. It is customary to design an antenna to have a driving point impedance close to 50Ω. In electrically small planar wire dipole antennas, an impedance close to 50Ω is usually obtained by adjusting the lengths of the arms of the dipole. In order for maximum power transfer, it is necessary for the load to also have an impedance close to 50Ω. The impedance matching is usually implemented by using combinations of inductors and capacitors and is referred to as passive matching. Passive matching associated with electrically small antennas is only effective over a very narrow bandwidth [45]. Electrically small antennas have a high Q and therefore a high reactance. This means that the matching network needs to have a high conjugate reactance and low resistance. The high reactance and low resistance will result in large current flow and large standing waves that will magnify the losses in the network [41]. These losses can be so pronounced that using no matching network is a viable alternative.

3.3 RF rectification

The concept of wireless power transfer was first demonstrated by Tesla in 1891[46] . Since then, much progress has been made in the field of energy harvesting, as it has now become known. Power transfer is affected in the near field by inductive coupling and rectification or in the far field by rectifying the incident RF signal. The signal is first captured by the antenna and then transferred to the rectifying circuit. The rectifying circuit consists of either a full-wave rectifier or a half-wave rectifier. Schottky

المنارة للاستشارات
www.manaraa.com

diodes with a low junction voltage are typically used for the rectifier circuit. Schottky diodes are used because they generally have a lower junction voltage and higher saturation current than normal p-n diodes and they are typically much faster[47]. An alternative is to use MOSFET transistors connected as diodes or in a four transistor cell configuration to form a self-driven synchronous rectifier [48].

Two basic rectifier topologies are commonly utilized. One is the common half-wave rectifier configuration which is referred to as the Greinacher voltage doubler or Cockcroft-Walton multiplier [23]. Multiple stages are usually needed, due to the low power of the received signal. A two-stage Greinacher circuit configuration is shown in Figure 20.

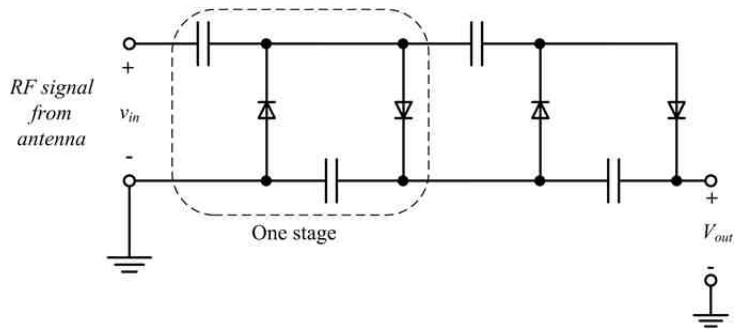

Figure 20. Two-stage Greinacher half-wave rectifier circuit.

The second rectifier topology often used is a modified Greinacher circuit and is referred to as the Dickson circuit. A typical circuit configuration for a half-wave rectifier using Schottky diodes is shown in Figure 21. The basic difference between the Dickson and Greinacher circuit configurations is that the capacitors in the Dickson case are rearranged so that each rectifying diode receives the same input signal amplitude [23]. This change in the circuit also reduces the input impedance. The DC output voltage for the rectifier is approximated by [16]

المنارة للاستشارات
www.manaraa.com

$$V_{DD} = n \cdot (V_{pin} - V_D) \tag{3.14}$$

where n is the number of diodes, V_{pin} is the amplitude of the input signal and V_D is the forward voltage of the diodes.

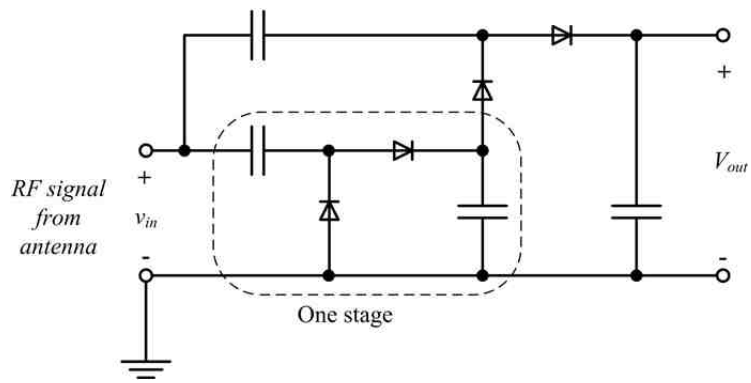

Figure 21. Two-stage Dickson half-wave rectifier.

3.4 Oscillators

Sensors for measuring physiological pressure typically consist of Microelectromechanical Systems (MEMS) capacitive pressure sensors [49]. Most implantable transducers make use of some kind of capacitor dependent oscillator. These types of oscillators have a frequency of oscillation that is proportional to one or more capacitances in the circuit. If the capacitor is replaced with a capacitive pressure sensor, the frequency of oscillation will change with a change in pressure.

An oscillator circuit is a feedback circuit that contains a self-sustaining mechanism that allows the noise in the circuit to grow and become a periodic signal [50]. Two conditions, known as Barkhausen's criteria, must be met simultaneously for a circuit to oscillate: the loop gain must be equal to or greater than unity and the total phase shift around the feedback loop must be equal to 180˚ [51]. These conditions have generally

المنارة للاستشارات
www.manaraa.com

been accepted as necessary and sufficient criteria for stable oscillations. There are circuits that do not oscillate even though the Barkhausen criteria are met [52]. A more accurate statement is that the Barkhausen criteria are necessary but not sufficient conditions for oscillation. Testing for the Barkhausen criteria is however the starting point for most oscillator design. Most RF oscillator circuits contain a LC tank in the feedback loop to stabilize the frequency of oscillation. To minimize noise, the majority of discrete RF oscillators contain only one transistor. One of the simplest RF oscillators is the Colpitts oscillator. This oscillator is more frequently used since it incorporates only one inductor. In the typical Colpitts oscillator circuit shown in Figure 22, the inductor and capacitors C_2 and C_3 form the tank circuit in the feedback loop. The frequency of oscillation is given by

$$f = \frac{1}{2\pi\sqrt{L_{eq}C_{eq}}} \tag{3.15}$$

where L_{eq} and C_{eq} are the equivalent inductance and capacitance in the tank circuit.

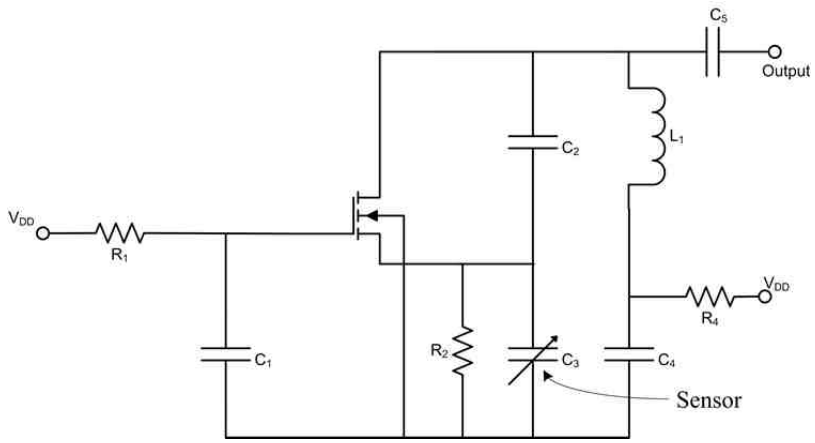

Figure 22. MOSFET Colpitts oscillator.

المنارة للاستشارات
www.manaraa.com

CHAPTER 4. OSCILLATOR LOCK-IN

4.1 Background

Oscillator lock-in or locking is a condition that some oscillating systems suffer from where the oscillator locks onto the fundamental frequency or harmonics of an external signal source. Oscillator locking has been widely studied and is commonly referred to as injection locking or pulling [53-55]. This behavior occurs when the natural frequency of an oscillator becomes locked to the frequency of a signal whose frequency is close to that of the free-running oscillator frequency. In certain applications, such as frequency modulation receivers, this is a desirable effect, but in this case, where the frequency of oscillation is directly related to the pressure measured, it is clearly detrimental. Little research has been done on this locking effect in RFID sensor systems.

An inductively coupled system was developed at the University of Louisville to wirelessly measure intra-ocular pressure [1]. This system makes use of an astable multi-vibrator oscillator Integrated Circuit (IC) connected to a micro-electro mechanical system (MEMS) capacitive pressure sensor. Variations in the pressure result in a change in the frequency of oscillation. The system is powered inductively by an RFID reader and the frequency of oscillation is read using load modulation [56]. The multi-vibrator oscillator displayed lock-in where the oscillator locks onto a harmonic of the fundamental frequency of the RFID reader that is used to power the IC.

المنارة للاستشارات
www.manaraa.com

Research was performed to investigate the locking effect observed in RFID sensor systems using two different types of oscillators. One system uses an astable multi-vibrator oscillator and the other uses a Colpitts oscillator. Both systems are connected to a MEMS capacitive pressure sensor. Both of these systems suffer from locking under certain conditions. These two oscillators were compared, with regard to their locking behavior, in an effort to gain insight into understanding this phenomenon in RFID sensor systems, and to derive an effective countermeasure to it.

The effect of oscillators locking to a frequency other than their free-running frequency has been observed and reported in prior work. Pioneering work was done by Van der Pol in the early 1900's when he derived and solved a second order differential equation to describe nonlinear oscillations [57]. His work was further refined and simplified by Adler who derived a differential equation for LC oscillators to describe the oscillator phase as a function of time[53]. Adler's expression is used to predict the range of frequencies over which a free-running oscillator will lock onto the frequency of another signal. Recently, more work has been done on deriving equations for predicting injection locking in LC and Ring oscillators [54, 55, 58]. Although Adler's equation was originally developed for LC oscillators and makes use of an explicit Q factor, it was applied to other oscillators if the Q can be defined and quantified, as was shown by Mesgarzadeh [58].

The lock-in range for oscillator locking is determined by

$$\left|\omega_o - \omega_{inj}\right| \leq \frac{\omega_o}{2Q}\frac{V_{inj}}{V_{osc}} \tag{4.1}$$

المنارة للاستشارات
www.manaraa.com

where ω_o = oscillator frequency, ω_{inj} = injected signal frequency, V_{inj} = voltage of injected signal and V_{osc} = voltage of oscillator output signal [54]. The Q of the oscillator is determined dependent on the type of oscillator. For LC oscillators, Q is defined as the ratio of the center frequency and the – 3 dB bandwidth. A broader definition, which can also be used for ring and multi-vibrator oscillators, is given by

$$Q = \frac{\omega_o}{2}\frac{d\varphi}{d\omega} \tag{4.2}$$

where ω_o is the resonant frequency and $d\varphi/d\omega$ is the slope of the phase of the transfer function with respect to frequency.

Injection locking, as defined above and by the lock-in range in equation 4.1, is desirable in certain applications; but in applications as described in this document it must be avoided. In applications where physiological parameters are measured using a capacitive sensor that forms part of an oscillator circuit, the frequency of oscillation must be related to the capacitance of the sensor. If the oscillator locks onto an external signal, the frequency of oscillation remains constant over a range of capacitance values.

4.2 Oscillator designs and lock-in tests

Two oscillators, an RC multi-vibrator oscillator and a Colpitts oscillator were compared with regard to lock-in behavior. The RC multi-vibrator oscillator was designed by Doug Jackson of the University of Louisville (UofL) Wireless and IC Design Laboratory based on a basic CMOS astable oscillator. An XNOR gate was used in the place of the typical second inverter to provide on/off control for the oscillator and to

المنارة للاستشارات
www.manaraa.com

reduce current consumption. The circuit schematic is shown in Figure 23a. The oscillation frequency is given by [59]

$$f_{osc} = \frac{1}{2.2RC} \tag{4.3}$$

Spice simulations were performed to determine if the circuits meet the Barkhausen criteria for oscillation. In the loop-gain and phase analysis, the Middlebrook method was used, where voltage and current test signals were injected into the circuit at a point in the signal path [60]. The points at which the test signals are injected are shown in Figure 23. Both circuits met the criteria for oscillation.

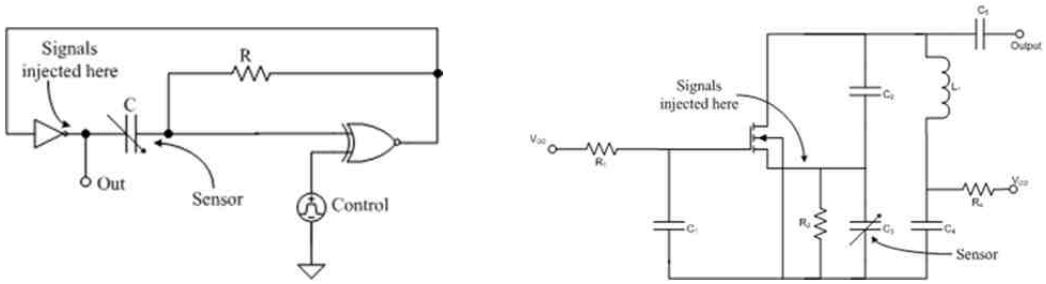

Figure 23. (a) RC multi-vibrator oscillator. (b) Colpitts oscillator.

The circuit layout for fabrication was performed using L-Edit from Tanner Tools. The circuit layout for the astable multi-vibrator oscillator is shown in Figure 24(a). This layout includes frequency divider and voltage regulation circuitry. The circuit layout for the Colpitts oscillator is shown in Figure 24(b). All resistors were designed using high resistance poly-silicon. All the capacitors, except the capacitive sensor, were on-chip. The only external components are the inductor and capacitive sensor that forms part of the LC tank of the oscillator. The circuits were fabricated using the OnSemi 0.5µm C5 process from MOSIS [61].

المنارة للاستشارات
www.manaraa.com

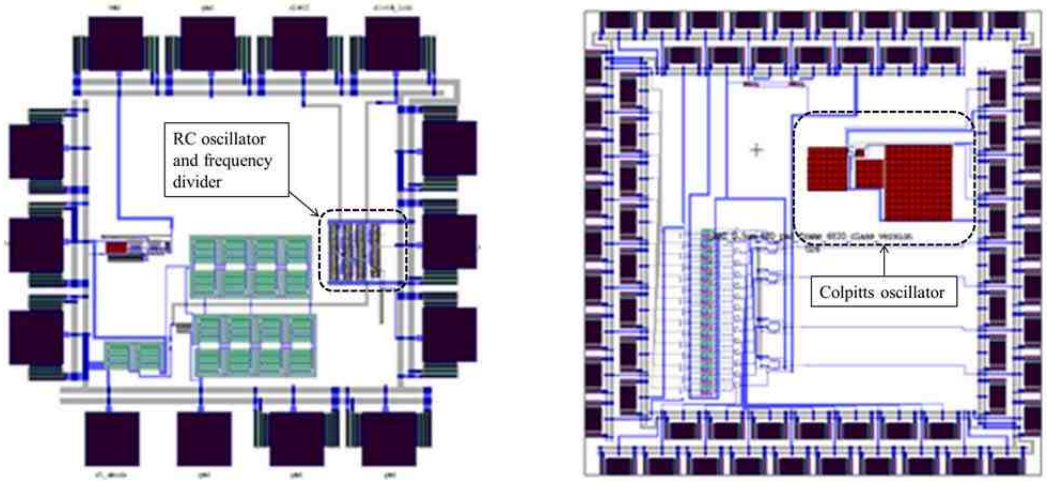

Figure 24. (a) RC multi-vibrator oscillator layout. (b) Colpitts oscillator layout.

The two oscillators were compared regarding their lock-in behavior in the RFID telemetry system. A MEMS pressure sensor was used as the sensing device and provided the variable capacitance in the multi-vibrator oscillator and for the LC tank in the Colpitts oscillator. The oscillator and the pressure sensor were placed in a pressure chamber and subjected to increasing pressure. The oscillators were both powered from the same 135 kHz RF reader and the frequency of oscillation was also read using the RF reader. The test setup for the RC multi-vibrator oscillator is shown in Figure 25.

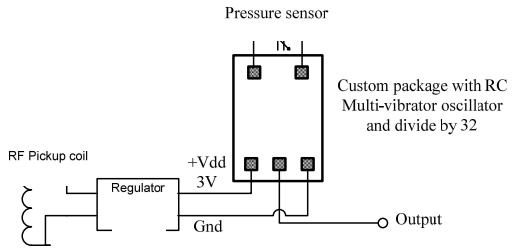

Figure 25. Multi-vibrator oscillator lo n test setup.

The test results for the multi-vibrator oscillator are shown in Figure 26 and clearly show that lock-in occurs around 2100 Hz. This lock-in behavior was also confirmed using a variable capacitor instead of the pressure sensor. The oscillator still locked in to a

المنارة للاستشارات
www.manaraa.com

frequency of 2100 Hz and confirmed that the lock-in behavior was not due to some resonance inherent to the pressure sensor.

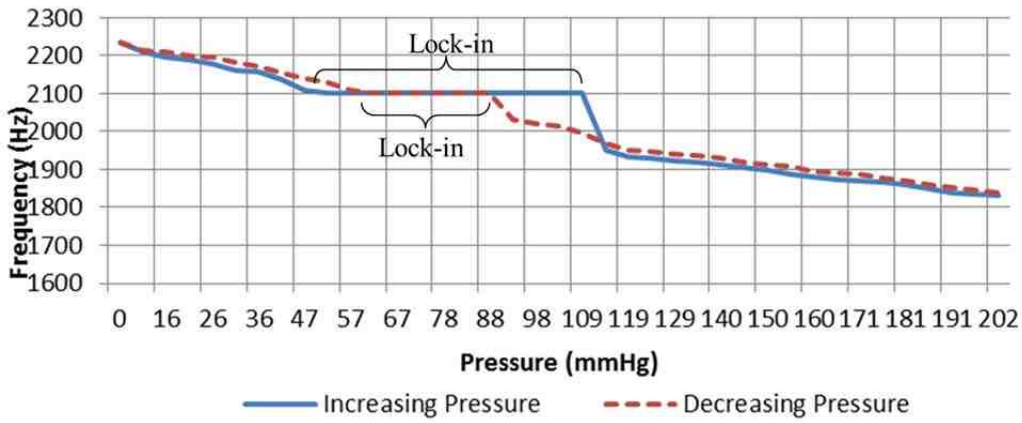

Figure 26. RC multi-vibrator oscillator output showing lock-in.

The same test was performed on the Colpitts oscillator. The output of the Colpitts oscillator was too low to drive the modulation circuit that was used as part of the telemetry; therefore an amplifier was designed to provide an adequate output. The Colpitts oscillator had a fundamental oscillation frequency of 7.4 MHz with a capacitance value of 1.6pF associated with the pressure sensor. The output of the amplifier circuit was used as the input to frequency dividers so that the higher oscillation frequency of the Colpitts oscillator was closer to the oscillation frequency of the RC multi-vibrator. The test setup is shown in Figure 27 and the pressure test results are shown in Figure 28. No lock-in behavior was observed.

المنارة للاستشارات
www.manaraa.com

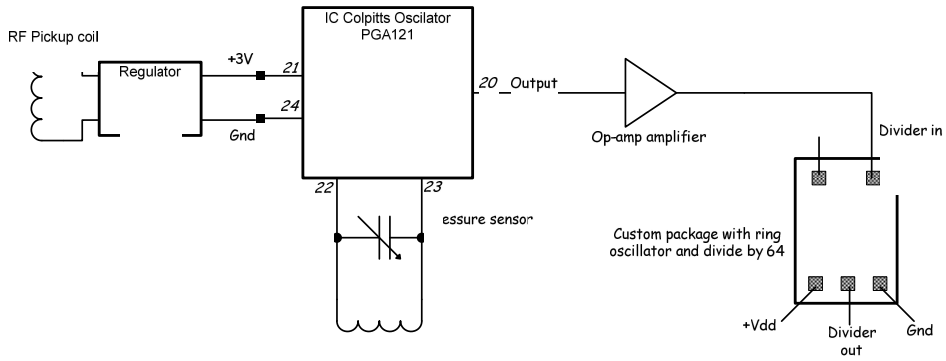

Figure 27. Colpitts oscillator lock-in test setup.

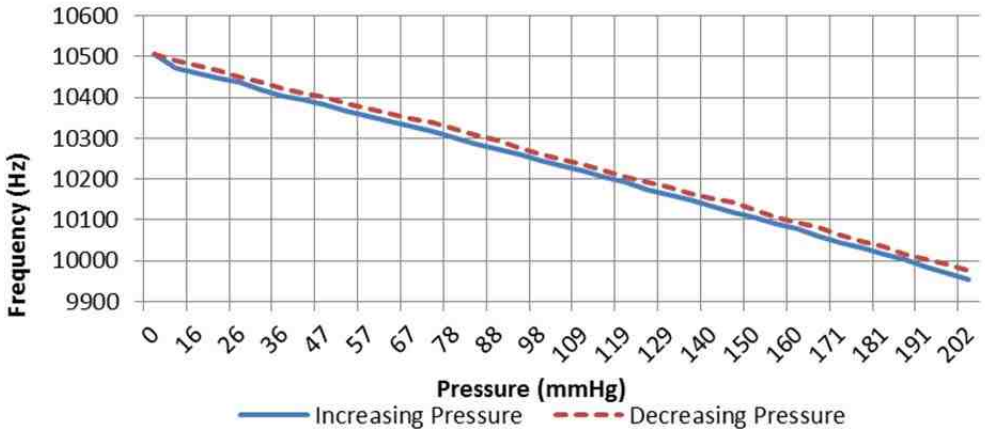

Figure 28. Colpitts oscillator output.

Further tests were done to investigate the lock-in behavior of both oscillators. The pressure sensor was replaced with a variable capacitor (1-30 pF). The multi-vibrator oscillator was powered using a power supply and the output spectrum of the oscillator was observed while the capacitor was varied from 1 to 30 pF. The oscillator signal frequency varied from 240 kHz with the capacitor at 3 pF to 92 kHz with the capacitor at 30 pF.

The reader was switched on and the effect of the reader signal on the output of the oscillator just before lock-in occurs is shown in Figure 29. The oscillator frequency is 137.5 kHz and the reader frequency is shown as 135 kHz at marker 2. The reader signal

المنارة للاستشارات
www.manaraa.com

is only 5 dBm down from the oscillator signal. When the oscillator frequency is not within the lock range, the reader signal is typically 26 dBm lower than the oscillator signal.

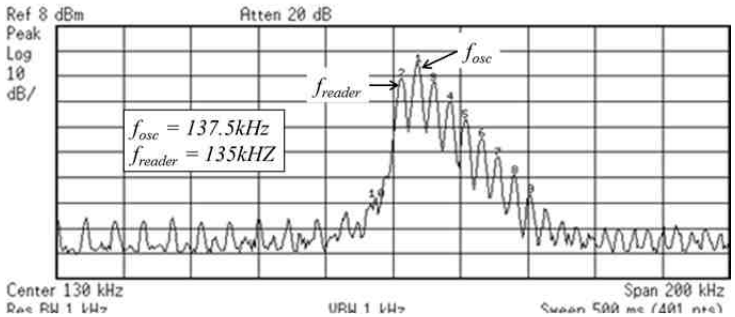

Figure 29. RC multi-vibrator oscillator just before lock-in.

It is clear that the oscillator circuit is also amplifying the reader signal. The spectrum shown in Figure 29 is typical of an oscillator spectrum where the injected signal frequency is close to but not within the lock range of the oscillator. The injected signal frequency, in this case the reader signal frequency, is also below the lock range and the oscillator frequency. The sidebands only appear above the reader frequency. The same behavior was observed and theorized by Razavi [54] and is referred to as "quasi-lock".

To investigate the lock-in behavior of the Colpitts oscillator, the oscillator was powered using a power supply. A 7 MHz sinusoidal signal, generated using a signal generator, and a loop antenna was used to simulate an RFID reader. The generated signal level was adjusted to approximately 26 dB lower than the Colpitts oscillator signal. The generated signal level is comparable to the signal level differences in the case of the RC multi-vibrator oscillator. A variable capacitor (1-30 pF) was used to replace the pressure sensor. With the generated signal and variable capacitor, the Colpitts oscillator exhibited locking behavior. The oscillator frequency varied from 7.363 MHz with the capacitance

المنارة للاستشارات
www.manaraa.com

at 1.6 pF to 6.575 MHz with the capacitance at 30 pF. The oscillator output spectrum, just before lock-in, is shown in Figure 30. The oscillator output signal frequency is at 6.97 MHz and the generator signal frequency is shown at 7.003 MHz. As was the case for the multi-vibrator oscillator, sidebands only appear below the generator signal frequency when the generator signal frequency is above the oscillator frequency. Similar behavior was observed when the generator signal frequency was below the oscillator frequency. Sidebands only appeared above the generator signal frequency. In the case of the Colpitts oscillator, the lock-in occurred over a capacitance range of 2.2 pF and a frequency range of 29 kHz. All these tests indicate the oscillator will lock-in when the oscillator frequency is close to the reader frequency.

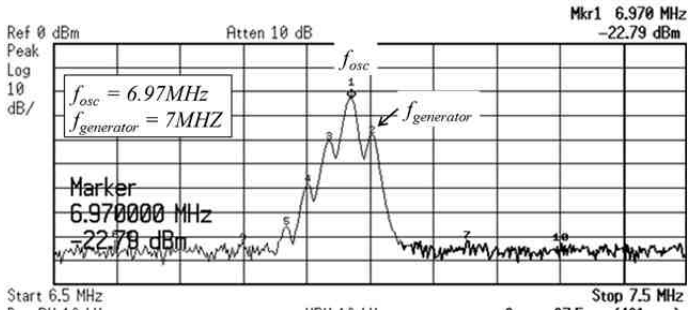

Figure 30. Colpitts oscillator output just before lock-in.

For both oscillators, lock-in occurred where the generated signal corresponds to integer multiples of the oscillator frequency. To investigate additional lock-in frequencies, a 200 mV sinusoidal signal was used with a DC offset as the power supply for the oscillators. The oscillator frequency was kept constant and the generator frequency was adjusted. The jitter associated with the output signal of the oscillator was viewed on an oscilloscope. When locked in, the jitter on the oscillator output signal disappeared, as was also shown by Razavi [54]. For both oscillators, lock-in occurred

المنارة للاستشارات
www.manaraa.com

where the generated signal corresponds to integer multiples of the oscillator frequency. The results of these tests are shown in Figures 31 and 32 and show the frequencies at which lock-in occurs and the range of frequencies of the lock-in.

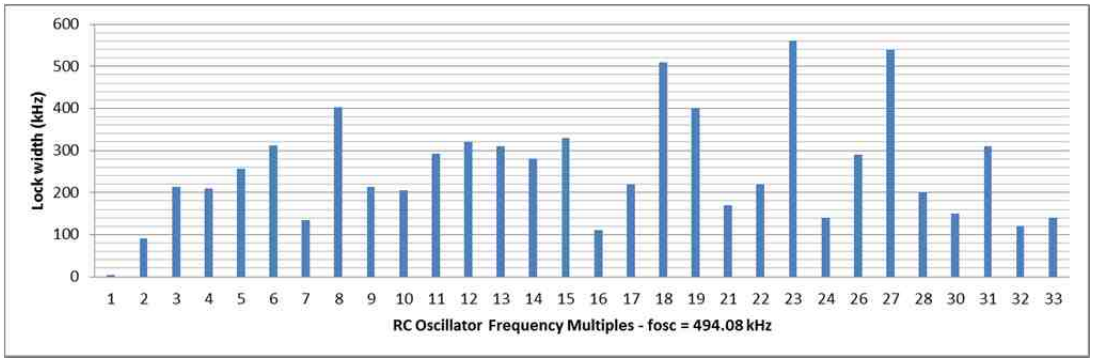

Figure 31. RC multi-vibrator lock-in frequencies and range.

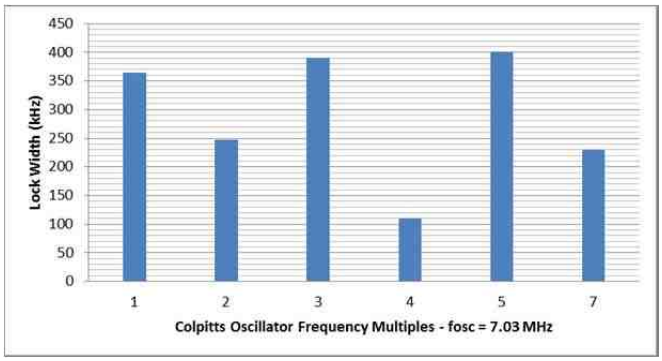

Figure 32. Colpitts oscillator lock-in frequencies and range.

It is also instructive to view the signals in the time domain. Two signals with frequencies that are integer multiples of each other are shown in Figure 33. The phases of the signals lock where the rising edges of the signals coincide.

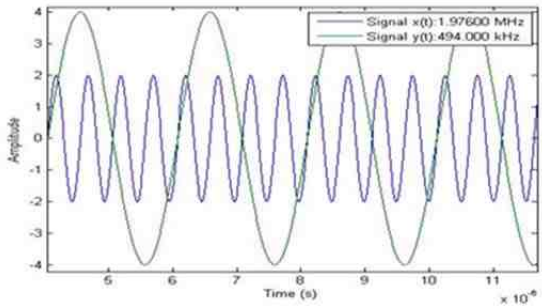

Figure 33. Time domain signal illustrating lock-in.

المنارة للاستشارات
www.manaraa.com

CHAPTER 5. ESA DESIGN AND DEVELOPMENT

5.1 Background

The area of the eye that can be utilized for implantation limits the maximum physical size of the antenna. If the antenna is to be incorporated into a "smart" Intra-Ocular Lens, then the size is limited by the physical size of the intra-ocular lens, which is approximately 12 x 6 mm [62]. The wavelength at 915 MHz is 328 mm; therefore, the physical size of a half-wavelength dipole antenna is 164 mm, which is much larger than the available space and thus necessitates the need for an electrically small antenna.

5.2 Design and simulation

Several antennas were designed and simulated using Advanced Design System (ADS) from Agilent Technologies. Advanced Design System (ADS) is an antenna design and simulation software package that uses Method of Moments electromagnetic simulation to characterize antennas. The antennas that were designed included half-wavelength wire and printed circuit board dipole antennas as well as electrically small meander dipole antennas. The half-wavelength dipole antennas were used as the primary antenna for transmitting the signal that was used to power the transponder. The electrically small meander dipole antennas were used as receiving antennas that were connected to the rectifier circuits.

المنارة للاستشارات
www.manaraa.com

5.3 Half-wavelength Dipole Antennas

Half-wavelength dipole antennas for implementation on FR-4 printed circuit board were designed and simulated in ADS. The resonant frequency and input impedance of the antennas were measured using a network analyzer and the values were compared to the simulated values. This was done to evaluate the accuracy of ADS as an antenna design tool. Half-wavelength dipole antennas are one of the most basic types of antennas and have been thoroughly characterized. The layout and simulation results for a straight-line half-wave dipole are shown in Figure 34. The simulated gain is 1.49 dB.

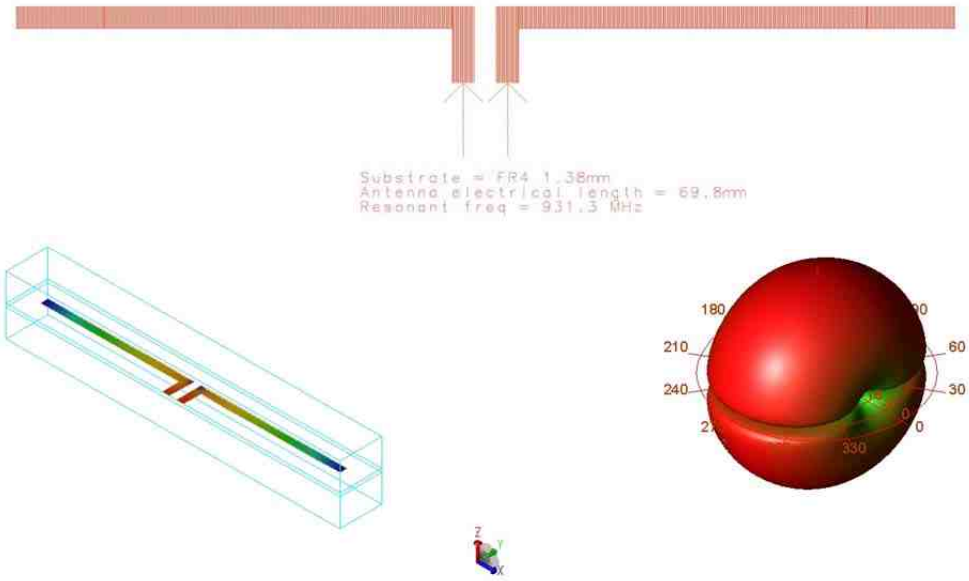

Figure 34. Dipole antenna layout, 3-D visualization and radiation pattern.

A folded dipole was also designed and simulated. Folded dipoles can provide higher gain and directivity. The layout and simulation results are shown in Figure 35. The simulated gain of the folded dipole is 1.52 dB, slightly higher than the straight-line dipole.

المنارة للاستشارات
www.manaraa.com

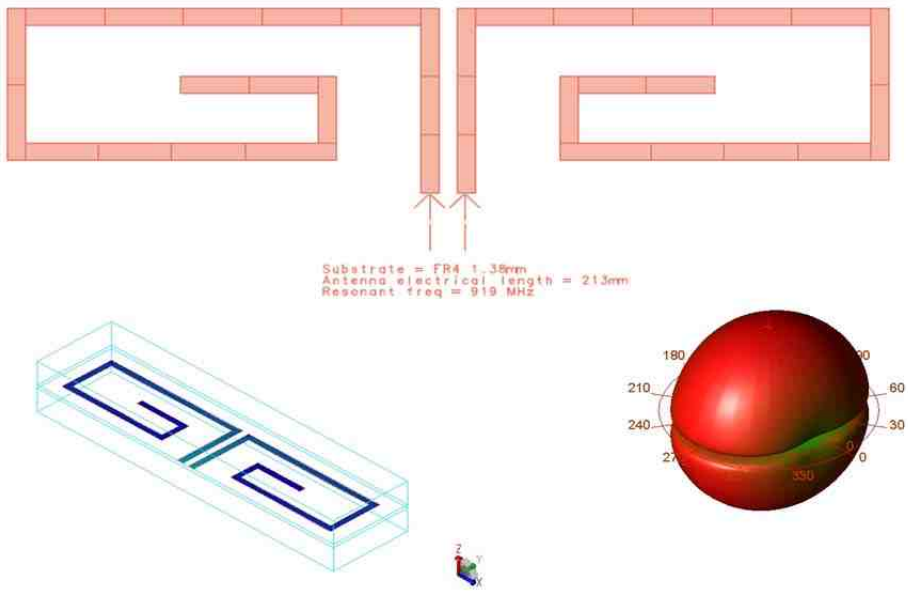

Figure 35. Folded dipole layout, 3-D visualization and radiation pattern.

Doug Jackson of the University of Louisville Wireless and IC Design laboratory, using a LPKF ProtoMAt C30 milling machine, fabricated the antennas on FR-4 printed circuit board. Both antennas were characterized with an Agilent 8714ES network analyzer by measuring the forward transmission parameters (S11). The straight-wire dipole antenna resonated at a frequency of 938 MHz (Figure 36), which is 2.5% higher than the designed frequency of 915 MHz.

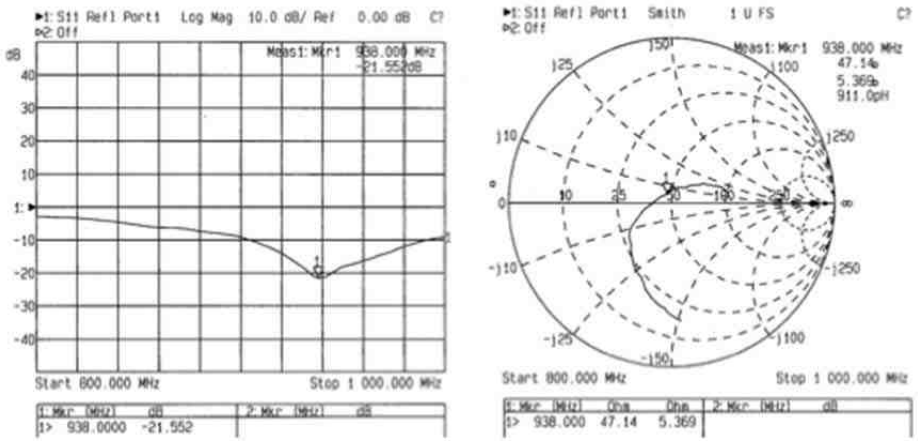

Figure 36. Forward transmission parameters of dipole antenna showing resonant frequency and impedance at resonance.

المنارة للاستشارات
www.manaraa.com

The measured parameters of the folded dipole are shown in Figure 37. The antenna resonated at a frequency of 924.6 MHz, which is only 0.6% higher than the designed frequency of 919 MHz. Comparisons of the simulated and measured parameters of the two antennas are shown in Table 3.

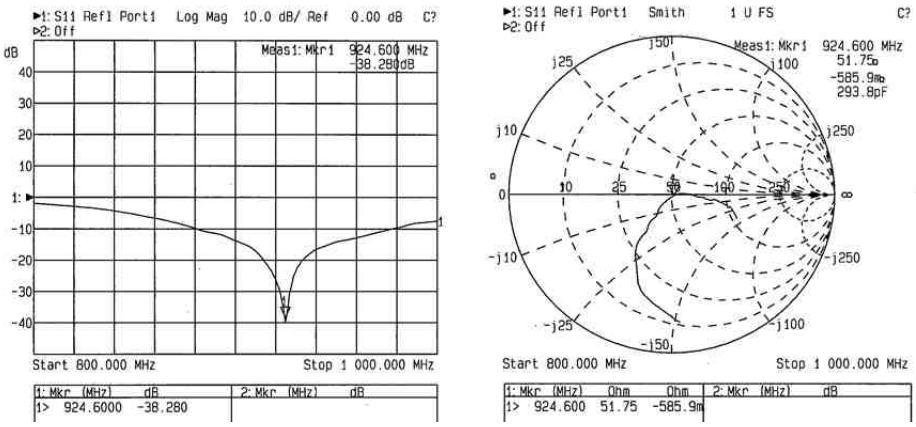

Figure 37. Forward transmission parameters of folded dipole antenna showing resonant frequency and impedance at resonance.

Table 3. Comparison of simulated and measured dipole antenna parameters.

Antenna	Simulated			Measured		
	Resonant Frequency	**SWR at Res Freq**	**Impedance at Res Freq**	**Resonant Frequency**	**SWR at Res Freq**	**Impedance at Res Freq**
Dipole (Orig. substrate parameters: Thickness = 1.5mm, ε_r = 4.4, copper thickness = 35 μm)	914 MHz S11=-35dB	1.026	51.3-j1.25	930 MHz S11=-23dB	1.127	46.87+j5.62
Dipole (Actual substrate parameters: Thickness = 1.38mm, ε_r = 4.0, copper thickness = 17.78 μm)	930.7 MHz S11=-30dB	1.063	53.15-j0.25	930 MHz S11=-23dB	1.127	46.87+j5.62
Folded dipole (Orig. substrate parameters: Thickness = 1.5mm, ε_r = 4.4, copper thickness = 35 μm)	903 MHz S11=-29dB	1.070	51.75-j3.65	930 MHz S11=-25dB	1.130	53.8-j4.76
Folded dipole (Actual substrate parameters: Thickness = 1.38mm, ε_r = 4.0, copper thickness = 17.78 μm)	932.4 MHz S11=-24dB	1.235	61.7+j2.25	930 MHz S11=-25dB	1.130	53.8-j4.76

المنارة للاستشارات
www.manaraa.com

The difference between simulated and measured values was due to not knowing the exact value of the relative dielectric constant of the FR-4 material that was used to fabricate the printed circuit board. The dielectric constant of FR-4 can vary from 4.2 to 4.8, depending on the frequency and the manufacturer [63]. The specific dielectric constant for these printed circuit boards was not available from the manufacturer and equipment to measure the dielectric constant was not available in the lab. Simulated results were produced that were very close to the measured values by performing a simulated parametric sweep of the dielectric constant from 4.2 to 4.8 in steps of 0.1. The printed circuit board dipole antennas were difficult to tune to 915 MHz since the copper traces had to be cut for that purpose. A half-wavelength straight wire dipole was made from 2 mm thick solid copper wire that was soldered to an SMA (Sub-Miniature version A) connector (Figure 38). The wire dipole antenna was tuned by making the two wires of the dipole slightly longer than a quarter wavelength each and then cutting them until the desired resonance frequency was obtained. The wire antenna was designed for 915 MHz and the measured forward transmission parameters (Figure 39) show a resonant frequency of 915 MHz and an impedance of 51 Ohms, which was very close to the standard RF impedance of 50 Ohms.

Figure 38. 915MHz half-wavelength wire dipole antenna.

المنارة للاستشارات
www.manaraa.com

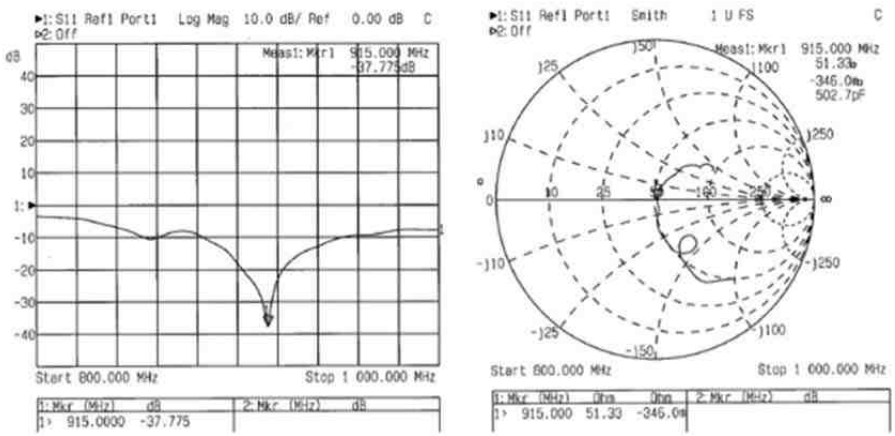

Figure 39. Wire half-wave dipole forward transmission parameters showing resonant frequency and input impedance.

5.4 Electrically Small Antennas

Physically and electrically small antennas were developed that could fit in the space available for intraocular implantation. The antennas were small, resonated at 915 MHz and had an input impedance of 50 Ω. One way of designing antennas that have electrical lengths that are capable of resonance but are physically small is using meandering lines to create a dipole type antenna structure. Electrically small antennas are typically designed using one of two approaches. The first approach is to use a genetic algorithm for the design that uses evolutionary algorithms to find an optimum design based on an initial design choice and design parameters set by the designer. The second approach is an iterative process that uses simulations to find the optimum design. The second approach was used because of the availability of a powerful simulation software package. The Advanced System Design (ADS) software package from Agilent makes use of the method-of-moments numerical computational method to solve linear partial differential equations that describe the boundary conditions associated with antennas.

المنارة للاستشارات
www.manaraa.com

5.4.1 Commercial RFID System Evaluation

An Alien Technology model ALR-9800 Enterprise RFID reader and two circular polarization antennas were evaluated in an effort to better understand the use of ESA's in commercial RFID systems. The ESA's are typically referred to as "tags" in RFID systems. The maximum output RF power of the system is 4 W EIRP. The RFID reader was connected to a PC via an Ethernet cable and was controlled using the Alien RFID Gateway software. The output power was set at maximum for the tests.

5.4.1.1 Test 1

One antenna was connected to the reader and the reader was set to maximum power. Two RFID tags, shown in Figure 40, were placed on plastic containers and moved away from the reader to determine the maximum read range. The "Squiggle" tag was continuously read at a distance of up to 2.5 m and intermittently at up to 3 m and the "Square" tag was continuously read up to a distance of 3m. The tags were found to be very susceptible to the human body and it was not possible to read any of the tags if they were placed closer than 7.5 cm from a human body.

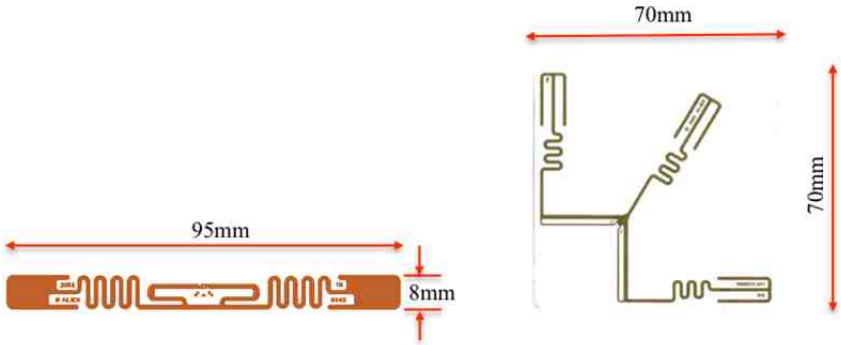

Figure 40. Alien Technology's "Squiggle" tag and "Square" tag.

المنارة للاستشارات
www.manaraa.com

5.4.1.2 Test 2

Test 2 involved the use of two antennas and maximum power, as recommended by the manufacturer. The test setup is shown in Figure 41. One antenna is used for send and one is used for receive. With this configuration, the "Squiggle" tag was read up to a distance of 6m and the "Square" tag up to a distance of 8.2 m. The system was able to read both tags up to a distance of 1 m when loosely held in one hand (tags within 2 mm from hand). The system was not able to read the tags when they were glued to the hand. The system was able to read the "Square" tag at a distance of 0.5 m when it was loosely held between both hands.

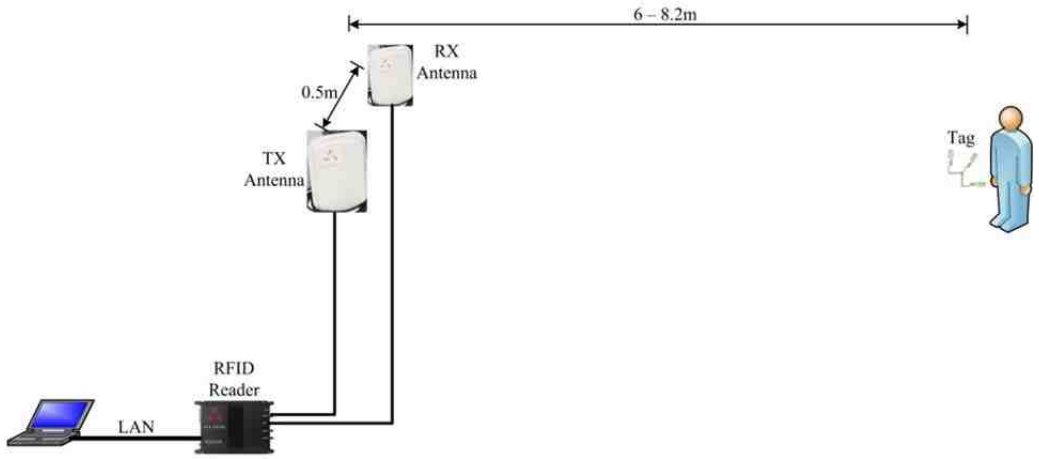

Figure 41. Alien Technology System Test Setup.

5.4.1.3 Test 3

The "Squiggle" tag antenna was modified to see to what extent it would still respond to the reader. The antenna was cut at different points as shown in Figure 42. After the first cut, the reader was able to read the tag at a distance of approximately 1 m. The second cut caused the reading distance to reduce to approximately 0.8 m and resulted in intermittent reading of the tag. The reader was not able to read the tag when the last cut

المنارة للاستشارات
www.manaraa.com

was made. The failure of the reader to read the tag indicated that the antenna is designed and optimized to operate at 915 MHz and any modifications to the antenna caused severe degradation in the performance of the system.

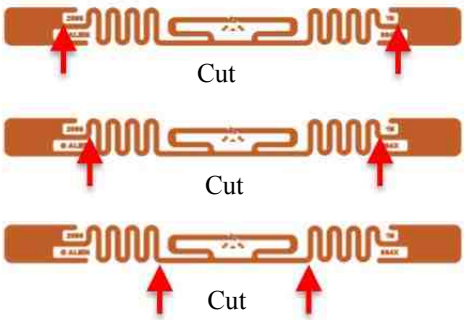

Figure 42. Modifications made to Alien Technology "Squiggle" antenna.

5.4.1.4 Test 4

An Alien "Squiggle" tag was cut at a distance of 5 mm on either side of the chip and connected to a printed circuit board antenna as shown in Figure 43. The configuration as shown in Figure 43 was first tested without the variable capacitor. The system was not able to read the tag. The variable capacitor was then connected as shown in Figure 43. The system was able to read the tag up to a distance of 1.5 m when the capacitance was set to approximately 17 pF. More tests were performed by cutting the solid portions of the PCB antenna at 5 mm intervals starting at the top. The results are summarized in Table 4.

Figure 43. Alien Technology IC connected to PCB antenna and variable capacitor.

المنارة للاستشارات
www.manaraa.com

Table 4. Reading distance of Alien IC with different antenna configurations.

Configuration	Capacitance	Reading distance (m)
Original "squiggle" 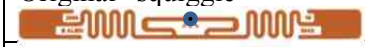	No capacitor	6
Modified antenna	No capacitor	No reading
Modified antenna	Variable cap ≈ 17 pF	1.5
Cut 5 mm from top 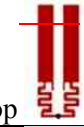	No capacitor	No reading
Cut 5 mm from top	Variable cap ≈ 14 pF	1
Cut 10 mm from top 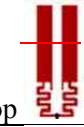	No capacitor	No reading
Cut 10 mm from top	Variable cap ≈ 10 pF	1
Cut 15 mm from top 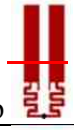	No capacitor	No reading
Cut 15 mm from top	Variable cap ≈ 6 pF	1
Cut 20 mm from top	No capacitor	No reading
Cut 20 mm from top	Variable cap ≈ 1.7 pF	0.8
Cut 20 mm from top	Fixed capacitance ≈ 1.7 pF	No reading
Cut 20 mm from top	Fixed capacitance ≈ 1.7 pF Tag fixture held with back against hand	0.5

The variable capacitor was changed to a fixed capacitance of 1.7 pF; however, the system was unable to read the tag, indicating that the metal bulk of the variable capacitor added to tuning the antenna. When the tag fixture was held with the fingers of a hand

المنارة للاستشارات
www.manaraa.com

pressed directly to the back of the tag, the system was able to read the tag intermittently up to a distance of 0.5 m.

5.4.2 ESA design and development

Three basic characteristics are needed for an antenna to effectively couple electrical energy to free space: gain, impedance matching to the electrical circuit, and a large radiation resistance. These were the main parameters that were used in evaluating the suitability of multiple antenna structures, designed and laid out in ADS, which are shown in Figure 44.

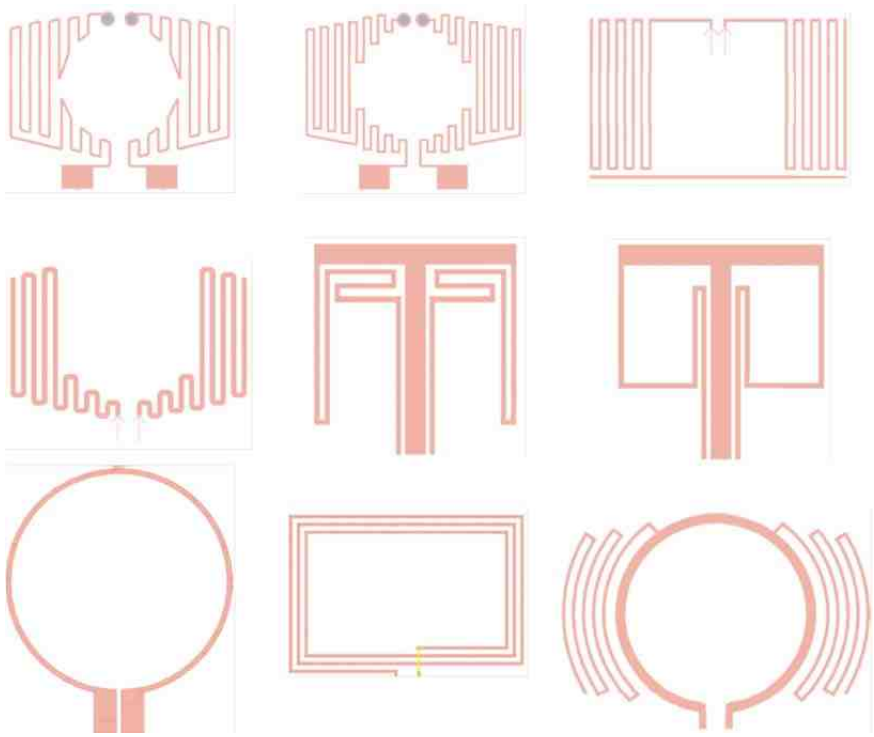

Figure 44. Various electrically small antenna design configurations.

Simulations of these antennas showed a discrepancy in at least one of the main parameters. Two of the antennas were fabricated on FR-4 printed circuit board to

المنارة للاستشارات
www.manaraa.com

measure and compare with the simulation results. The fabricated antenna configurations and the measured results are shown in Figure 45 and Table 5.

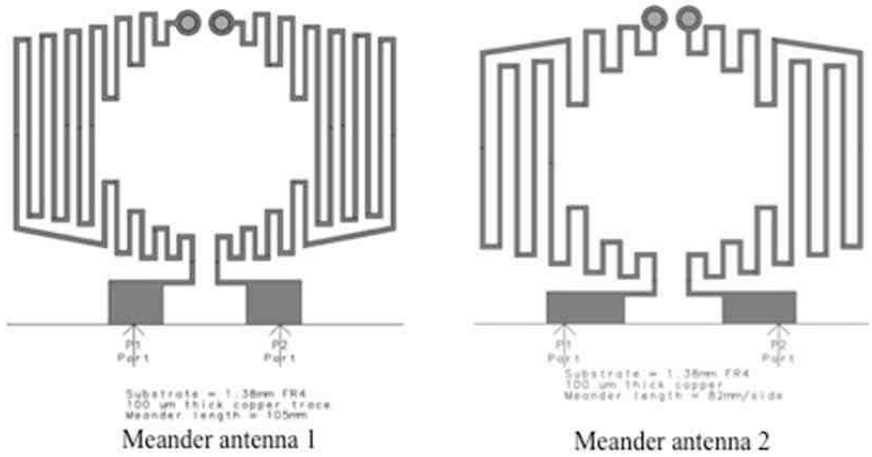

Figure 45. Meander antenna configurations fabricated on FR-4 PCB.

Table 5. Comparison of simulated and measured parameters of ESA's

Antenna	Simulated		Measured	
	Resonant Frequency	**Impedance at Res Freq**	**Resonant Frequency**	**Impedance at Res Freq**
Meander antenna 1 (Orig. substrate parameters: Thickness = 1.5 mm, ε_r = 4.4, copper thickness = 35 µm)	988.6 MHz S11=-8 dB	21.8+j6.9	1170 MHz S11=-8 dB	23.19+j11.7
Meander antenna 1 (Actual substrate parameters: Thickness = 1.38 mm, ε_r = 4.0, copper thickness = 17.78 µm)	1033 MHz S11=-4 dB	10.8+j6.15	1170 MHz S11=-8 dB	23.19+j11.7
Meander antenna 2 (Orig. substrate parameters: Thickness = 1.5 mm, ε_r = 4.4, copper thickness = 35 µm)	1067 MHz S11=-6 dB	17.5-j0.85	1290 MHz S11=-9 dB	34+j27.7
Meander antenna 2 (Actual substrate parameters: Thickness = 1.38 mm, ε_r = 4.0, copper thickness = 17.78 µm)	1123 MHz S11=-7 dB	19.05+j3.8	1290 MHz S11=-9 dB	34+j27.7

The lowest measured resonant frequency was 1170 MHz and both antennas had a Standing Wave Ratio (SWR) greater than 2. Other ESA configurations were investigated that were based on work done by Gosalia et al. [31], who showed that impedance matching of planar meander line antennas were achieved via phase reversal. When a full wavelength dipole antenna is fed a quarter wavelength from one end, the phase of the

المنارة للاستشارات
www.manaraa.com

current distribution changes significantly [10]. The phase reversal is detrimental to the operation of a normal dipole; however, in the case of planar meander antennas, it was used to improve the impedance matching and the directivity. Phase reversal and impedance matching in planar meander line antennas are implemented by incrementally shortening one of the arms of the dipole. The four designs are shown in Figure 46.

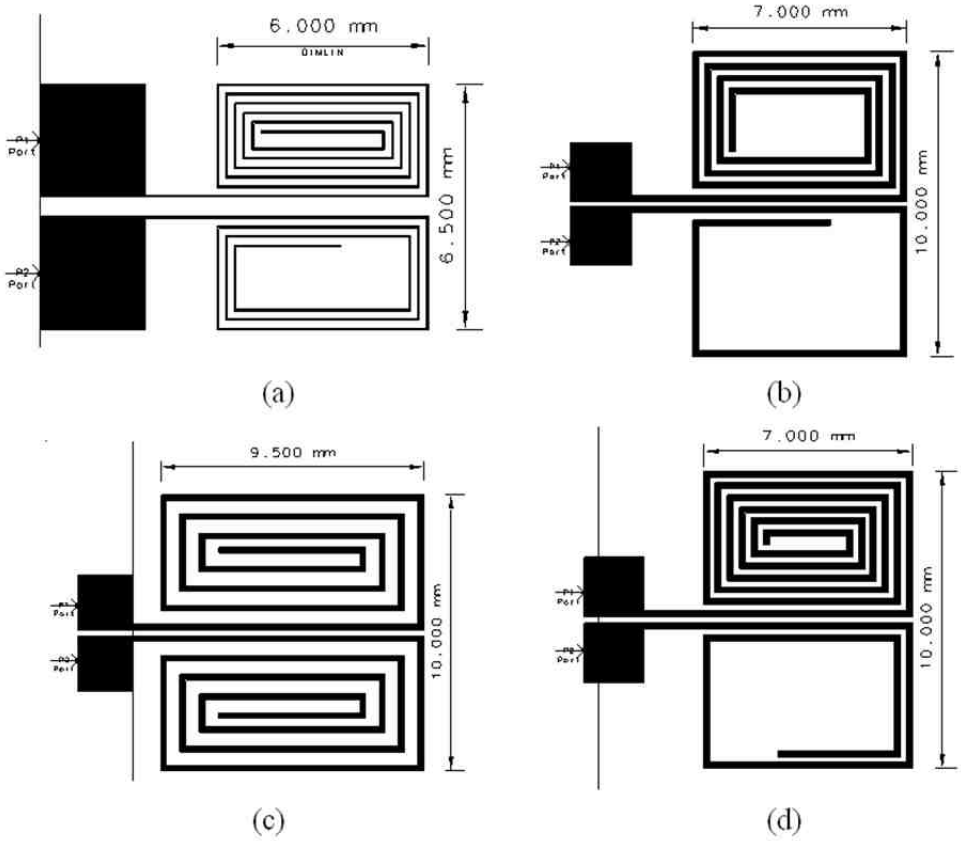

Figure 46. Meander dipole designs. (a) Trace width – 50 µm, separation 200 µm. (b) Optimized for impedance match, trace width 200 µm, separation 200 µm. (c) Optimized for efficiency, trace width 200 µm, separation 500 µm. (d) Optimized for impedance match, trace width 200 µm, separation 200 µm.

The antennas were fabricated on 1.38 mm thick FR-4 printed circuit board (PCB) using a PCB milling machine. Table 6 compares measured and simulated antenna parameters [49]. Resonant frequencies of the fabricated antennas were within 7% of the

المنارة للاستشارات
www.manaraa.com

simulated values, a difference that is attributed to not knowing the exact value of the dielectric properties of the FR-4 substrate, and to the fabrication process.

Table 6. Comparison of simulated and measured antenna parameters.

Ant.	**Simulated**		**Measured**	
	Resonant Freq MHz	**Imp at Res Freq**	**Resonant Freq MHz**	**Imp at Res Freq**
a.	919 S11=-25 dB	45+j0.7	970 S11=-15 dB	38+j8.1
b.	929 S11=-51 dB	50-j0.1	866 S11=-11 dB	30+j9
c.	923 S11=-6 dB	16-j0.3	955 S11=-7 dB	24+j25
d.	845 S11=-30 dB	46-j3	795 S11=-31 dB	48+j0.5

The antennas were made using a milling machine that milled 40 μm deeper than the copper thickness in order to remove the necessary copper and create the traces. This created burrs and some uneven areas around corners that were not taken into account in the simulations. Previous experience with small symmetric meander line antennas has shown fabricated antennas to have resonant frequencies 8–12 % higher than simulated. Antenna (d) was designed to have a resonant frequency lower than 915 MHz. The asymmetric antennas (b) and (d) had measured resonant frequencies lower than simulated as shown in Table 6.

Antennas (b) and (d) were tuned by trimming the longer arm of each of the antennas, resulting in higher resonant frequencies. Antenna (d) showed superior

المنارة للاستشارات
www.manaraa.com

performance in terms of return loss and standing wave ratio. The shorter dipole arm in the meander dipole antennas determines input impedance, while the longer arm affects resonant frequency. The longer arms on the two antennas were incrementally cut until a resonant frequency close to 915 MHz was obtained. The fabricated antennas are shown in Figure 47.

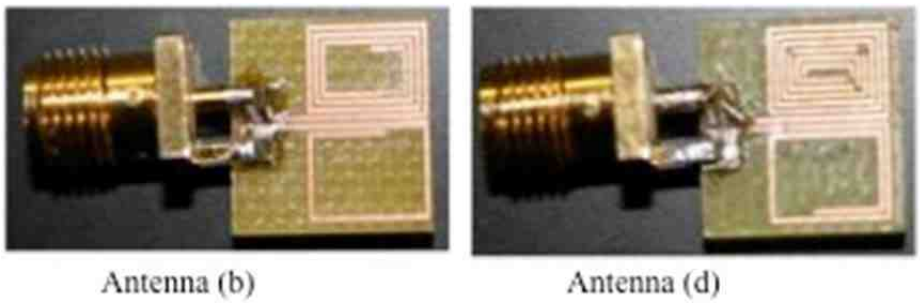

Figure 47: Antennas (b) and (d) after tuning to 915 MHz.

Comparative range measurements were taken on a lab bench with half-wave wire dipole antennas since access to an anechoic chamber was unavailable. A 30 dBm, 915 MHz sinusoidal signal was used as input to a half-wavelength transmitting dipole antenna. A received power of 1.2 dBm was measured on the spectrum analyzer using an identical half-wavelength dipole receiving antenna. The antennas were 1 m apart. The antenna gain for identical antennas used for transmission and reception is given by

$$G_{TX(dB)} = G_{RX(dB)} = \frac{1}{2}\left[20\log\left(\frac{4\pi r}{\lambda}\right) + 10log\left(\frac{P_r}{P_t}\right)\right] \quad (5.1)$$

where r is the distance between the antennas, λ is the wavelength, P_r is the received power and P_t is the transmit power [13]. The gain of the two dipole antennas was calculated as 1.84 dB, which corresponds well with the expected standard gain of 2.1 dB for a half-wave dipole.

المنارة للاستشارات
www.manaraa.com

The receiving dipole antenna was replaced with antenna (b) and (d) respectively and the received power measured. At 915 MHz, a power of -6 dBm was measured with antenna (b) and -8 dBm was measured with antenna (d). Maximum received power for antenna (b) was -4 dBm at 900 MHz and -4.5 dBm for antenna (d) at 905 MHz. The received power of -4 dBm corresponds to a maximum received power of approximately 400 μW at a distance of 1m. Karthaus et al. and Curty et al. demonstrated powering of an RFID transponder with as little as 2.7 μW [16, 24].

Further antenna measurements were made using a -10 dBm signal from the signal generator, and the results are summarized in Table 7. With a 3 dB cable loss, the effective input power to the amplifier was -13 dBm. With a gain of 41 dB, the effective output power of the amplifier was therefore 28 dBm (0.7W). A half wavelength dipole antenna was used as the transmitting antenna. A 1 dB cable loss was measured between the output of the amplifier and the input of the antenna, giving an effective input power to the antenna of 27 dBm (0.5 W). The four ESA's were used as receiving antennas. The antennas were 1m apart over a test bench as shown in Figure 48. The received power was measured using an Agilent E4402B spectrum analyzer. The transmitting antenna was kept horizontal and the receiving antenna was oriented horizontally and vertically to investigate the polarization sensitivity. The power density at the receiving antenna was measured using an Electrosmog model TES593 Electromagnetic Field strength meter. The meter was calibrated to 915 MHz, and was set to measure average power density in W/m^2 at the receiving antenna. The power density measurement was performed to determine a relationship between the power density that surrounds an antenna and the power that is captured by the antenna.

المنارة للاستشارات
www.manaraa.com

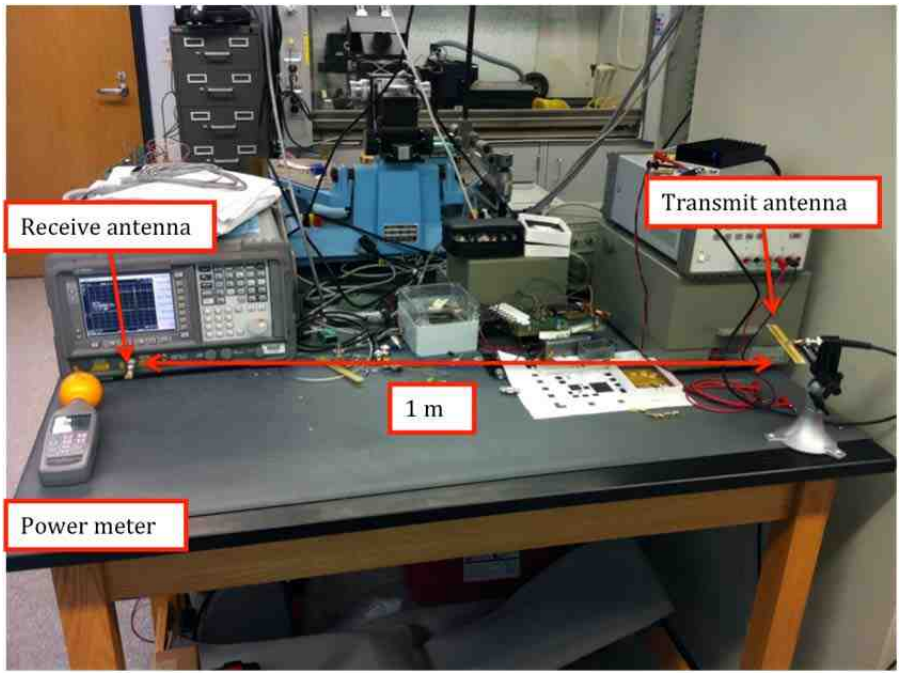

Figure 48. Electrically small antenna test setup.

The fabricated antennas are shown in Figure 49.

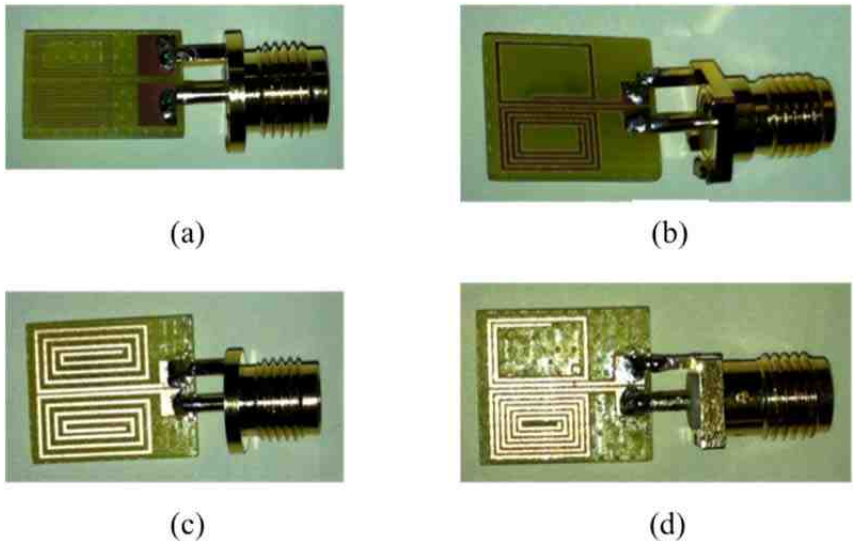

Figure 49: Fabricated ESA meander dipole antennas.

المنارة للاستشارات
www.manaraa.com

Table 7: Measured ESA parameters and performance.

Antenna	**Measured**		**Received power at 915 MHz (dBm)**			**Received power at resonant freq. (dBm)**		
(Substrate parameters: Thickness = 1.38mm, ε_r = 4.0, copper thickness = 17.78 µm)	**Resonant Freq**	**Impedance at Res Freq**	**RX antenna horizontal**	**RX antenna vertical**	**Antenna tuned**	**RX antenna horizontal**	**RX antenna vertical**	**Power density adjusted**
(a) (6 x 6.5 mm) Trace width: 50 µm, Separation 200 µm	970 MHz S11:-15 dB	38+j8.1	-13.4	-13		-2.6	-7	-11.5
Power density @ 1 m			225 mW/m^2			235 mW/m^2		66 mW/m^2
(b) (10 x 10 mm – best match) Trace width:200 µm, Separation: 200 µm	865.5 MHz S11:-11 dB	29.7+j8.95	-16	-19	Res freq: 920MHz -6	-11.1	-16	-21
Power density @ 1 m			225 mW/m^2			224 mW/m^2		63 mW/m^2
(c) (10 x 10 mm – best eff) Trace width: 200 µm Separation: 500 µm	955 MHz S11:-7 dB	24+j25.2	-15.8	-16		-11.8	-15	-25
Power density @ 1 m			225 mW/m^2			243 mW/m^2		65 mW/m^2
(d) (10 x 10mm – rev of ant (b)) Trace width:200 µm, Separation: 200 µm	794.8 MHz S11:-31 dB	47.7+j0.5	-45.5	-40	Res freq: 915MHz -6	-17.3	-18	
Power density @ 1 m			225 mW/m^2			64 mW/m^2		

المنارة للاستشارات
www.manaraa.com

Traces of antennas (b) and (d) were cut to tune the antennas to 915 MHz. The traces of antenna (b) were cut five times to get a resonant frequency of 920 MHz. An exact frequency of 915 MHz could not be obtained; however, 920 MHz was considered close. The cuts are shown in Figure 50 and the characteristic changes are shown in Table 8. Cuts 1 and 2 changed the impedance of the antenna but did not change the resonant frequency. These cuts were therefore restored and cut 5 produced the desired resonant frequency.

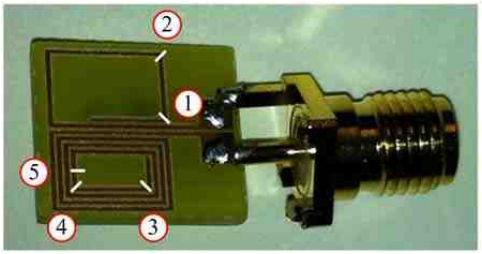

Figure 50. Antenna (b): Cuts made for tuning.

Table 8. Antenna (b) characteristics during tuning

	Measured			Simulated		
Ant. (b) cuts	Resonant Freq (MHz)	S11 at Res. Freq.	Impedance at Res Freq	Resonant Freq (MHz)	S11 at Res. Freq.	Impedance at Res Freq
No cut	865.5	-11 dB	29.7+j8.95	929.2	-51.6	50+j0.1
1	865	-12.5 dB	31.92+j6.68	950	-13 dB	78.6+j3.6
2	865	-13.3 dB	33.31+j8	948	-13 dB	78.8-j3.45
3	880	-13.1 dB	32.61+j6.54	952	-12.4 dB	79.8-j9.35
4	910	-13 dB	31.15+j0.25	974.2	-19.3 dB	41.2+j4.65
5	925	-13 dB	35.32+j14.11	987.2	-18 dB	39.7+j5.1
Cut 2 restored	925	-12.9 dB	34.5+j11.91	983.3	-15.6 dB	35.9+j1.75
Cut 1 restored	920	-13	31.43+j2	979.4	-13.3 dB	32.7+j4.5

المنارة للاستشارات
www.manaraa.com

The traces of antenna (d) were cut four times to get a resonant frequency of 915 MHz. The cuts are shown in Figure 51 and the characteristic changes shown in Table 9. The received power as a function of the transmitted power is shown in Figure 52.

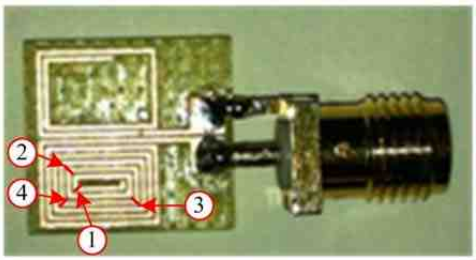

Figure 51. Antenna (d): Cuts made for tuning.

Table 9. Antenna (d) characteristics during tuning.

	Measured			**Simulated**		
Ant. (d) cuts	**Resonant Freq (MHz)**	**S11 at Res. Freq**	**Impedance at Res. Freq**	**Resonant Freq (MHz)**	**S11 at Res. Freq**	**Impedance at Res. Freq**
No cut	794.8	-31 dB	47.7+j0.5	844.5	-30 dB	46.5-j2.5
1	800	-23.67 dB	44.79-j7.44	853.9	-29.8 dB	46.2-j2.85
2	845	-14 dB	36.33+j11.1	885	-28.4 dB	46.35-j0.1
3	880	-12.9 dB	31.84+j5.28	926.2	-21.1 dB	42.4+j2.8
4	915	-13 dB	32.82+j8	975	-14.9 dB	34.8-j0.3

المنارة للاستشارات
www.manaraa.com

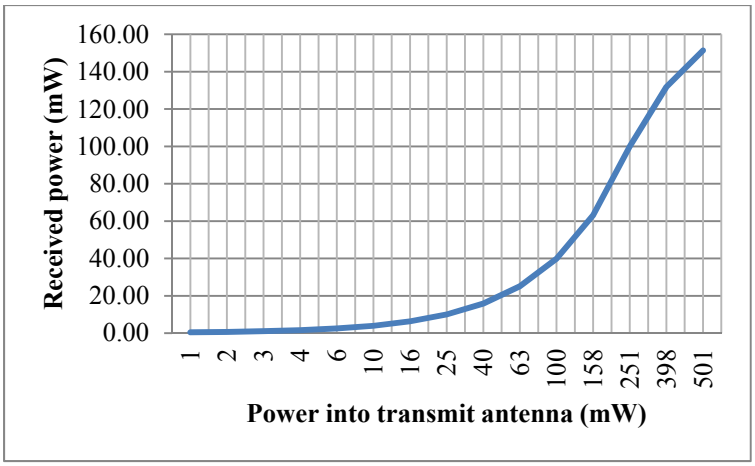

Figure 52. Received power at antenna (d) vs. transmit power.

Friis's transmission equation, for antennas that are matched in terms of reflection and polarization, is given by

$$\frac{P_r}{P_t} = \left(\frac{\lambda}{4\pi r}\right)^2 G_t G_r. \tag{5.2}$$

The free-space loss factor is $\left(\frac{\lambda}{4\pi r}\right)^2$. At a frequency of 915 MHz and a distance of 1m, the free space loss factor is 0.681 x 10^{-3}, or -31.7 dB. Therefore, with 0 dBm into the transmitting antenna and assuming the typical gain of 2.2 dB for a half-wave dipole, the received power at a distance of 1m is 0 + 2.2 – 31.7 = -29.5 dBm. The received power, measured on an Agilent E4402B spectrum analyzer and using antenna (d) tuned to 915 MHz, was -34 dBm. The difference between the received power of the ESA and the half-wave dipole gives a loss factor of 4.5 dB (or a gain of -4.5 dB) associated with antenna (d). The factor of 4.5 dB is a surprisingly good loss factor, considering the geometry of the antenna. One side of this "folded-dipole" has a total length of λ/4.8 and the other side

المنارة للاستشارات
www.manaraa.com

has a total length of only λ/8.4.The antenna characteristic values shown in Tables 8 and 9 were obtained by using ADS simulations and measurements made in the laboratory using a network analyzer. Typical simulation results for antenna (d) are shown in Figure 53 and the measured antenna characteristics before and after tuning are shown in Figure 54.

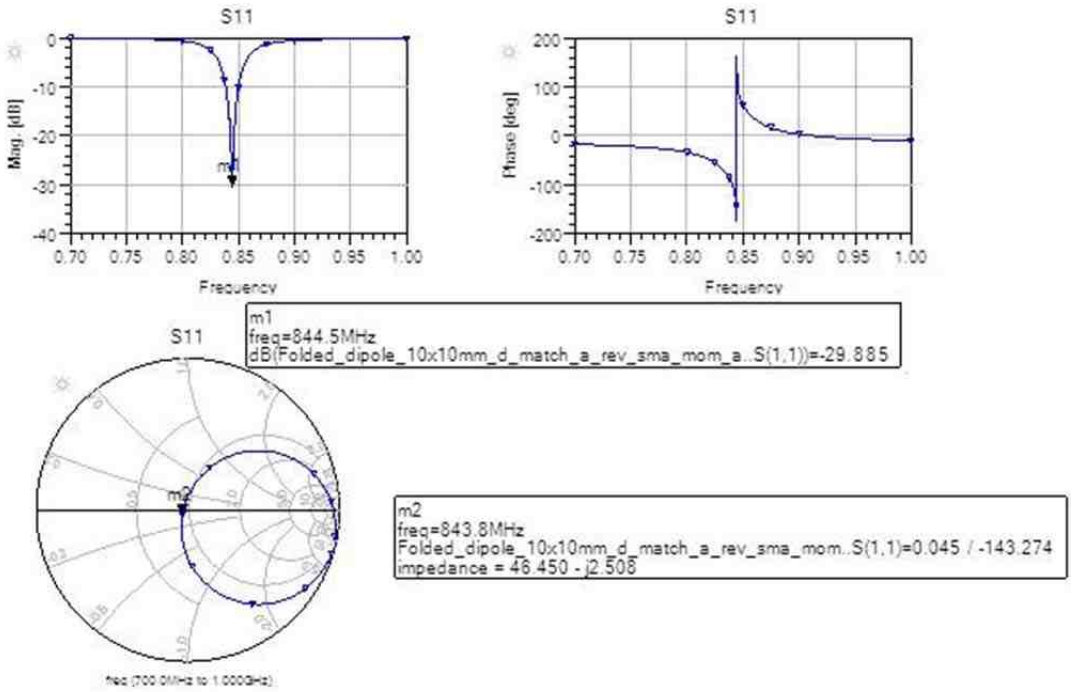

Figure 53. Simulated forward transmission parameters and impedance for antenna (d).

المنارة للاستشارات
www.manaraa.com

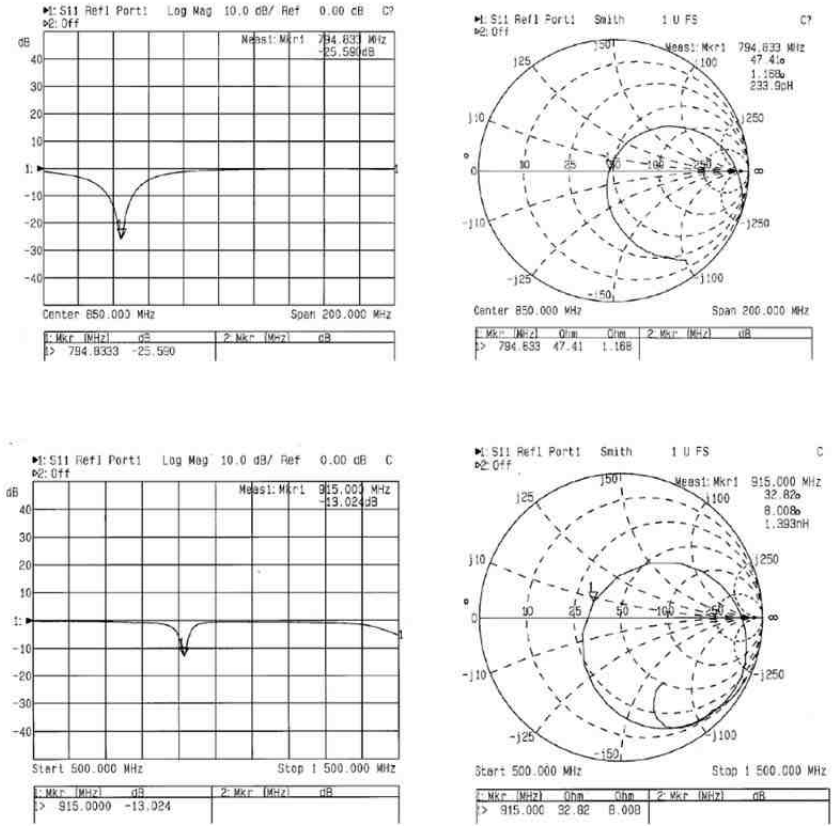

Figure 54. Measured parameters for antenna (d) before (top) and after (bottom) tuning.

Two of the electrically small antennas were evaluated with regard to their quality factor. The first antenna (antenna (a)) has a physical size of 6 x 6.5 mm and the second (antenna (d)) has a physical size of 10 x 10 mm. The antennas were designed and simulated using Agilent ADS (Advanced Design System). The antenna designs are shown in Figure 55.

المنارة للاستشارات
www.manaraa.com

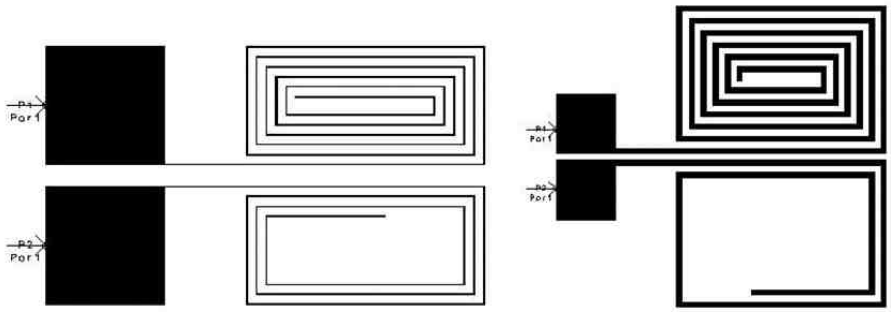

Figure 55. Antenna (a) Antenna (d).

The return loss simulations for the two antennas are shown in Figure 56. The simulated bandwidth for antenna (a) is 17 MHz, resulting in a Q factor of 54. The simulated bandwidth for antenna (d) is 14 MHz, resulting in a Q factor of 70.

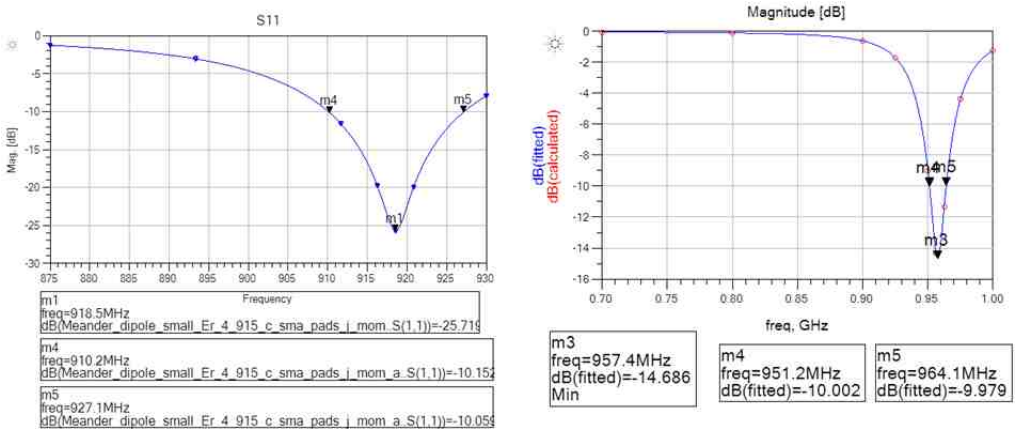

Figure 56. Return Loss: Antenna (a) Antenna (d).

The Q of both antennas was measured using two methods. The first method involves measuring the return loss (S11) using an Agilent 8714ES network analyzer. The antenna bandwidth is measured by taking the band of frequencies where the return loss is less than -10 dB [44]. The measured return loss of both antennas is shown in Figure 57.

المنارة للاستشارات
www.manaraa.com

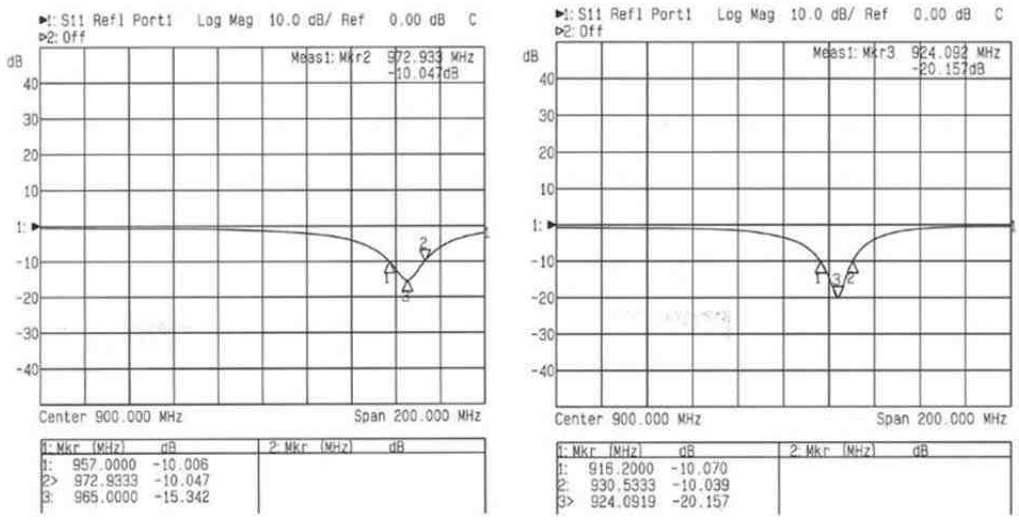

Figure 57. Return Loss: Antenna (a) Antenna (d).

The -10 dB bandwidth of antenna (a) is measured as 16 Mhz and that of antenna (d) as 14 MHz, resulting in a Q factor of 60 for antenna (a) and 66 for antenna (b).

The second method makes use of an Agilent 8648C signal generator and an Agilent E4402B spectrum analyzer. The antenna being tested was used as the transmitting antenna and a wire dipole antenna was used as the receiving antenna. The antennas were separated by a distance of 1m. A sinusoidal signal of -15dBm was generated from the signal generator and used as input to a 41 dB power amplifier. The output of the amplifier was used as input to the transmitting antenna. An overall cable loss of 4 dB was measured, giving an effective input power to the antenna of 22 dBm. The frequency of the signal generator was adjusted until maximum power was received at the spectrum analyzer. The frequency of the signal generator was then further adjusted to find the upper and lower frequencies at which the received power is 3dB down from the maximum. The bandwidth of antenna (a) was measured as 30 MHz with a maximum received power at 903 MHz, giving a Q factor of 30. The bandwidth of antenna (b) was

المنارة للاستشارات
www.manaraa.com

measured as 29 MHz with a maximum received power at 904 MHz, giving a Q factor of 31.

The theoretical Q for each antenna was calculated using a relationship derived by McLean [43] and given by

$$Q = \frac{1}{(ka)^3} + \frac{1}{ka}, \tag{5.3}$$

where k is the wave number (2π/λ) and a is the radius of the smallest sphere that encloses the antenna. The theoretical Q factors of the two antennas at their measured resonant frequencies were calculated using equation 4.11. Using a resonant frequency of 965 MHz for antenna (a) and a sphere radius of 6.45 mm, gives a Q factor of 451. A Q factor of 429 was calculated for antenna (d) using a resonant frequency of 924 MHz and a sphere radius of 6.85 mm.

The theoretical, simulated and measured Q factors of the two antennas are summarized in Table 10. There is good correlation between the simulated Q and the Q measured with the network analyzer, but these values are much lower than the theoretical Q. The reason for this discrepancy is unclear. The lower values measured on the spectrum analyzer were attributed to the dipole antenna used as receiving antenna, since the bandwidth of the dipole antenna is small.

Table 10. Theoretical, Simulated and measured Q for antennas (a) and (d).

Antenna	**Theoretical Q**	**Simulated Q**	**Measured Q**	
			Network analyzer	**Spectrum analyzer**
1	451	54	60	30
4	429	70	66	31

المنارة للاستشارات
www.manaraa.com

The upper limit for the gain of an electrically small antenna was determined by using [44]

$$G = (ka)^2 + 2ka. \tag{5.4}$$

The maximum possible gain for antenna 1 is -5.6 dBi and the maximum possible gain for antenna 4 is -5.5 dBi. The actual gains were not measured since no anechoic chamber was available.

Accurate antenna measurements are performed in indoor or outdoor antenna ranges. Indoor antenna ranges consist of anechoic chambers. Anechoic chambers have electromagnetic absorbing walls and shield the antenna under test from external electromagnetic fields. The measurement results shown in Table 10 were not obtained in an anechoic chamber and could have been subject to external electromagnetic interference. It has also been reported that special care should be taken when making measurements on electrically small antennas [64]. Staub et al. found that the shielding of the coaxial cable that feeds the antenna radiates as much or even more than the antenna under test. The measured gain and bandwidth will therefore be that of the radiator formed by the antenna and the feeding cable.

The performance of one of the ESA antennas (antenna (b)) together with the RF rectifier circuit was evaluated with increased transmitter power. Both transmit and receive antennas were at the same height of 16.5 cm above the table. The antennas were both horizontal and in-line with each other. A -2 dBm, 915 MHz sinusoidal signal was generated by the signal generator and used as input to the power amplifier. Cable losses

المنارة للاستشارات
www.manaraa.com

were measured as 2 dB resulting in an EIRP of 36 dBm (4 W). The test setup is shown in Figure 58.

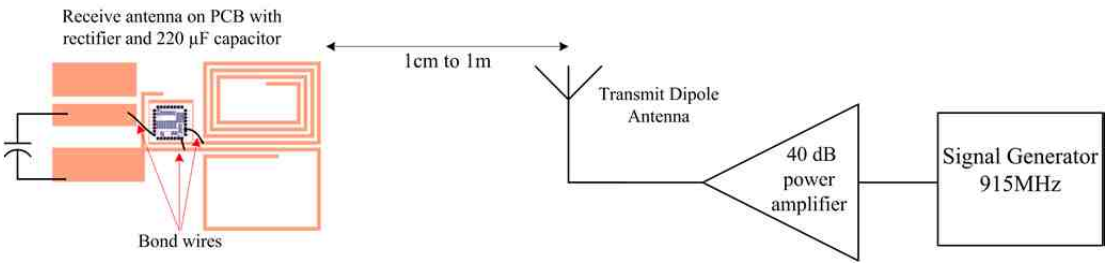

Figure 58. Test setup to measure ESA performance with increased transmitter power.

In all cases, the transmitter was activated for 1 minute and then switched off. The voltage across the storage capacitor (220 μF) was measured directly after the transmitter was switched off. The results of the tests are shown in Figure 59.

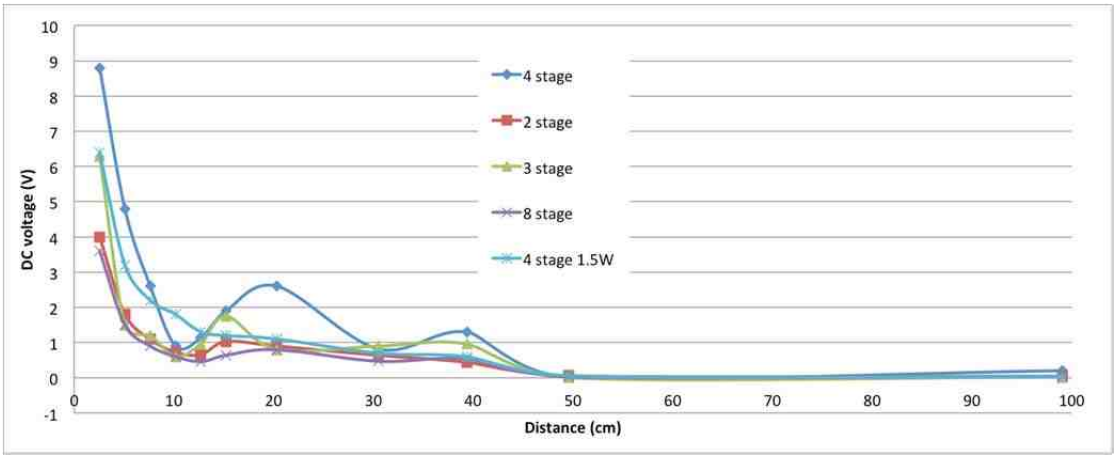

Figure 59. DC voltage generated by multistage rectifiers .

The reason for the sudden increase in dc output at 20 and 40 cm is unclear. This behavior was not seen in earlier tests when a transmit power of 1.5 W was used. Harmonics associated with the transmitted signal can cause an increase in the received signal power if they constructively interfere with the fundamental signal. To test for the presence of harmonic signals, a dipole antenna was connected to a spectrum analyzer and

المنارة للاستشارات
www.manaraa.com

separated a distance of 20 cm away from the transmitting dipole antenna. The output of the power amplifier was measured on the spectrum analyzer over a frequency span from 0 to 3 Ghz. With a transmit power (EIRP) of 36 dBm (4W), the received signal at 915 MHz was 16.6 dBm with harmonic signals at 1.83 GHz (-24 dBm) and 2.745 GHz (-14 dBm). It is unlikely that these weak harmonic signals contribute to the increased dc output voltage seen at 20 and 40 cm.

Tests were also performed on small loop antennas (12mm diameter) to evaluate their performance in the near field. The performance of these antennas was much worse than the small dipole antenna. The highest dc output voltage generated was only 0.3 V at a distance of 2.54 cm. This poor performance is mainly due to the small loop not being resonant at 915 MHz.

5.4.2.1 Electrically small antenna in saline solution

One of the ESAs (antenna (b)) was inserted in a saline solution to evaluate the detuning effect when the antenna is enclosed by a medium other than free space. The antenna configuration is shown in Figure 60. Simulations were performed in ADS to compare with the measured results and to determine if accurate simulations could be used to predict the performance of electrically small antennas in an implanted environment.

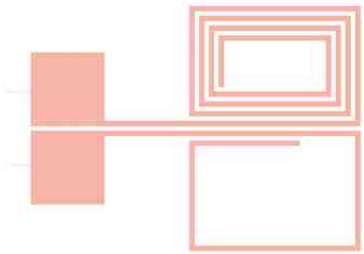

Figure 60. Antenna configuration (b) used in saline solution test.

المنارة للاستشارات
www.manaraa.com

Advanced Design System has the capability to perform 3D electromagnetic (EM) simulations using either the Method of Moments (MoM) 3D planar EM simulator or the Finite Element Method (FEM) for full wave 3D simulation. Simulations were performed using both methods. Both of these methods are better suited to planar structures where it is assumed that the horizontal dimensions of the substrate are much larger than the vertical dimensions. According to Agilent Support, finite sized substrates can only be defined using a dielectric via in FEM. Finite sized substrates were defined in FEM and simulations were performed using both FEM and MoM for comparison. The antenna was first enclosed in plastic to model and measure the effect of the plastic. The simulated and measured results are shown in Figures 61 to 63.

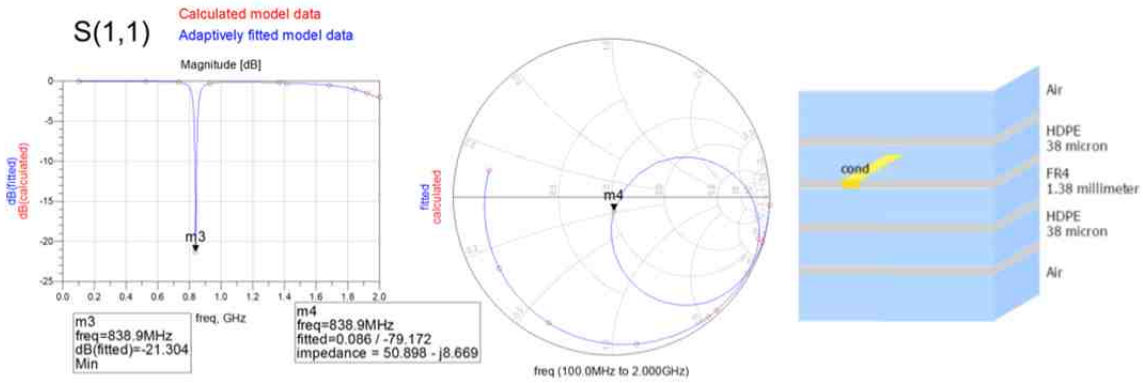

Figure 61. MoM simulation results for antenna (b) in plastic. Substrate definition is shown on right.

المنارة للاستشارات
www.manaraa.com

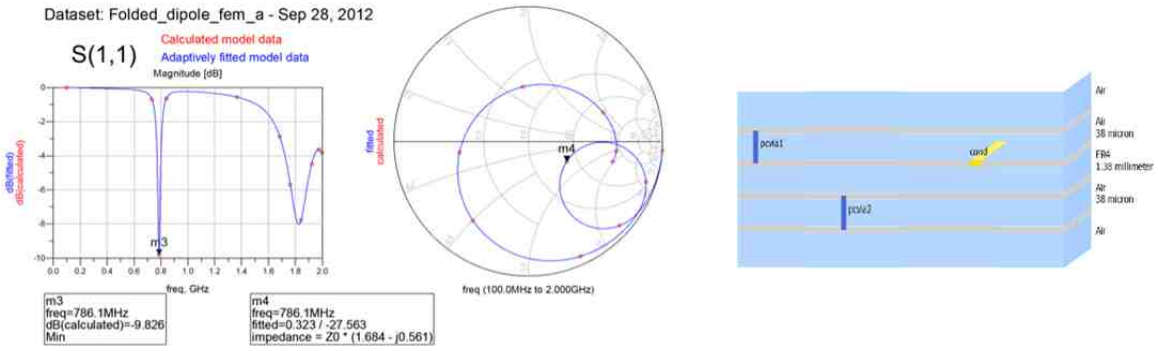

Figure 62. FEM simulation results for antenna (b) in plastic. Substrate definition is shown on right.

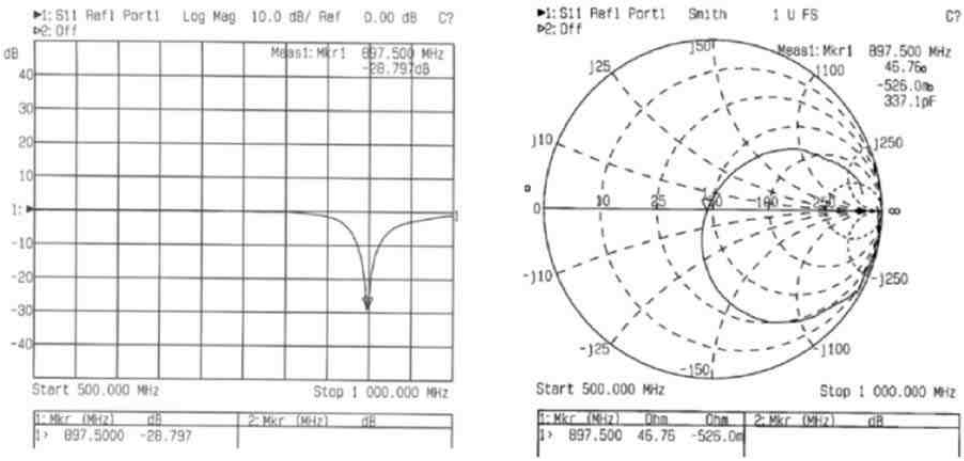

Figure 63. Measured results for antenna (b) in plastic.

The antenna was detuned slightly to 897.5 MHz from its original resonant frequency of 920 MHz. The resonant frequency of the MoM simulation was 58.6 MHz or 7% lower than the measured resonant frequency and the resonant frequency of the FEM simulation was 111.4 MHz or 13% lower than measured. The antenna, enclosed in plastic, was inserted 5 cm into a 10 cm diameter Pyrex glass beaker filled with a saline solution that had the same dielectric properties as the aqueous humor in the eye. The simulated and measured results are shown in Figures 64 to 66.

المنارة للاستشارات
www.manaraa.com

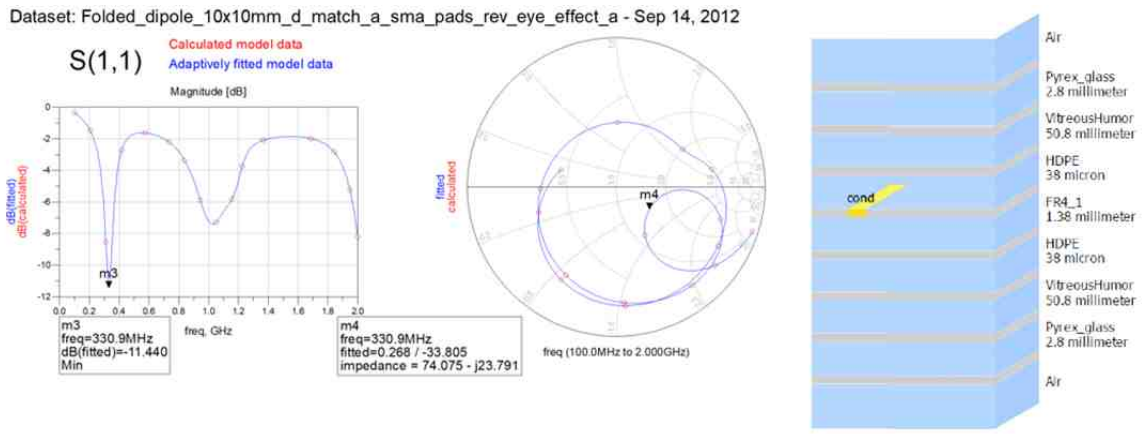

Figure 64. MoM simulation results for antenna (b) in saline solution. Substrate definition is shown on right.

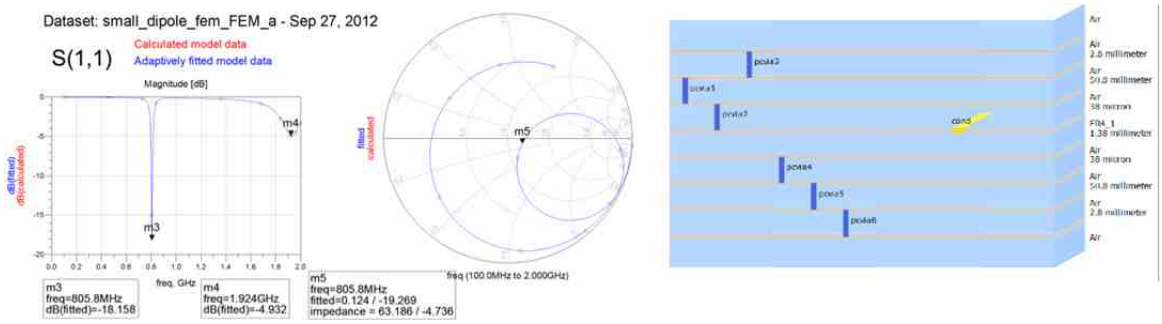

Figure 65. FEM simulation results for antenna (b) in saline solution. Substrate definition is shown on right.

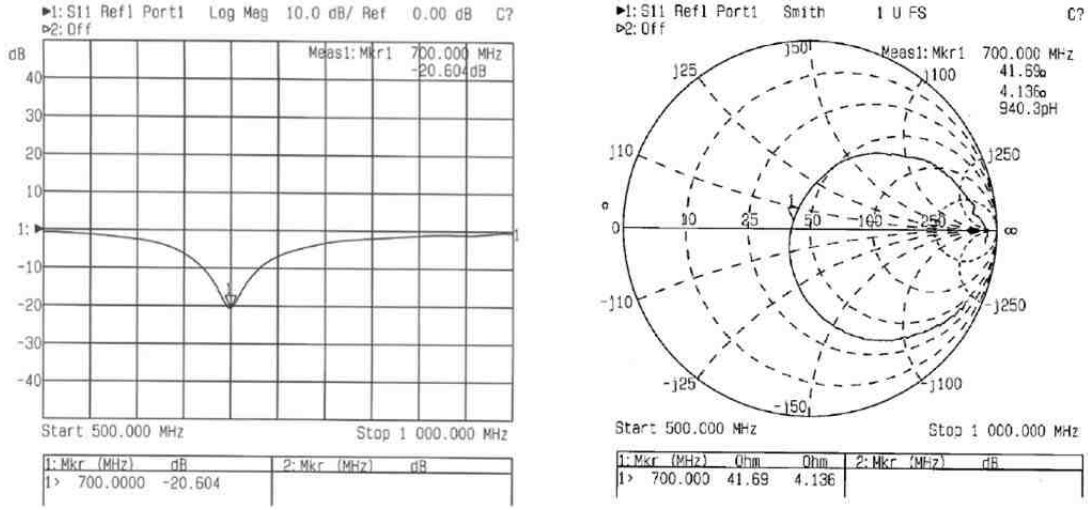

Figure 66. Measured results for antenna (b) in saline solution.

المنارة للاستشارات
www.manaraa.com

The saline solution detunes the antenna even further, down to a resonant frequency of 700 MHz. The simulated resonant frequency, using MoM, is approximately half of the measured resonant frequency. Thickness limits are only placed on the vertical parts of the substrate layers; however, the horizontal lengths are considered infinite. The FEM simulation resonant frequency is closer to the measured results; however, there is some uncertainty regarding the correctness of the substrate definition.

5.4.3 Commercial antenna tests

Two commercial Yagi antennas, with known characteristics, were compared to the performance of the designed and fabricated antennas. Tests were performed outdoors to reduce interference and multipath signal effects. The tests were conducted over a wet grassy area and the received power was measured using an Agilent spectrum analyzer. The received power was measured at different distances using three different antennas. The receiving antennas were a 9 dBi Yagi, a 2.15 dBi half-wavelength dipole, and a 6 dBi circularly polarized RFID antenna from Alien Technologies respectively. A 9 dBi Yagi antenna was used as the transmitting antenna. The transmit antenna was connected to an Agilent signal generator that generated a 0 dBm, 915 MHz signal, resulting in an effective transmit power of 6.85 dBd. Both antennas were at a height of 1.37 m above the ground. All the antennas were configured for horizontal polarization, except the Alien Technologies antenna, which is circularly polarized. The results of the tests are shown in Figure 67.

المنارة للاستشارات
www.manaraa.com

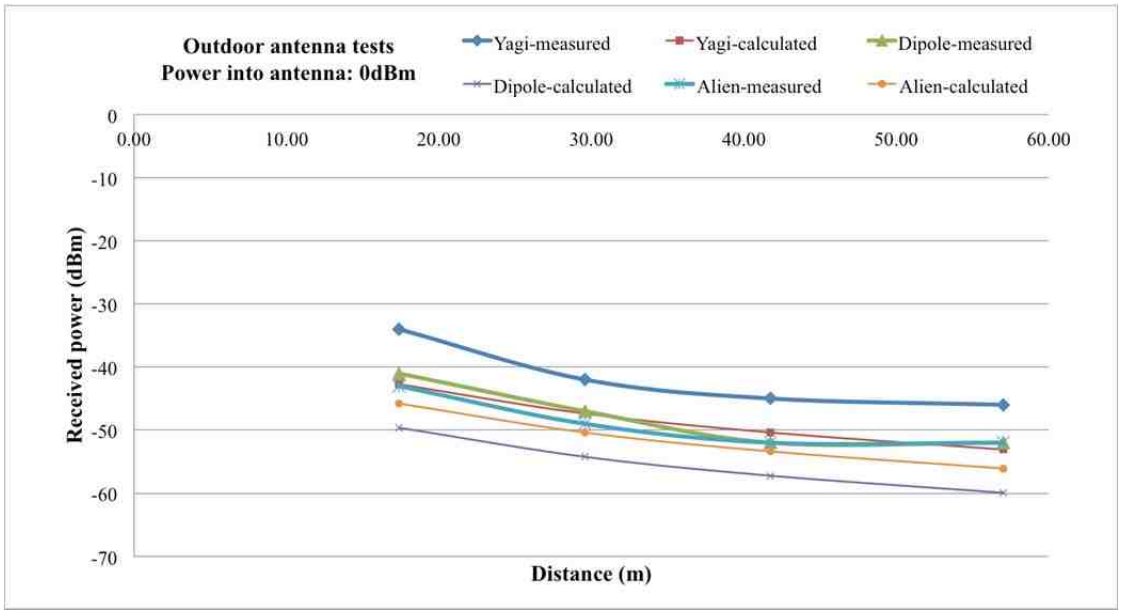

Figure 67. Comparison of measured and calculated received power for three different antennas.

The measured data was compared with calculated values. The measured data was on average 6.7 dB higher for the Yagi antenna, 7.3 dB for the dipole and 2.4 dB for the Alien antenna. The higher measured data is attributed to ground reflection of the RF waves.

The received power using the Yagi antenna was on average 6.25 dB higher than the dipole. This correlates well with the 6.85 dBd gain of the Yagi antenna. The dipole antenna performed better or equal to the 3.85 dBd Alien Technologies antenna.

The effect of changes in the angle between transmitting and receiving antennas was also measured using the Yagi antennas. The receiving antenna was rotated in 30-degree increments at various distances and the received power measured on the spectrum analyzer. No discernible signal was measured when the receiving antenna was at a 90-

المنارة للاستشارات
www.manaraa.com

degree angle with respect to the transmitting antenna. The results are shown in Figure 68 and confirm the expected decrease in received power with an increase in the angle between the two antennas.

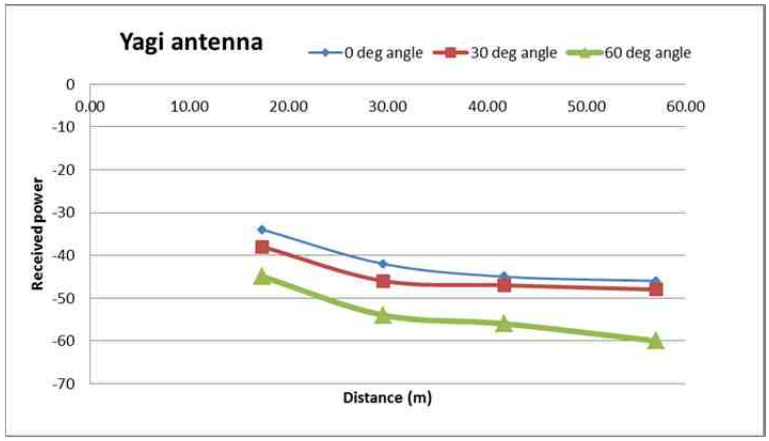

Figure 68. Received power vs angle and distance for the Yagi antenna.

The near field of the Yagi antenna was investigated. A 9 dBi Yagi antenna was used as the transmitting antenna. The transmit antenna was connected to an Agilent signal generator that generated a 0 dBm, 915 MHz signal resulting in an effective transmit power of 6.85 dBd. Both antennas were at a height of 1.37m above the ground. The tests were conducted over a wet grassy area and the received power versus distance was measured using an Agilent spectrum analyzer. The antennas were configured for horizontal polarization. The results of the tests are shown in Figure 69.

المنارة للاستشارات
www.manaraa.com

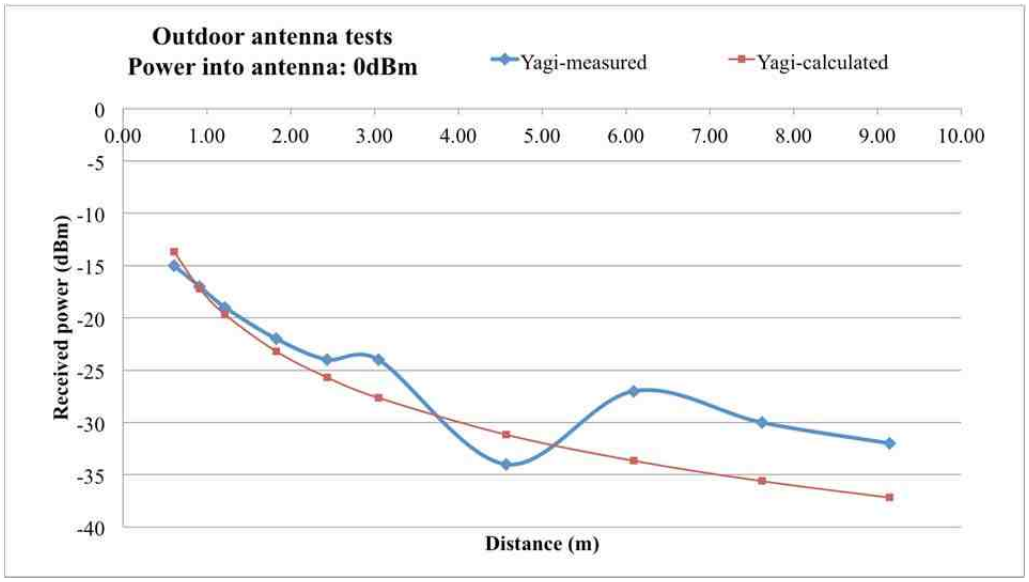

Figure 69. Near-field measured and calculated received power vs distance.

The received signal power dropped by up to 10 dB when the distance between the two antennas was between 4 and 5 m. The reason for this behavior is unclear. Similar behavior was observed when the antennas were tested on the balcony of a building.

There is strong correlation between the measured and calculated received power in the range from 0.6 m to 2.5 m. This is in contrast to the results obtained in the laboratory when the Yagi antenna was used as transmitting antenna to power a rectifier circuit. The Yagi antenna performed on average 40% worse than a half-wave dipole antenna over a distance of 1m and less in the laboratory.

المنارة للاستشارات
www.manaraa.com

CHAPTER 6. CIRCUIT DESIGN AND DEVELOPMENT

6.1 Application Specific Integrated Circuit (ASIC) Designs

This section discusses the design process and development and includes simulations that were performed using a variety of simulation packages. Several ASICs were designed and integrated circuit layouts were created using LEDIT from Tanner Tools. The first ASIC was fabricated by the MOSIS service using AMI Semiconductor's 1.5 µm process. All subsequent ASICs were fabricated by the MOSIS service using the OnSemi 0.5 µm C5 process. A block diagram of the proposed system is shown in Figure 70 and the system design process is shown in Figure 71.

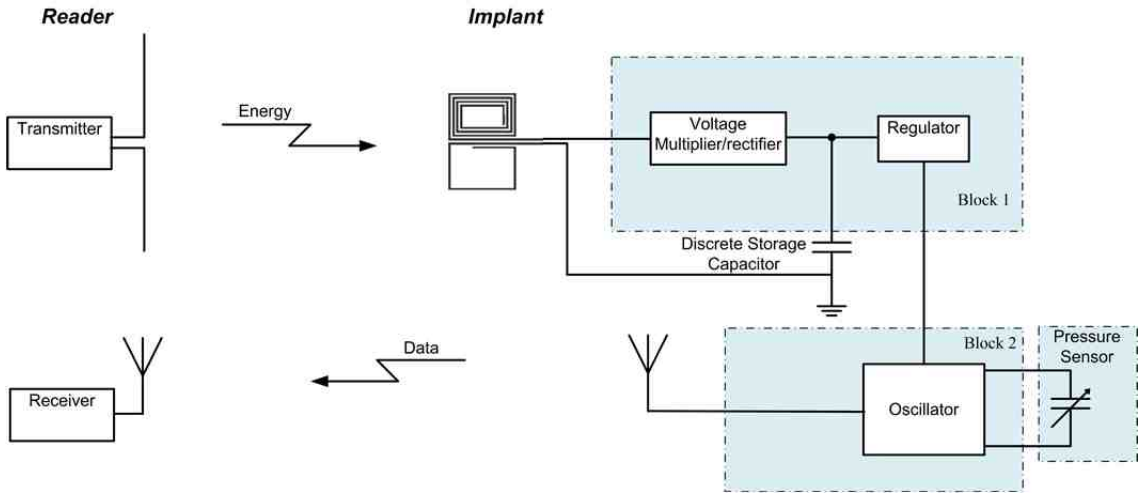

Figure 70. Block diagram of implantable transponder.

المنارة للاستشارات
www.manaraa.com

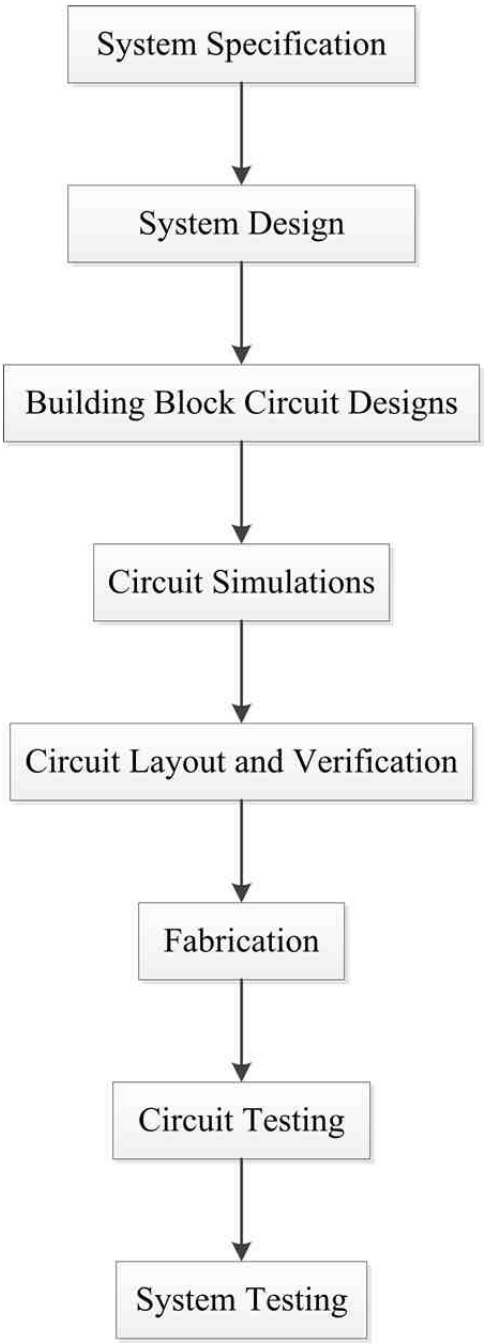

Figure 71. System Design Process Flow.

المنارة للاستشارات
www.manaraa.com

6.2 Oscillator Design

Three oscillator circuit configurations were investigated for use in the implantable transponder. The circuit configurations included a voltage-controlled oscillator, an RC multi-vibrator oscillator and a Colpitts oscillator. The circuits were simulated in T-Spice from Tanner Tools.

6.2.1 Voltage Controlled Oscillator (VCO)

The VCO circuit shown in Figure 72 was simulated in T-Spice and evaluated with regard to frequency of oscillation and power supply requirements. The design of this oscillator was based on a design included in Baker [59]. The VCO simulation showed a constant output voltage of 1.8 V with Vdd = 5 V, Vinvco =2.4 V and a capacitance of 1.2 pF.

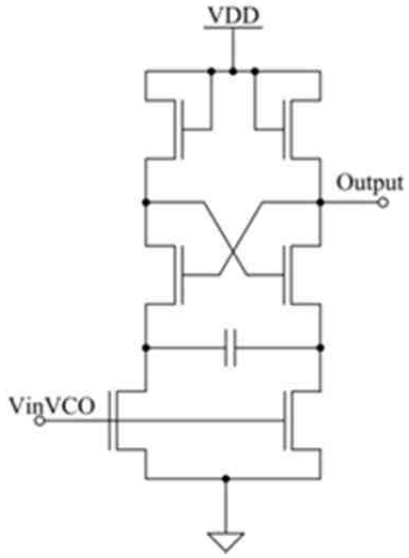

Figure 72. Voltage controlled oscillator circuit schematic.

المنارة للاستشارات
www.manaraa.com

Changing the C value from 1.1 pF to 1.2 pF, an output signal was generated that oscillated between 0.8 V and 3.4 V with a frequency of 102 MHz. The frequency corresponds well with the calculated frequency of 104 MHz using [59]

$$f_{osc} = \frac{I_D}{4 \cdot C \cdot V_{th}} \tag{6.1}$$

with I_D = 300 μA and V_{th} = 0.6 V. The simulated oscillator failed to function when the supply voltage was lower than 5 V. The high supply voltage requirement is not realistic for a wirelessly powered application since the oscillator must be able to function with a supply voltage between 1 V and 3 V. Assuming that the oscillator draws 300 μA and Vth = 0.6 V, then a capacitance of 136.6 fF is required to get an oscillation frequency of 915 MHz. This capacitance is dominated by the parasitic capacitances of the MOSFET's and the bond pads. If a capacitance of 1pF is used, then a current of 2.2 mA is required to get oscillations at 915 MHz. The current requirement of 2.2 mA is too high for a passive transponder application. The VCO oscillator configuration was therefore not considered viable for a wirelessly powered application.

6.2.2 RC Multi-vibrator Oscillator

The circuit schematic for an RC multi-vibrator oscillator is shown in Figure 73.

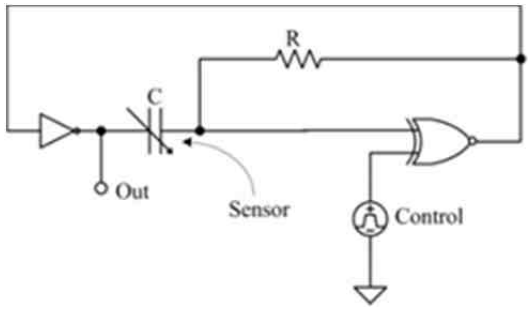

Figure 73. RC Multivibrator oscillator schematic.

المنارة للاستشارات
www.manaraa.com

The oscillation frequency is given by

$$f_{osc} = \frac{1}{2.2RC} \tag{6.2}$$

For an oscillation frequency of 915 MHz, the capacitance values shown in Table 11 are required with different values of the feedback resistor.

Table 11. Capacitance vs resistance values for RC oscillator.

R(Ω)	f_{osc}	C (F)
100	9.15E+08	4.97E-12
1000	9.15E+08	4.97E-13
10000	9.15E+08	4.97E-14
100000	9.15E+08	4.97E-15

The only realistic capacitance values correspond to resistance values of 100 Ω and 1000 Ω, with values of 5 pF and 0.5 pF, respectively. The low resistance values will result in unacceptable large current flow in the circuit. With a capacitance value of 1 pF and R=100 kΩ, the simulated output frequency is 4 MHz. This corresponds well with the calculated frequency of 4.5 MHz. A maximum frequency of 13.5 MHz is simulated with a resistance value of 20 kΩ and capacitance of 1 pF. It is not practical to obtain an oscillation frequency of 915 MHz from this oscillator configuration.

6.2.3 Colpitts Oscillator

The design process was started by designing a discrete Colpitts oscillator using a RF Bipolar Junction Transistor (BJT). The initial design was based on a Surface Acoustic Wave (SAW) stabilized Colpitts oscillator as shown in Figure 74. The transistor was an MMBTH10 NPN RF transistor and the SAW device was a RO2053 310 MHz single port resonator.

المنارة للاستشارات
www.manaraa.com

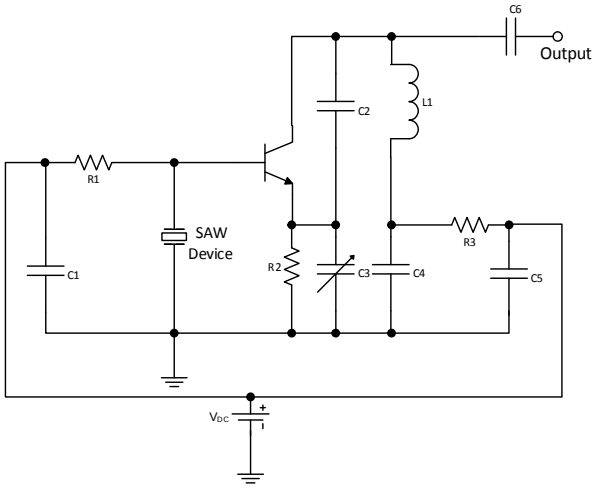

Figure 74. SAW based Colpitts oscillator circuit schematic.

The variable capacitor (C3) represents the capacitive pressure sensor. The oscillator circuit was implemented using a custom printed circuit board (PCB) as shown in Figure 75. The layout of the circuit board was performed in Circad and fabricated using a LPKF ProtoMat C30 milling machine. The oscillator provided a stable output signal over the full range (1 – 30 pF) of the variable capacitor.

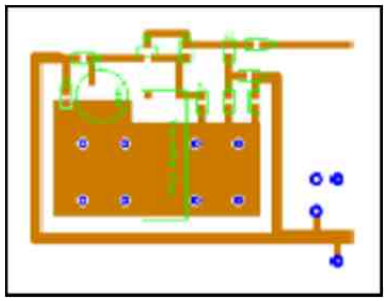

Figure 75. Colpitts oscillator PCB layout.

The next step in the design process involved replacement of the SAW device with a fixed capacitor. The oscillator circuit was implemented and tested for stability, power consumption, and sensitivity to change in the capacitive elements of the LC tank circuit. The revised oscillator circuit with component values is shown in Figure 76. The oscillator provided stable oscillation, low power consumption, and the oscillation frequency shifted

المنارة للاستشارات
www.manaraa.com

in accordance with the variable capacitor values changing from 1 to 30 pF. The oscillator output with the variable capacitor set at 14.8 pF is shown in Figure 77.

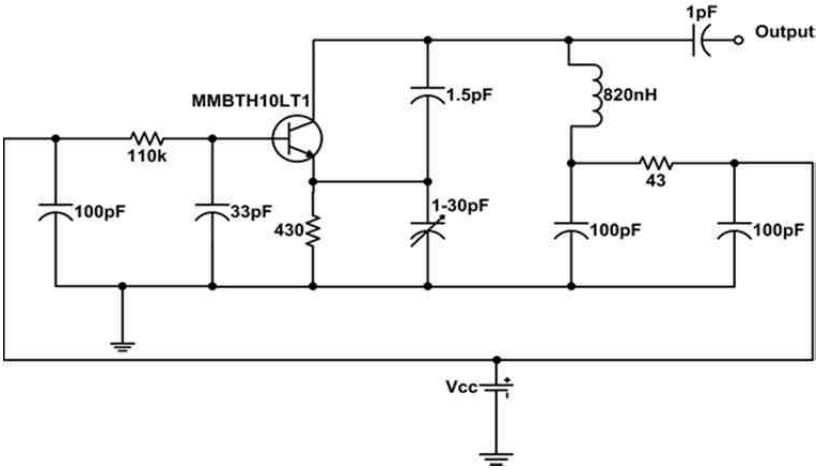

Figure 76. Revised discrete Colpitts oscillator circuit schematic.

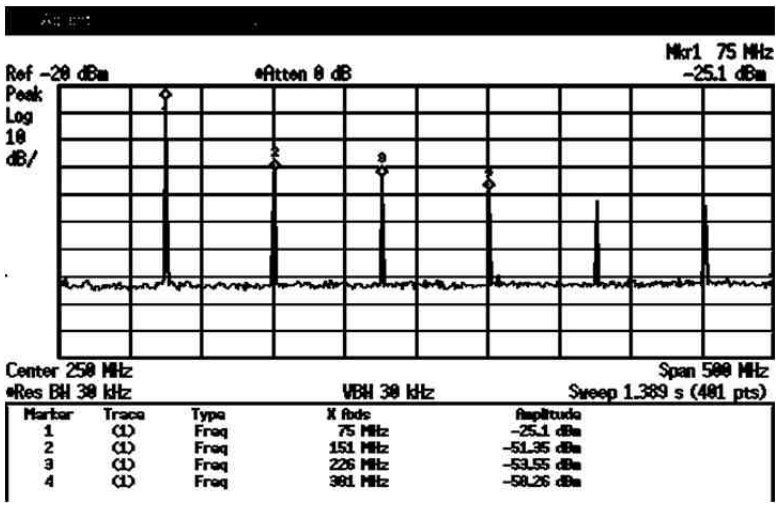

Figure 77. Discrete Colpitts oscillator output.

Initially, inductive coupling was considered to power the oscillator. To allow for inductive coupling of power and data and to reduce the oscillating frequency, the 820 nH inductor was replaced with various inductive coils. The coils were manufactured using

المنارة للاستشارات
www.manaraa.com

50 AWG wire and turns of 50, 100, 200 and 400. The magnitude and phase response of each coil was measured with a HP 4139A Vector impedance meter and the quality factor (Q) and inductance of each coil was calculated. The Q was calculated using

$$Q = \frac{|X|}{R} = tan(\theta) \tag{6.3}$$

where θ is the phase angle. The inductance of the coil was calculated using

$$L = \frac{X}{\omega} = \frac{(|Z| \sin\theta)}{2\pi f} \tag{6.4}$$

where Z is the magnitude of the impedance and f is the frequency of operation. The Q of the different coils versus frequency is shown in Figure 78.

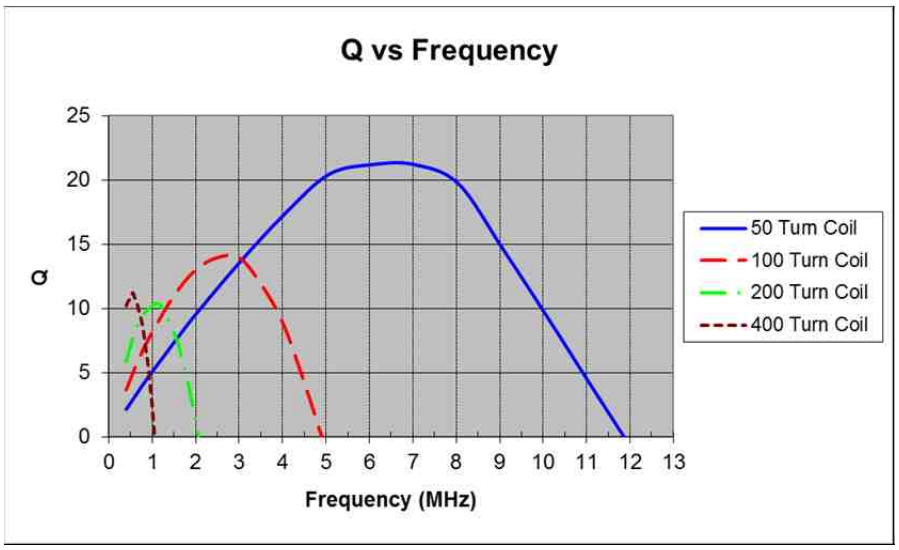

Figure 78. Quality factor of the different coils.

The 50 turn coil had the highest Q over the largest bandwidth. The coil was characterized using a vector impedance meter and the magnitude and phase response of the coil is shown in Figure 79. At the self resonant frequency (SRF) of an inductor, the

المنارة للاستشارات
www.manaraa.com

magnitude of the impedance is a maximum and the phase angle is zero. The SRF for the 50-turn coil is approximately 11.95 MHz as shown in Figure 79. With the 50 turn coil used as the inductance of the LC tank, the circuit oscillated at a frequency of 6.15 MHz with a supply voltage of 1V and supply current of 0.32 mA.

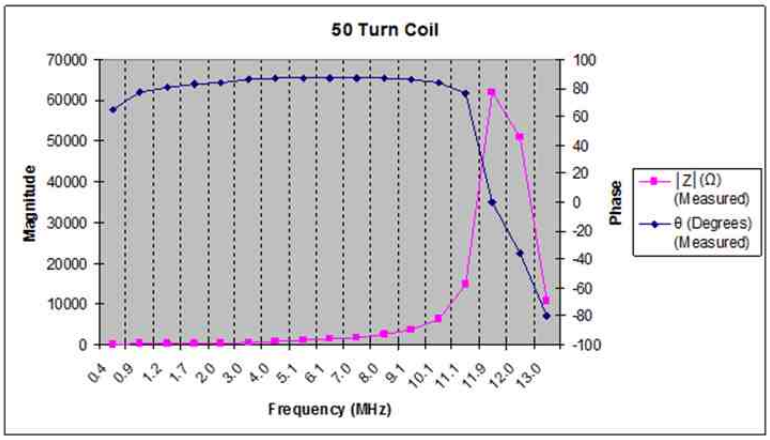

Figure 79. Magnitude and phase response of 50-turn coil.

The next step in the design process was to change the discrete oscillator circuit to an integrated circuit. The process was started by performing circuit simulations using PSpice from Cadence. The circuit was modified to include an integrated NMOS transistor that was fabricated and tested. Such a transistor was available through the UofL Wireless and Integrated Circuit Design Lab's library of standard MOSFET cells. An NMOS transistor from the T46B MOSIS run was used. The transistor was fabricated using the 1.5µm process from On Semiconductor. Transistors with different channel widths were used in the circuit and the circuit was analyzed and simulated to ensure that the loop gain and phase met the conditions for oscillation. The modified circuit is shown in Figure 80.

المنارة للاستشارات
www.manaraa.com

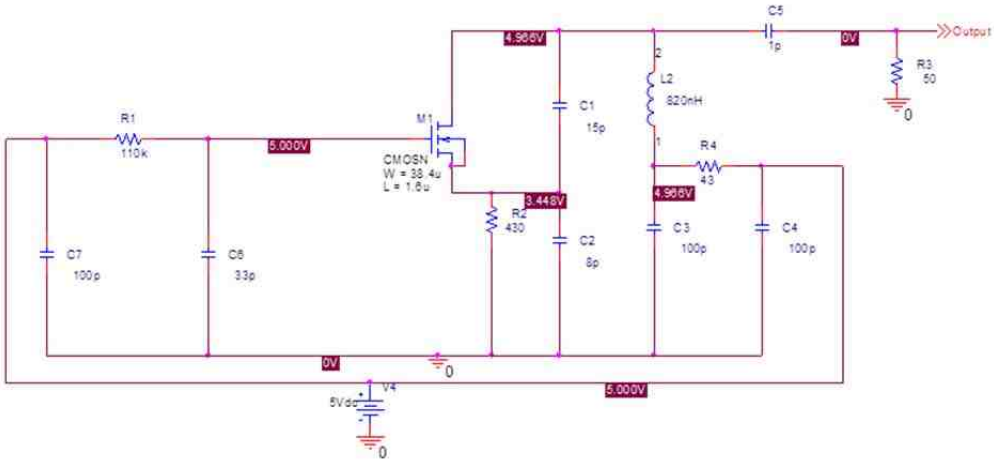

Figure 80. Colpitts circuit schematic with NMOS transistor.

In the loopgain and phase analysis, the circuit was broken at the node between the source of the transistor and resistor R2. The supply voltage was removed and a test signal was injected into the circuit at this point. The magnitude and phase response of the circuit was measured. Capacitor C2 was varied between 1 and 20 pF in the loop gain analysis and the results are shown in Figure 81. The graphs show that both conditions for oscillation, which are a loop gain greater than 1 (0 dB) and a phase shift of 180 degrees, are met for all values of C2.

المنارة للاستشارات
www.manaraa.com

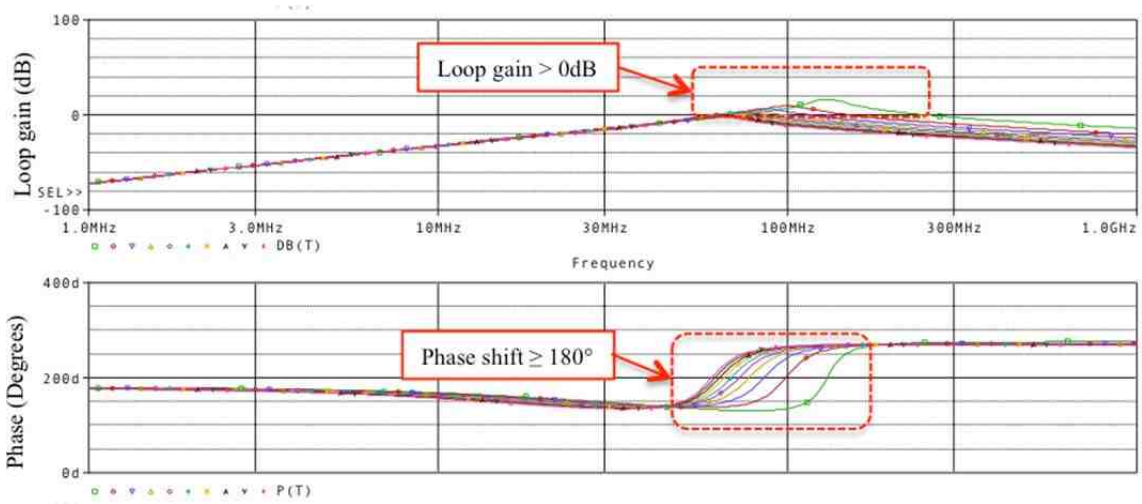

Figure 81. Loop gain(top) and phase(bottom) response of oscillator.

The circuit was simulated in PSpice but it was not possible to get the oscillations to start. Several methods to obtain an oscillator output were tried. These included injecting a small noise signal at the gate of the transistor and ramping up the supply voltage to simulate the switching of the power supply. Neither of these methods produced a consistent oscillator output, confirming that the Barkhausen criteria are not sufficient for steady state oscillations.

After several iterations some of the component values were changed to see if the circuit would produce an output. The resistor connected between source and ground was changed from 430 Ω to 4300 Ω. This change increased the source voltage and decreased the drain current. The resistance change resulted in the circuit producing an output without the need of a noise source or ramping up of the power supply. The oscillator output is shown in Figure 82.

المنارة للاستشارات
www.manaraa.com

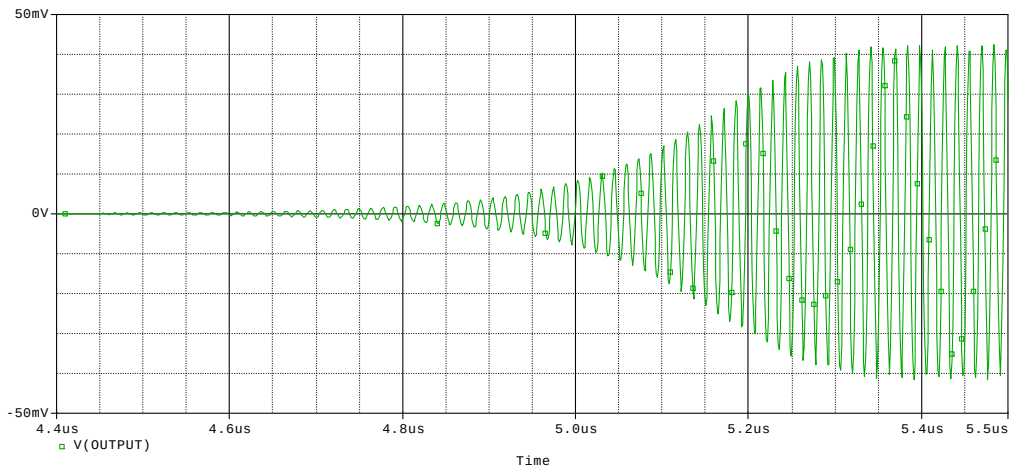

Figure 82. Simulated oscillator output.

The circuit still had too many large capacitors for IC fabrication. A 100 pF capacitor occupies approximately 14% of the available space on a 1.5 by 1.5 mm IC die. The original circuit contained three 100 pF capacitors that will occupy at least 42% of the available space. Some of the larger capacitors were removed without affecting the circuit from operating as an oscillator. The final circuit used for layout purposes is shown in Figure 83.

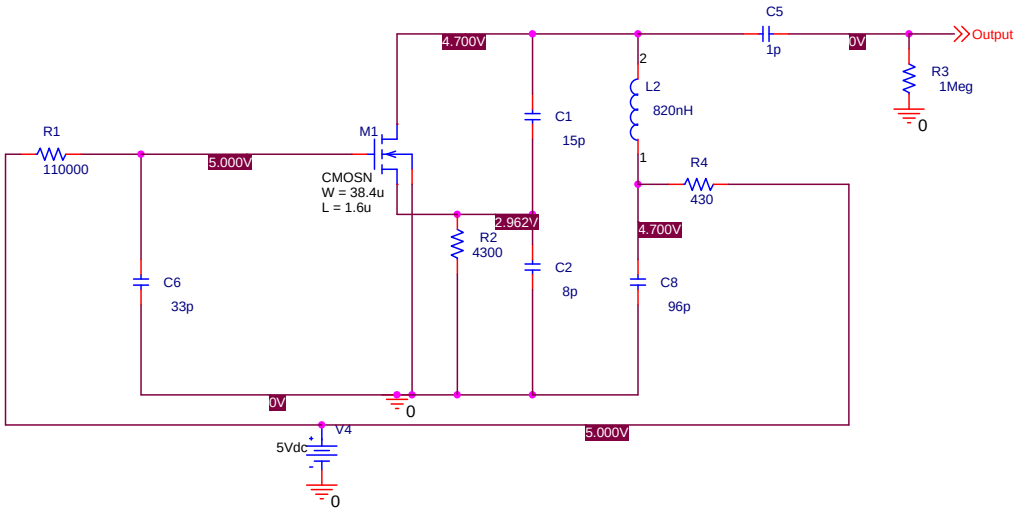

Figure 83. Colpitts oscillator circuit used for IC layout.

المنارة للاستشارات
www.manaraa.com

6.2.4 Spiral Inductor Characterization

An inductor forms part of the LC tank of the oscillator; since no spiral inductor was available as part of the L-Edit standard cell library, the viability of including a spiral inductor on the chip was investigated. A spiral inductor was laid out by Doug Jackson of the UofL Wireless and IC Design Laboratory and was fabricated using the AMI 0.5 µm CMOS C5 process. The inductor was evaluated and characterized. The die was inserted in a 16-pin DIP package and the two bond pads connected to the inductor were bonded to pins 4 and 5 of the DIP package. The bond pads used are shown circled in Figure 84.

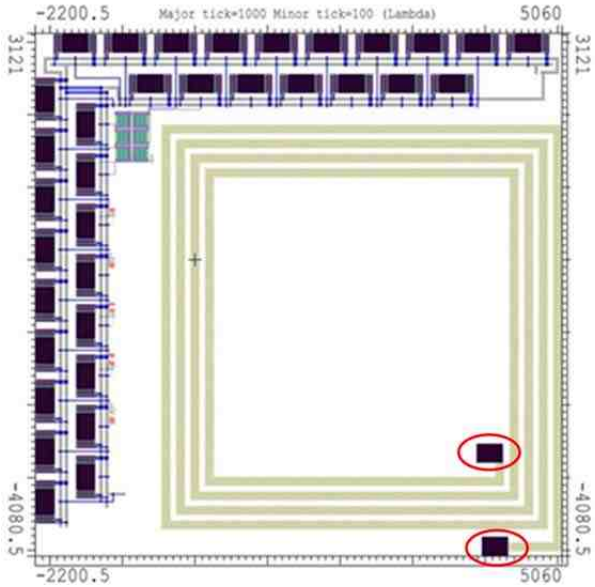

Figure 84. IC Die with spiral inductor.

Calibration of the network analyzer was necessary to make accurate measurements. A 50 Ohm resistor was connected between unused pins 1 and 2 of the IC package and a short circuit was connected between unused pins 6 and 7 for calibration purposes. The test equipment was therefore calibrated up to the pins on the DIP package. An Agilent 8714ES network analyzer was calibrated using these connections and the single port S-parameters of the inductor were measured over a frequency range from 300

المنارة للاستشارات
www.manaraa.com

kHz to 3 Ghz. The results are shown in Figure 85(a). The results were also plot on a Smith chart over the frequency range from 300 kHz to 1 GHz (Figure 85(b)).

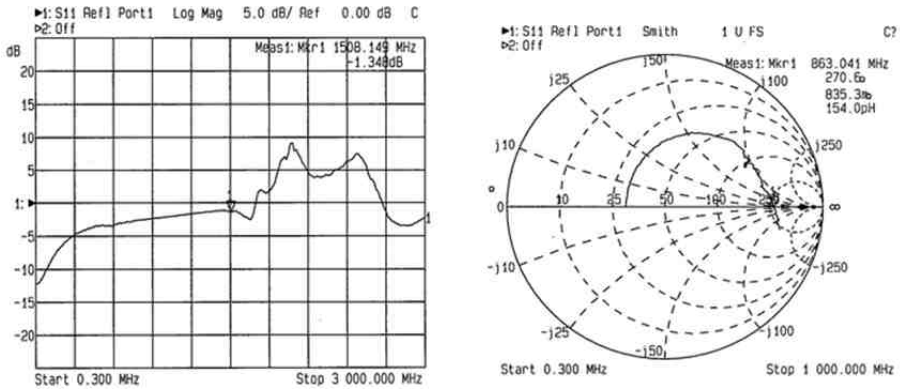

Figure 85. (a) Inductor S11 (b) Impedance.

The inductor was also tested using an Aligent 4294A Precision Impedance Analyzer with an impedance probe and BNC fixture. The frequency was swept from 40 Hz to 110 MHz and the equivalent circuit was measured. The equivalent circuit and component values are shown in Figure 86.

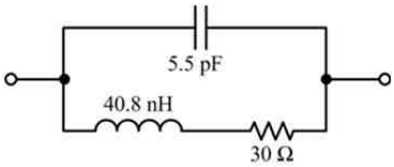

Figure 86. Inductor equivalent circuit.

The inductance of the spiral inductor was calculated using the Stanford Microwave Integrated Circuits Laboratory's online Integrated Spiral Inductor Calculator [65]. The calculated inductance was 48 nH, which is 17.6% higher than the measured value of 40.8 nH. The inductor was simulated using Advanced Design System (ADS) from Agilent Technologies. The layout was performed on a silicon substrate with metal parameters obtained from the AMI Semiconductor C5X, 0.5 Micron Technology Design Rules. The structure was drawn using Metal 3 with a thickness of 0.77 μm and a

المنارة للاستشارات
www.manaraa.com

conductivity of 32.47 x 10^6 Siemens/m. Bondpads were drawn by defining a metal layer with a thickness of 1.98 μm (the combined thickness of Metal 1, Metal 2 and Metal 3) and a conductivity of 23.83 x 10^6 Siemens/m (the average conductivity of Metal 1, Metal 2 and Metal 3). The layout is shown in Figure 87.

Figure 87. Inductor Layout in ADS.

The simulation was performed using Momentum in ADS. This is a Method of Moments analysis package that is primarily suited for doing fast simulations on 3D-planar designs. The same layout was used to perform simulations using the Finite Element Method (FEM) analysis package in ADS. The effective inductance, resistance, and the quality factor were calculated using the results of s-parameter simulations and the results are shown in Figure 88.

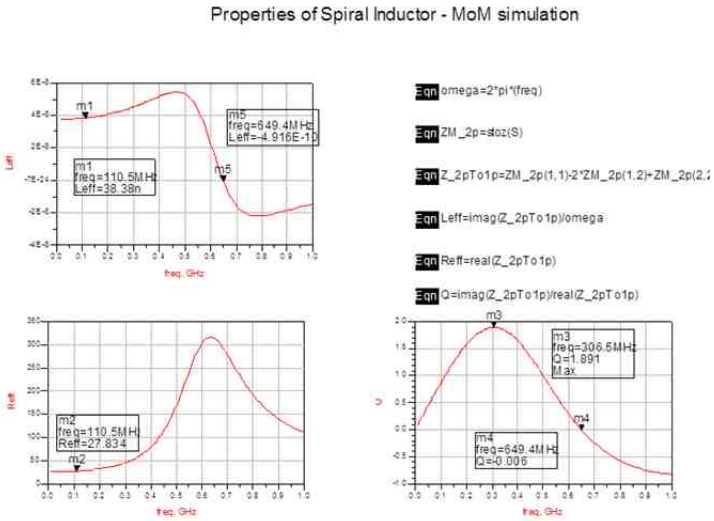

Figure 88. ADS Inductor simulation results.

المنارة للاستشارات
www.manaraa.com

The self-resonant frequency (SRF) was obtained from the results contained in Figure 38. At the SRF of an inductor, the effective inductance and the Q of the inductor are zero. The SRF for this inductor is approximately 650 MHz (Marker 5 in Figure 88). The results of the two analysis methods were compared with the measured data at 110 MHz and are summarized in Table 12. The results obtained using the MoM analysis corresponds better to the measured values than the FEM method.

Table 12. Spiral inductor characteristics.

Property	Measured	MoM	FEM
Effective inductance	40.8 nH	38.4 nH	32.7 nH
Effective resistance	30 Ω	27.8 Ω	2.9 Ω
Quality factor		1.9	8.3
Self Resonant Frequency		650 MHz	593 MHz

6.2.5 Discrete Oscillator

A discrete Colpitts oscillator was implemented on a FR-4 PCB. This circuit was used to determine the maximum oscillation frequency that could be obtained with a discrete design and to evaluate the accuracy of simulations that were performed in Advanced Design System from Agilent. Simulations were performed using ideal components, surface mount components (SMT) with ideal connections, and SMT components with transmission line connections. The circuit schematics, output signals, and spectra for the different simulations are shown in Figures 89 to 91.

المنارة للاستشارات
www.manaraa.com

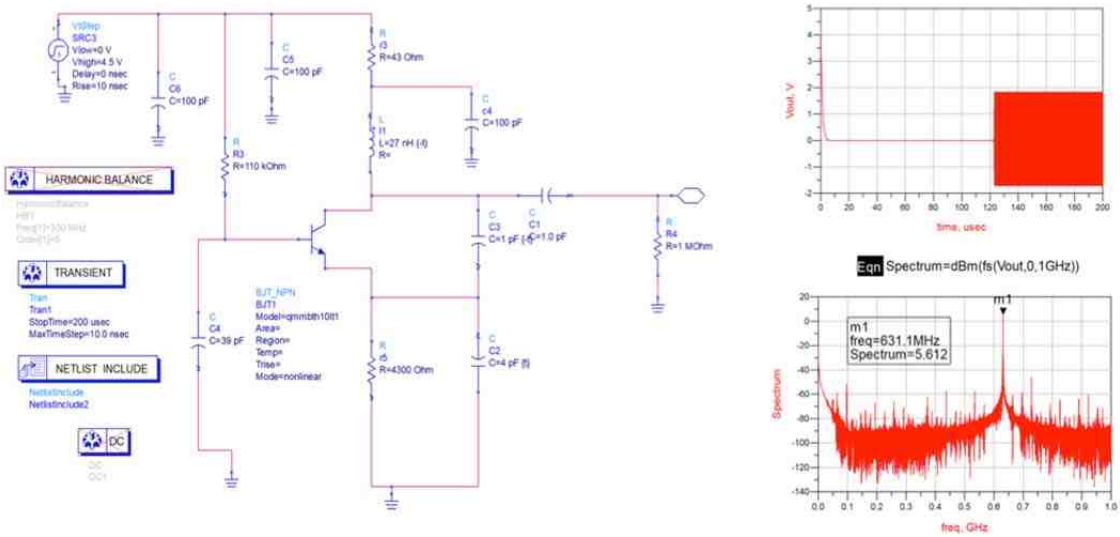

Figure 89. Discrete Colpitts oscillator schematic and output signal with spectrum.

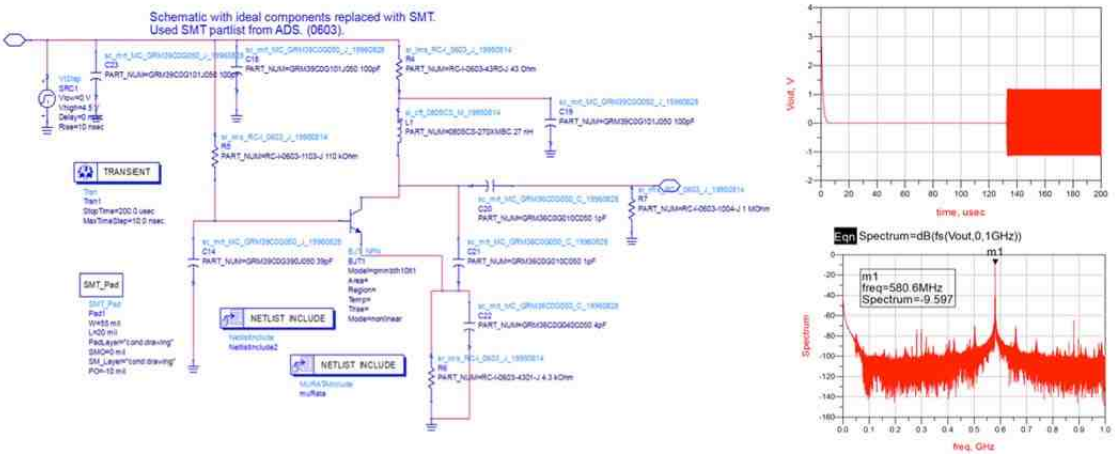

Figure 90. Discrete Colpitts oscillator schematic with SMT components, output and spectrum.

المنارة للاستشارات
www.manaraa.com

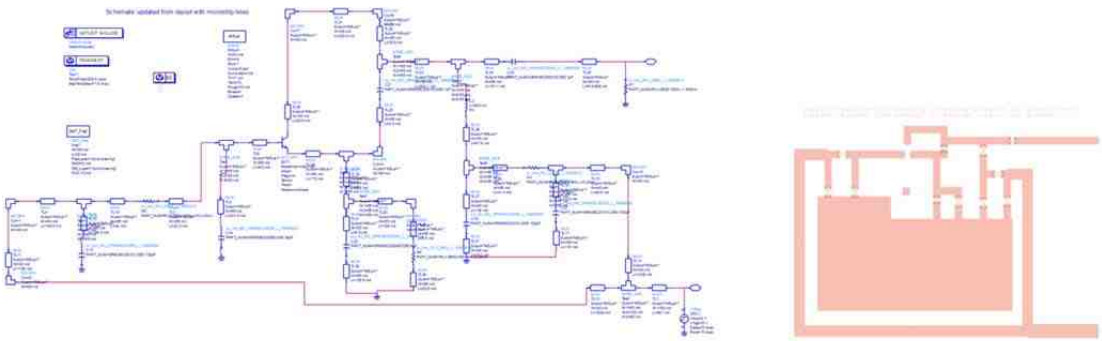

Figure 91. Discrete Colpitts oscillator schematic with SMT components and transmission lines, PCB layout at right.

No simulated output could be generated using the circuit with SMT components transmission line connections. The circuit was fabricated on a PCB and tested in the laboratory. The output of the oscillator was measured using a high impedance probe connected to a spectrum analyzer. A comparison between the simulated and measured parameters of the oscillator is shown in Table 13. A supply voltage of 4.5 V was used in the measurements to enable comparison with the simulated results; however, the oscillator can operate with a supply voltage as low as 1.8 V and consumes only 266 µA with a 2 V supply voltage.

Table 13. Comparison of simulated and measured oscillator parameters.

Parameter	Measured	Simulated		
		Ideal components	SMT components, ideal connections	SMT components, T-line connections
Osc freq	400 MHz Vcc = 4.5 V	631 MHz Vcc = 4.5 V	580 MHz Vcc = 4.5 V	None
Output power	-17 dBm	5.6 dBm	0.403 dBm	None
Vce	1.21 V	1.29 V	1.29 V	1.29 V
Ic	754 µA	311 µA	311 µA	311 µA
Vc	4.47 V	2.65 V	2.65 V	2.65 V
Vb	3.87 V	2.06 V	2.06 V	2.06 V
Ve	3.27 V	1.36 V	1.36 V	1.36 V
Vbe	0.6 V	0.7 V	0.7 V	0.7 V
Comments	Oscillations start at Vcc = 1.8 V	Needs Vcc = 4.5 V for oscillations to start		

المنارة للاستشارات
www.manaraa.com

6.3 Energy Harvesting Circuit Design

A variety of different RF rectification topologies were investigated. These included the Greinacher and Dickson topologies as discussed in Chapter 3 as well as three other that were considered for implementation, but were eventually excluded due to the complexity of the designs and the risks involved. The three that were excluded are discussed briefly.

A sixteen-stage voltage multiplier was developed by Kocer et al. [21]. Kocer et al. referred to it as a Cockcroft-Walton multiplier, which is also called the Greinacher; however, the topology resembles the Dickson configuration. Kocer et al. claim an output voltage of 2.5 V DC with an input signal of only 140 mV. The efficiency was defined as

$$\eta = \frac{V_{out}}{V_{in-peak} \times n} \tag{6.5}$$

where n is the number of stages. An efficiency of 78% was observed. The circuit schematic is shown in Figure 92.

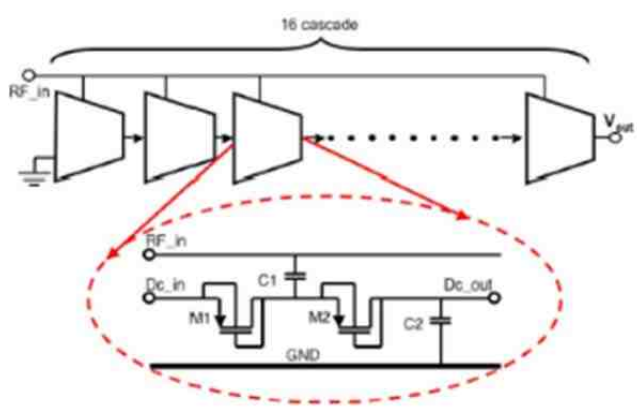

Figure 92. Kocer et al. sixteen stage voltage multiplier.

A three-stage CMOS rectifier was implemented by Mandal and Sarpeshkar [48] in the AMI 0.5 µm process as shown in Figure 93. The rectifier efficiency was defined as

المنارة للاستشارات
www.manaraa.com

$$\eta = \frac{P_{load}}{P_{incident}}. \tag{6.6}$$

With a nominal load of 2 μW, and a power-up threshold of 62 μW, the efficiency was 3.2%, which corresponds to a theoretical free space range of 8 m (900 MHz, 36 dBm EIRP).

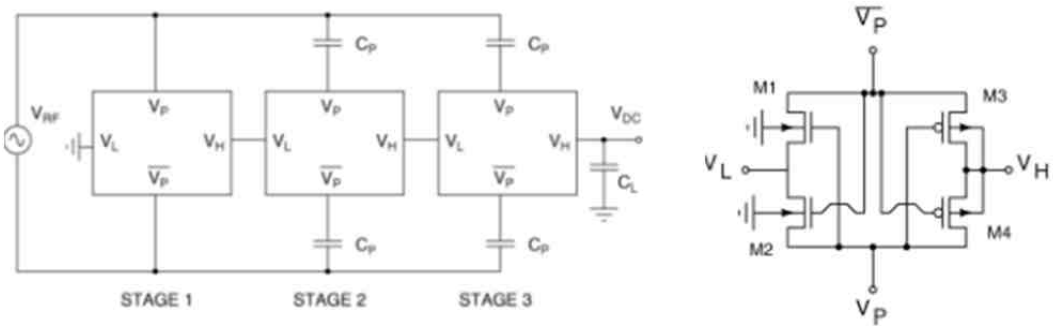

Figure 93. Three-stage CMOS rectifier schematic.

Nakamoto et al. [66] implemented a single-stage full-wave CMOS rectifier with a circuit configuration as shown in Figure 94. They implemented the circuit using a 0.35 μm process. An efficiency of 36.6% at a frequency of 953 MHz and a range of 4 m was reported.

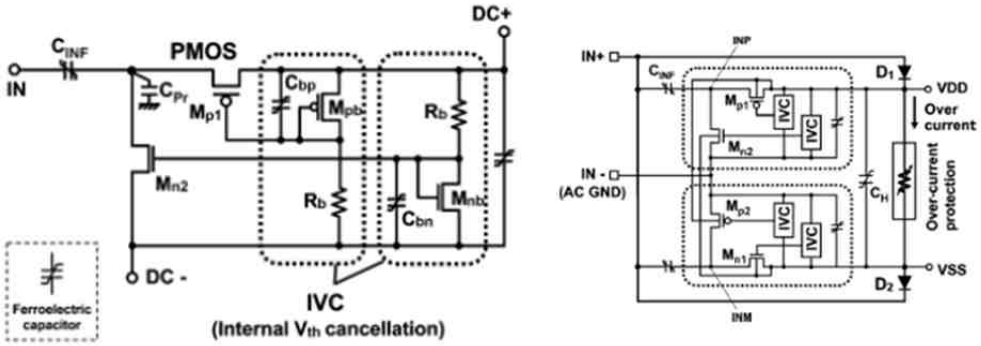

Figure 94. Single-stage full-wave CMOS rectifier.

The Greinacher and Dickson rectifier topologies are simpler and easier to implement than the configurations discussed above; therefore, a variety of Greinacher and Dickson topologies were designed and implemented. The Greinacher and Dickson

المنارة للاستشارات
www.manaraa.com

topologies have been implemented by others using low-voltage Schottky diodes or diode connected MOSFET transistors. Several test pieces were designed, simulated using T-Spice from Tanner Tools, and laid out for fabrication using L-Edit from Tanner Tools. The circuits were included on an ASIC that also contained several other test pieces that formed part of the system design. The ASIC was submitted to MOSIS at the end of November 2010, but due to problems in the fabrication process at the foundry, the ASIC was only received for testing at the end of June 2011. The design process for the RF rectifier circuit involved the design, fabrication and testing of a total of four ASICs and is discussed in more detail in the following sections.

6.3.1 ASIC 1: Schottky and MOSFET rectifier/multiplier implementation

6.3.1.1 Design and Simulation

Several rectifier designs were included as test pieces on the first ASIC. Multi-stage rectifier/multiplier designs of both Greinacher and Dickson topologies were implemented using Schottky diodes and diode connected NMOS transistors and capacitors. The number of stages was initially limited to four since increasing the number of stages can lead to lower output voltages due the current drain of later stages [7]. Both of the topologies and implementations have successfully been used by others but they all made use of specialized processes and technologies that offered lower voltage operation [16, 17, 23]. The possibility of implementing these designs using a mature, inexpensive process such as the 0.5µm CMOS fabrication process from On Semiconductor through MOSIS was investigated for this application. Capacitors of 1 pF were used in all the designs. This capacitance value was chosen since it provides a low impedance path of

المنارة للاستشارات
www.manaraa.com

174 Ω at 915 MHz and occupies a relatively small space on the IC. A Schottky diode that is part of the standard cell library of the UofL Wireless and IC Design Laboratory was used in the diode implementation. The diode was characterized by Matt Turner [67] and the SPICE model parameters were extracted using MATLAB. These parameters were used in the simulations that were performed using T-Spice from Tanner Tools. The circuit schematics and simulation results for the different topologies are shown in Figures 95 to 101. Figure 95 shows the circuit schematic and simulation results of a two-stage Greinacher half-wave rectifier/multiplier that was implemented using Schottky diodes. The simulated input signal is a 250 mV peak sinusoid at a frequency of 915 MHz and a DC output voltage of 700 mV is produced.

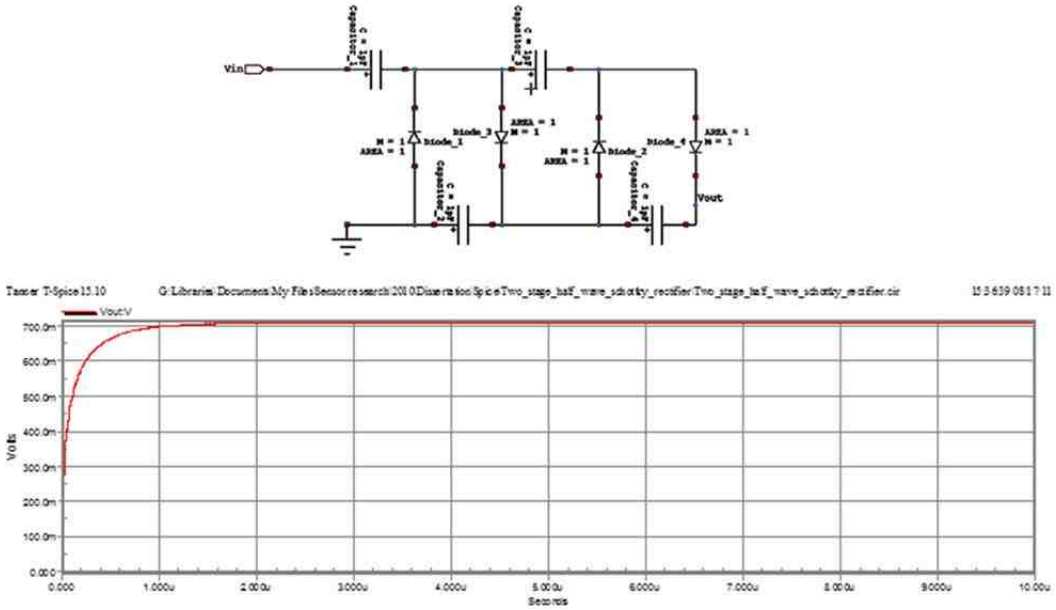

Figure 95. Two-stage Greinacher Schottky half-wave multiplier boosting voltage to 700mV.

Figure 96 shows the circuit schematic and simulation results of a two-stage Greinacher half-wave rectifier/multiplier. The circuit was implemented using diode

www.manaraa.com

connected MOSFET transistors. In this case an input sinusoidal signal of at least 750 mV peak was needed before rectification was observed and only 550 mV DC was produced.

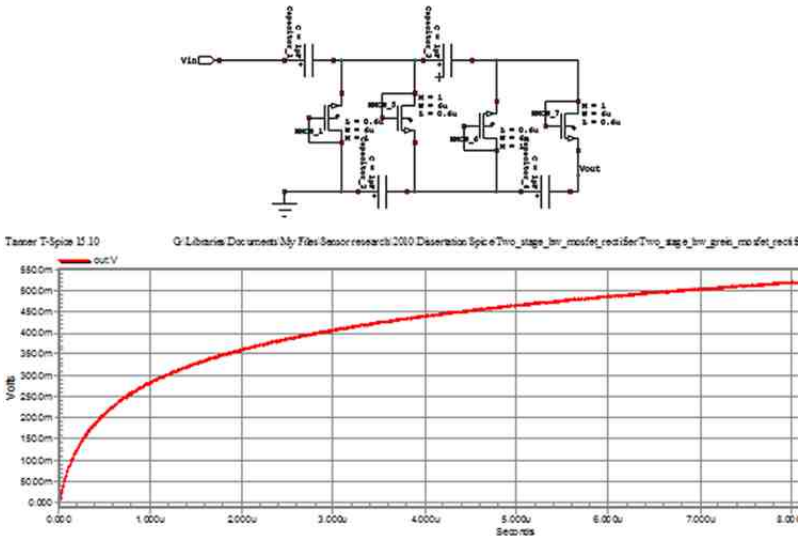

Figure 96. Two-stage Greinacher MOSFET half-wave multiplier with decreased performance.

The circuit schematic and simulation results of a four-stage Greinacher half-wave rectifier/multiplier. The circuit was implemented using Schottky diodes as shown in Figure 97. This rectifier/multiplier was able to produce 1.4 V DC with a 250 mV sinusoidal input signal at 915 MHz.

المنارة للاستشارات
www.manaraa.com

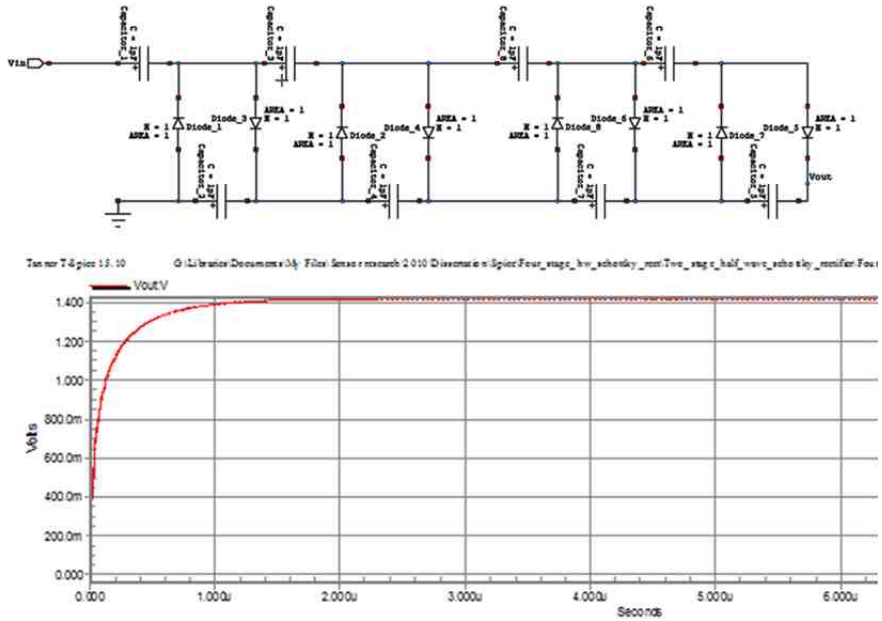

Figure 97. Four-stage Greinacher half-wave multiplier boosting signal to 1.4V.

Figure 98 shows the circuit schematic and simulation results of a two-stage Dickson half-wave rectifier/multiplier. The circuit was implemented using Schottky diodes. A 250 mV sinusoidal input signal at a frequency of 915 MHz produced a 700 mV DC output.

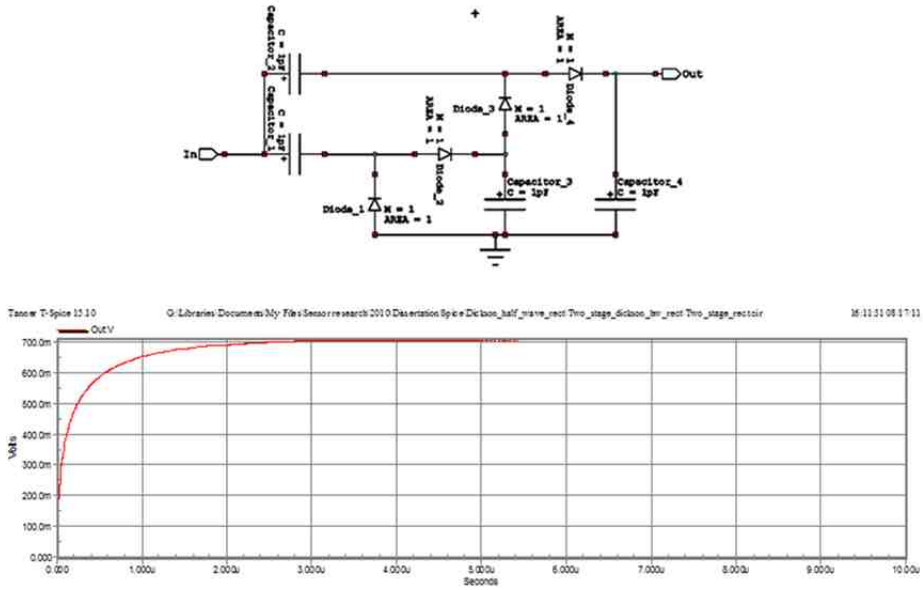

Figure 98. Two-stage Dickson half-wave multiplier using Schottky diodes.

المنارة للاستشارات
www.manaraa.com

The circuit schematic and simulation results of a two-stage Dickson half-wave rectifier/multiplier. The circuit was implemented using diode coupled MOSFET transistors as shown in Figure 99. The simulated output was only 500 mV DC with a 750 mV sinusoidal input signal at 915 MHz.

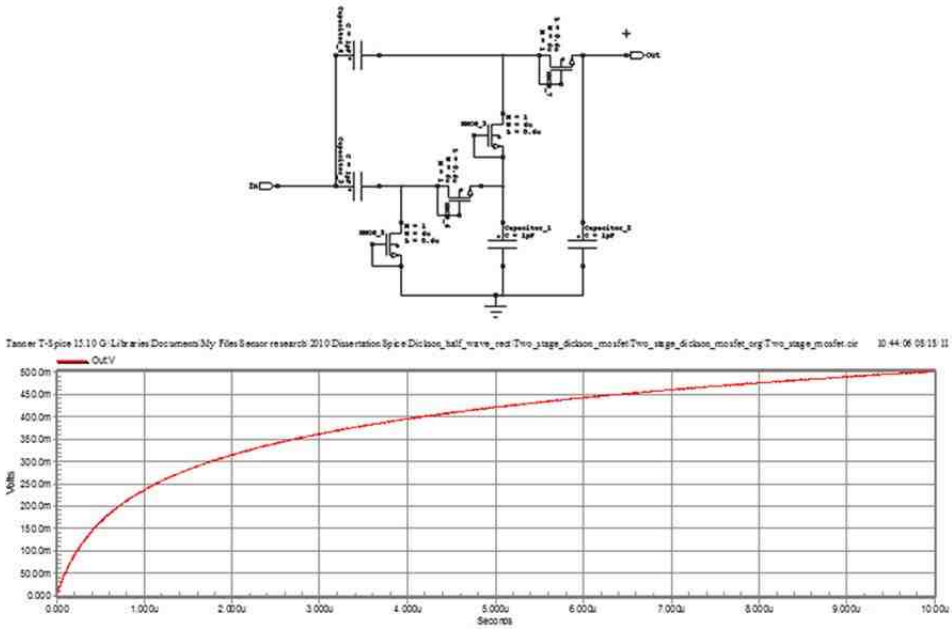

Figure 99. Two-stage Dickson half-wave multiplier using MOSFETs.

Two full-wave Dickson rectifiers/multipliers were included as test pieces. Curty et al. [23, 24] implemented this configuration using Silicon-on-Sapphire (SOS) 0.5 µm CMOS technology. Figures 100 and 101 show the circuit schematic and simulation results for full-wave Dickson rectifiers/multipliers that were implemented using Schottky diodes and diode connected MOSFET's, respectively. The simulated output for the Schottky implementation was 700 mV DC with a 250 mV sinusoidal input signal at 915 MHz. This was the same as the simulated output of the two-stage Dickson rectifier/multiplier. The simulated DC output for the MOSFET implementation was only 500 mV for a 750 mV input signal and was also identical to the half-wave implementation. The circuits were

المنارة للاستشارات
www.manaraa.com

laid out using L-Edit from Tanner Tools. The ASIC circuit layout and pin layouts are shown in Figures 102 and 103.

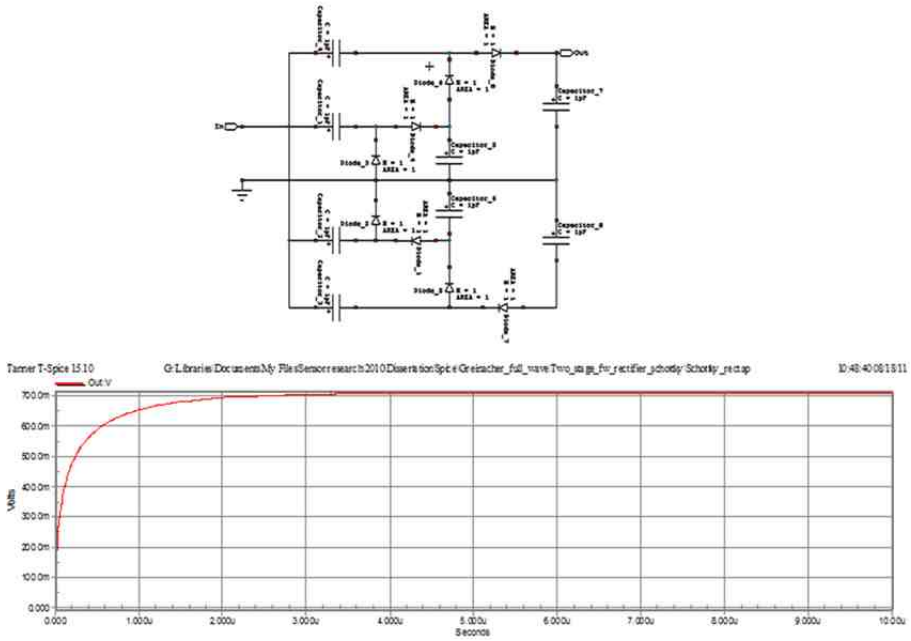

Figure 100. Two-stage Dickson full-wave Schottky multiplier.

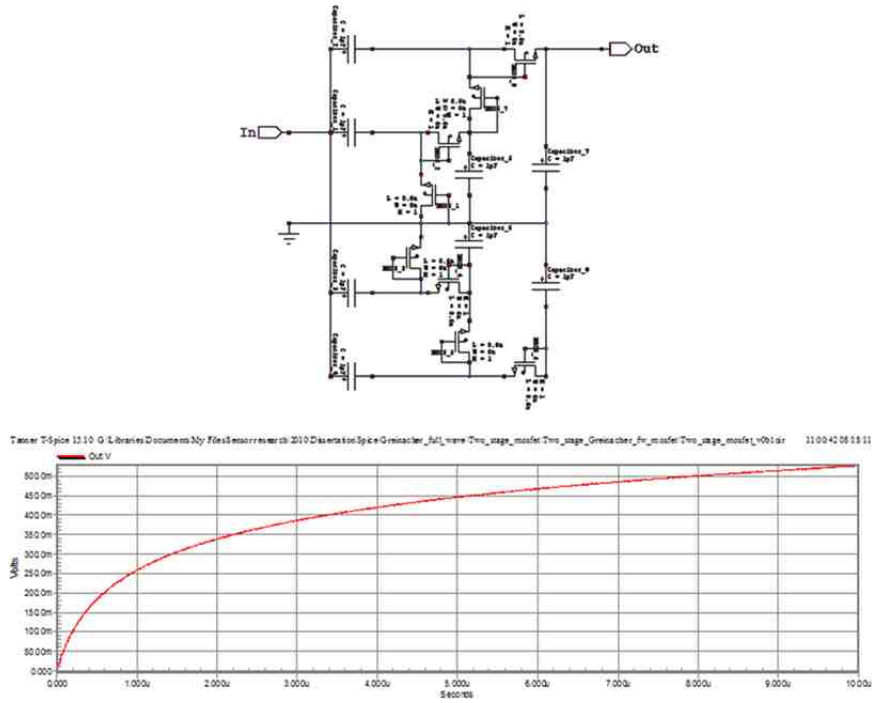

Figure 101. Two-stage Dickson full-wave MOSFET multiplier.

المنارة للاستشارات
www.manaraa.com

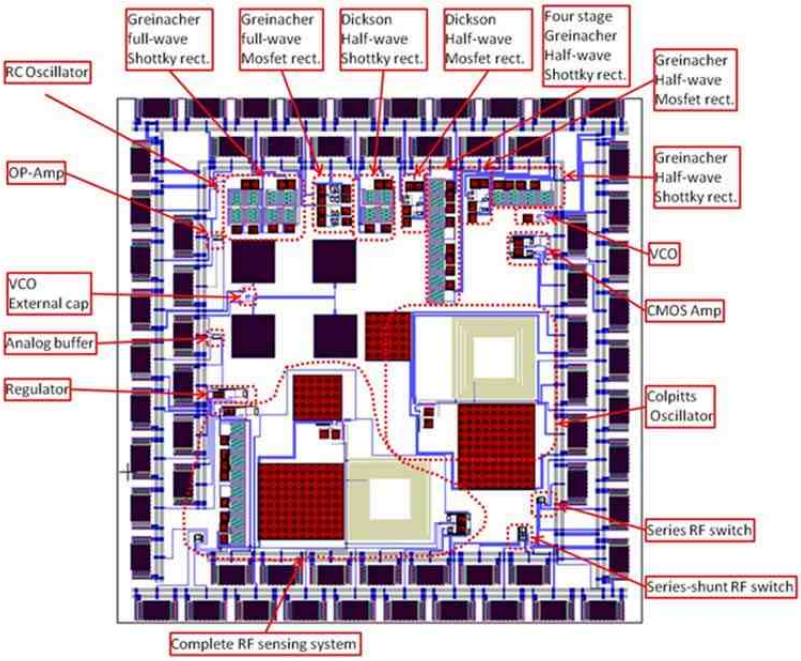

Figure 102. ASIC test circuit layout.

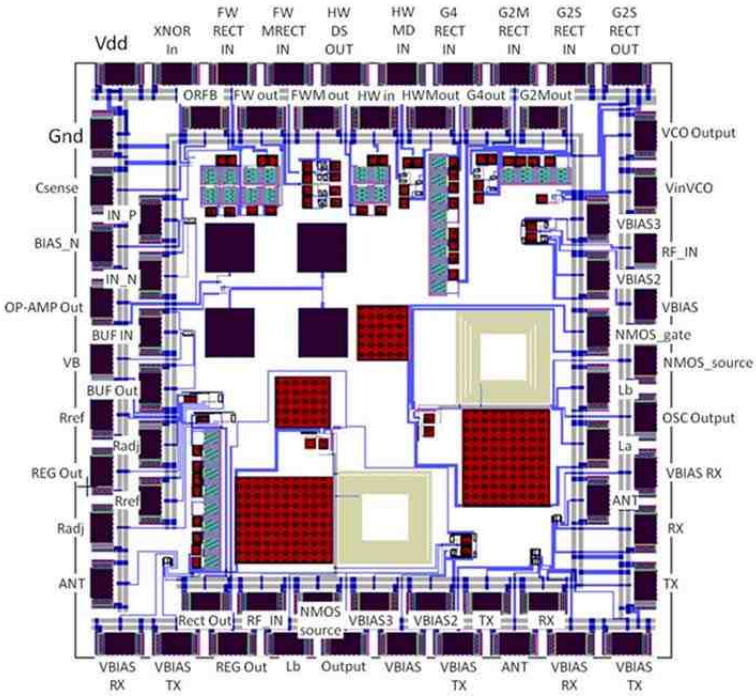

Figure 103. ASIC pin layout.

المنارة للاستشارات
www.manaraa.com

6.3.1.2 Measurement results

Two types of tests were performed on the rectifier circuits, direct RF-to-DC conversion and radiated RF-to-DC conversion. The ASICs were packaged in a Pin Grid Array (PGA121) ceramic package. Measurement instruments were connected to the relevant pins on the package. The results of these tests are discussed here.

6.3.1.2.1 Direct RF-to-DC conversion

The input of the test piece was connected to the output of an Agilent 8648C signal generator. A 1 V peak, 915 MHz signal was generated using the signal generator. The output of each test piece was measured using a Fluke 87V digital multimeter and an Agilent 54645D oscilloscope. The test results are summarized in Table 14.

Table 14. Direct RF-to-DC conversion test results.

Test piece	**Circuit**	**DC output voltage**	
		Oscilloscope	Voltmeter
1	Two –stage Greinacher Schottky half wave rectifier	0.64	0.72
2	Two-stage Greinacher Mosfet half wave rectifier	-0.3	-0.3
3	Four stage Greinacher Schottky half wave rectifier	0.4	0.6
4	Two-stage Dickson Schottky half wave rectifier	1	1
5	Two-stage Dickson Mosfet half wave rectifier	0.3	0.5
6	Two-stage Dickson Schottky full wave rectifier	0.7	0.8
7	Two-stage Dickson Mosfet full wave rectifier	0.2	0.2

The Schottky rectifiers produced DC voltages that were more than twice the DC voltages produced by the MOSFET rectifiers. The Dickson half-wave Schottky rectifier produced the highest DC output voltage of 1 V.

المنارة للاستشارات
www.manaraa.com

6.3.1.2.2 Radiated RF-to-DC conversion

A 915 MHz dipole antenna was connected to the input of each test piece. A 915 MHz, -10 dBm sinusoidal signal was generated using an Agilent 8648C signal generator. This signal was amplified using a Min-Circuits ZHL-4240 amplifier and transmitted using a 915 MHz dipole connected to the output of the amplifier. The antennas were set up over a test bench and separated by 0.5m for the first test and 1m for the second test. The DC output of each test piece was measured using a Fluke 87V digital multimeter. The transmitting signal frequency was also adjusted to obtain a maximum output voltage. The results are summarized in Table 15.

Table 15. Radiated RF-to-DC conversion test results.

Test piece	**Circuit**	**DC output voltage – 0.5 m**	**DC output voltage – 1 m**
1	Two –stage Greinacher Schottky half wave rectifier	0.13 at 915 MHz 0.24 at 905 MHz	0.03 at 915 MHz 0.07 at 905 MHz
2	Two-stage Greinacher Mosfet half wave rectifier	No output	No output
3	Four stage Greinacher Schottky half wave rectifier	0.014 at 915 MHz 0.03 at 905 MHz	0.03 at 915 MHz 0.075 at 905 MHz
4	Two-stage Dickson Schottky half wave rectifier	0.15 at 915 MHz 0.17 at 905 MHz	0.045 at 915 MHz 0.08 at 905 MHz
5	Two-stage Dickson Mosfet half wave rectifier	No output	No Output
6	Two-stage Greinacher Schottky full wave rectifier	0.03 at 915 MHz 0.1 at 905 MHz	0.09 at 915 MHz 0.15 at 905 MHz
7	Two-stage Greinacher Mosfet full wave rectifier	No Output	No output
	Connected 6 and 4 together	0.09at 915 MHz 0.12 at 905 MHz	0.09at 915 MHz 0.1 at 905 MHz

The MOSFET rectifiers produced no DC output voltage. The DC output voltages from the Schottky rectifiers were disappointingly small and the performance of the Greinacher and Dickson topologies were similar. The results indicated that no usable DC voltage could be generated by these circuits. Based on work by Chow et al. [6], who

المنارة للاستشارات
www.manaraa.com

successfully implemented the Greinacher topology, Greinacher rectifier circuits with a higher number of stages were implemented and tested.

6.3.2 ASIC 2 – Multi-stage Greinacher rectifier circuits.

Two eight stage and one sixteen stage Greinacher topology rectifier circuits were designed, simulated, and fabricated. The circuits were simulated using TSpice from Tanner Tools and the simulations verified using Advanced Design System (ADS) from Agilent Technologies. A 50 Ω impedance match was designed for one of the eight stage circuits. The matching circuit consisted of a 52 Ω resistor in parallel with a 0.31 pF capacitor. The impedance matching circuit was designed using the impedance matching utility in ADS. A screen shot of the utility is shown in Figure 104.

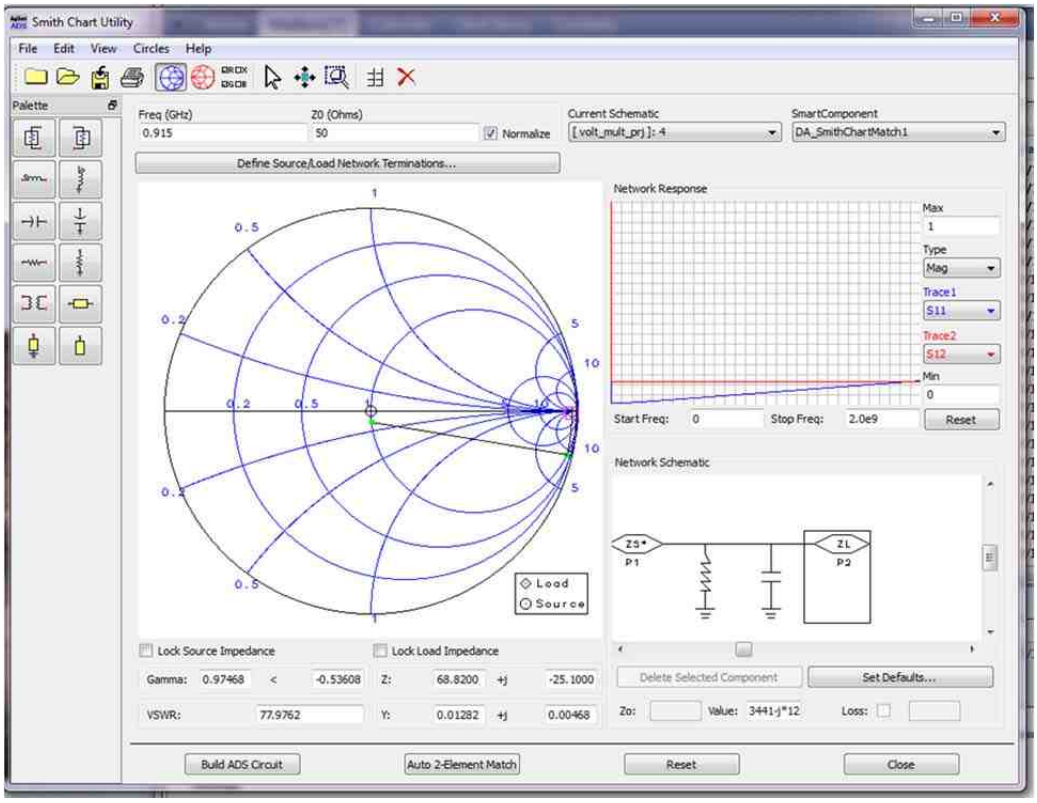

Figure 104. Worksheet screen shot of impedance matching utility.

المنارة للاستشارات
www.manaraa.com

The circuit schematic of a multi-stage Greinacher rectifier is shown in Figure 105. The circuits were fabricated using the 0.5 μm CMOS process from On Semiconductor through MOSIS. The layout is shown in Figure 106.

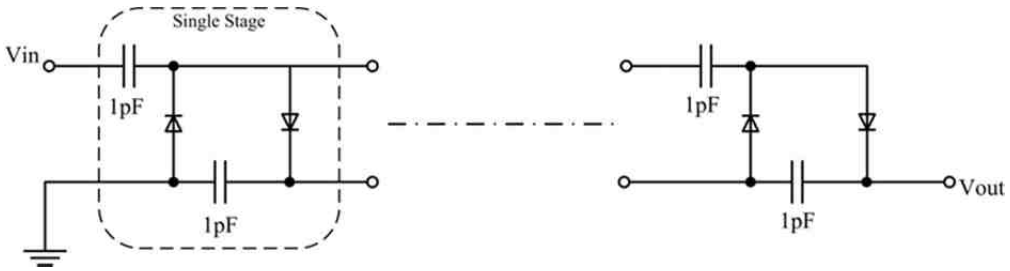

Figure 105. Multi-stage Greinacher rectifier circuit schematic.

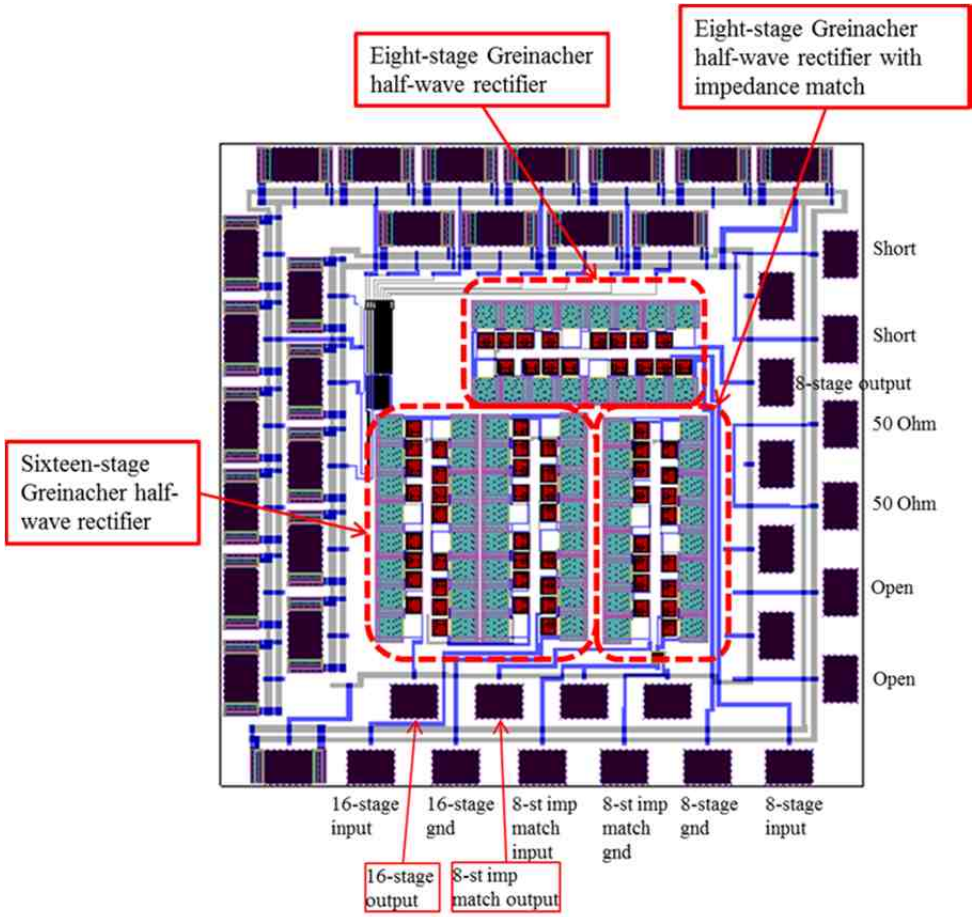

Figure 106. Multi-stage Greinacher rectifier circuit layout.

المنارة للاستشارات
www.manaraa.com

6.3.2.1 Direct RF-to-DC conversion measurement results

A 50 Ω test fixture was fabricated on a FR-4 printed circuit board and the IC die was fixed to the board using a silver epoxy. Connections between the bond-pads of the IC and the input, output, and ground of the test fixture were performed with a ball-bonder using gold bond-wires. The test fixture is shown in Figure 107.

Figure 107. Rectifier circuit 50Ω Test fixture.

The input of the test piece was connected to the output of a Mini-Circuits ZHL-4240 amplifier. The input of the amplifier was driven using a 915 MHz, 2 mV peak signal from an Agilent 8648C signal generator and the output DC voltage was measured using a Fluke 87V digital multimeter. The test setup is shown in Figure 108. The signal generator output voltage was increased in steps of 1 mV. The test results are summarized in Tables 16 to 18.

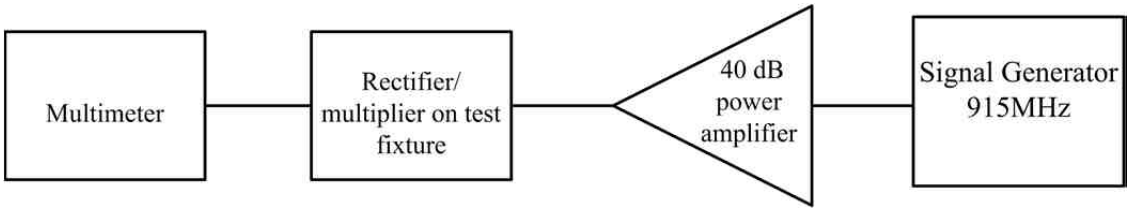

Figure 108. Test setup for measuring DC output voltage of rectifiers/multipliers.

المنارة للاستشارات
www.manaraa.com

Table 16. Eight-stage Greinacher half-wave rectifier test results.

Generator output (mV)	Rectifier input (mVpeak)	DC output
2	14	230 mV
3	21	650 mV
4	29	1.2 V
5	35	1.8 V
6	40	2.6 V
7	44	3.2 V
8	51	4.3 V
9	58	5 V
10	64	6 V
15	98	10 V

Table 17. Eight-stage Greinacher half-wave rectifier with impedance match test results.

Generator output (mV)	Rectifier input (mVpeak)	DC output
2	28	200 mV
3	35	400 mV
4	50	1 V
5	65	1.5 V
6	80	2 V
7	88	2.7 V
8	100	3 V
9	115	4.3 V
10	144	4.8 V
15	205	9 V

Table 18. Sixteen-stage Greinacher half-wave rectifier test results.

Generator output (mV)	Rectifier input (mVpeak)	DC output
2	40	160 mV
3	64	470 mV
4	80	830 mV
5	105	1.6 V
6	128	2.3 V
7	155	3.1 V
8	180	4.1 V
9	190	4.7 V
10	215	5.8 V
15	315	11.2 V

المنارة للاستشارات
www.manaraa.com

DC voltages in excess of 2 V were generated with an input voltage as low as 40mV. The results shown in tables 16 to 18 indicated that the Greinacher rectifier/multiplier configuration was able to supply sufficient DC voltage for a wireless application. It was not clear why the eight-stage rectifier with impedance matching performed worse than the eight-stage rectifier without impedance matching.

6.3.2.2 Radiated RF-to-DC conversion

A 915 MHz dipole antenna was connected to the input of the test piece. A 915 MHz, -7 dBm signal was generated from an Agilent 33250A waveform generator and used as input to a Mini-Circuits ZHL-4240 amplifier with 915 MHz dipole antenna connected to the output of the amplifier. The two antennas were separated by 0.5 m for the first test and 1m for the second test and the DC voltage at the output of the test piece was measured using a Fluke 87V digital multimeter. The results are summarized in Table 19.

Table 19. DC output voltage at distances of 0.5 m and 1 m.

Circuit	**DC output voltage – 0.5m**		**DC output voltage – 1m**	
	915 MHz	930 MHz	915 MHz	930 MHz
Eight –stage Greinacher Schottky half wave rectifier	0.7 V	1 V	0.17 V	0.4 V
Eight-stage Greinacher Mosfet half wave rectifier with impedance match	0.7 V	0.9 V	0.33 V	0.5 V
Sixteen stage Greinacher Schottky half wave rectifier	0.3 V	0.7 V	0.06 V	0.18 V

The DC voltages that were generated were too low to power other circuits. Several studies showed the successful use of the Greinacher topology; however, all used

المنارة للاستشارات
www.manaraa.com

a different fabrication technology. Further research indicated that better performance is achieved by using the Dickson rectifier circuit topology.

6.3.3 ASIC 3 – Multi-stage Dickson Rectifier Circuits

Several multi-stage rectifier circuits, using the Dickson topology, were designed, simulated, and fabricated. Simulations were performed using TSpice from Tanner Tools and ADS from Agilent Technologies. Half-wave and full-wave rectifier circuits were included. The basic two-stage, half-wave rectifier circuit configuration is shown in Figure 109. Multiple stages are created by adding more of this basic configuration in series. A two-stage, full-wave rectifier circuit configuration is shown in Figure 110. Higher order stages were created by adding additional stages in series. The circuits were fabricated using the 0.5 µm CMOS process from On Semiconductor through MOSIS. The IC pin layout and bonding diagram are shown in Figure 111 and Table 20.

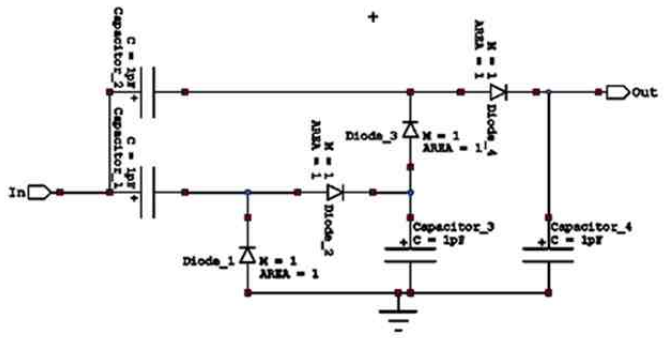

Figure 109. Two-stage, half-wave Dickson rectifier circuit schematic.

المنارة للاستشارات
www.manaraa.com

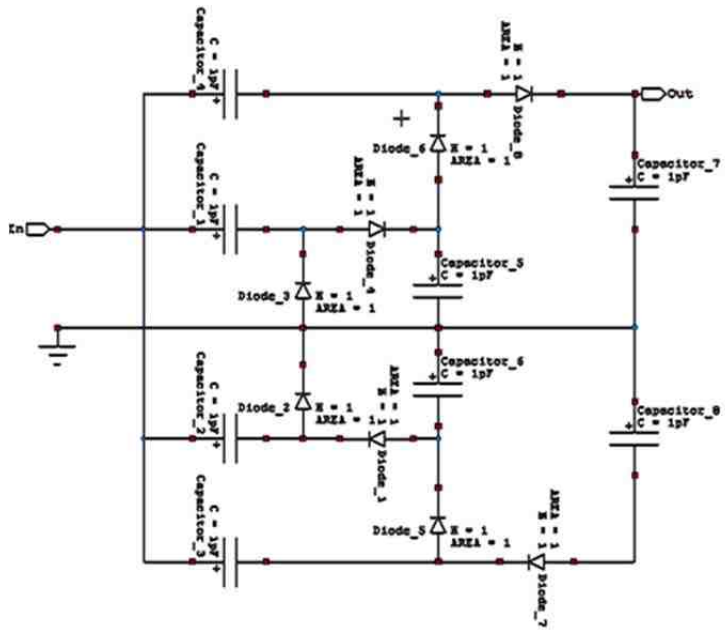

Figure 110. Two-stage, full-wave Dickson rectifier circuit schematic.

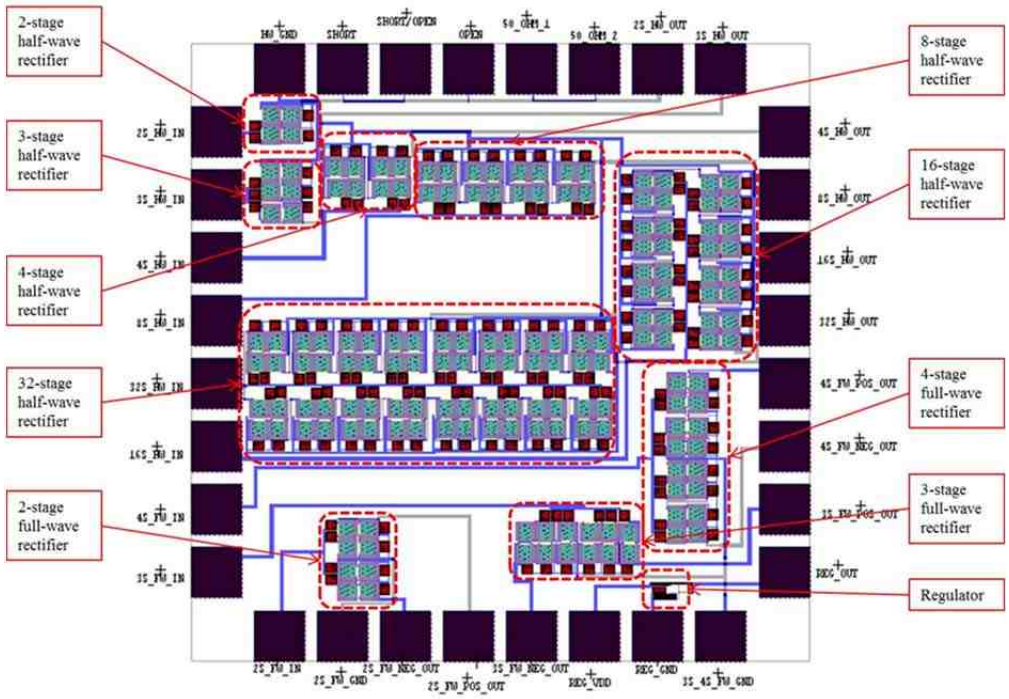

Figure 111. Multi-stage Dickson rectifier circuit layout.

المنارة للاستشارات
www.manaraa.com

Table 20. Multi-stage Dickson rectifier circuit bonding table.

Pin	Description	Pin	Description
3	3-Stage half-wave output	66	2-Stage full-wave in
6	2-Stage half-wave output	69	2-Stage full-wave ground
9	Calibration – 50 Ohm - 1	71	2-Stage full-wave neg out
11	Calibration – 50 Ohm - 2	74	2-Stage full-wave pos out
14	Calibration - open	77	3-Stage full-wave neg out
17	Calibration – open/short	78	Regulator VDD
18	Calibration - short	81	Regulator ground
30	Half-wave ground	83	3&4-Stage full-wave GND
33	2-Stage half-wave in	86	Regulator out
36	3-Stage half-wave in	99	3-Stage full-wave pos out
39	4-Stage half-wave in	101	4-Stage full-wave neg out
41	8-Stage half-wave in	104	4-Stage full-wave pos out
44	32-Stage half-wave in	107	32-Stage half-wave out
47	16-Stage half-wave in	108	16-Stage half-wave out
48	4-Stage full-wave in	111	8-Stage half-wave out
51	3-Stage full-wave in	113	4-Stage half-wave out

6.3.3.1 Direct RF-to-DC Conversion Tests

A 50 Ω test fixture was fabricated on a FR-4 printed circuit board and the IC die was fixed to the board using a silver epoxy. Connections between the bond-pads of the IC and the input, output, and ground of the test fixture were performed with a ball-bonder using gold bond-wires. The test fixture is shown in Figure 112.

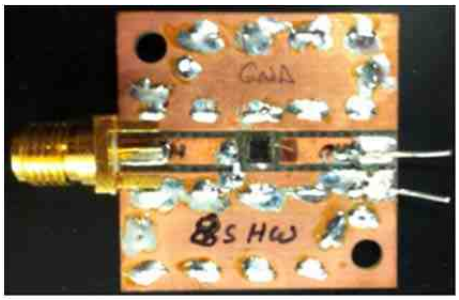

Figure 112. Rectifier 50Ω test fixture.

The input of the test piece was connected to the output of a Mini-Circuits ZHL-4240 amplifier. The input of the amplifier was driven using a 915MHz, 2 mV peak signal from an Agilent 8648C signal generator. The output DC voltage was measured using a

المنارة للاستشارات
www.manaraa.com

Fluke 87V digital multimeter. The signal generator output voltage was increased in steps of 1 mV. The test results are shown in Figure 113. The half-wave rectifiers outperformed the full-wave rectifiers by a factor of more than 2; however, these tests were performed in order to determine if the rectifiers work and not as an indication of the actual performance of the rectifiers when connected to the electrically small antenna.

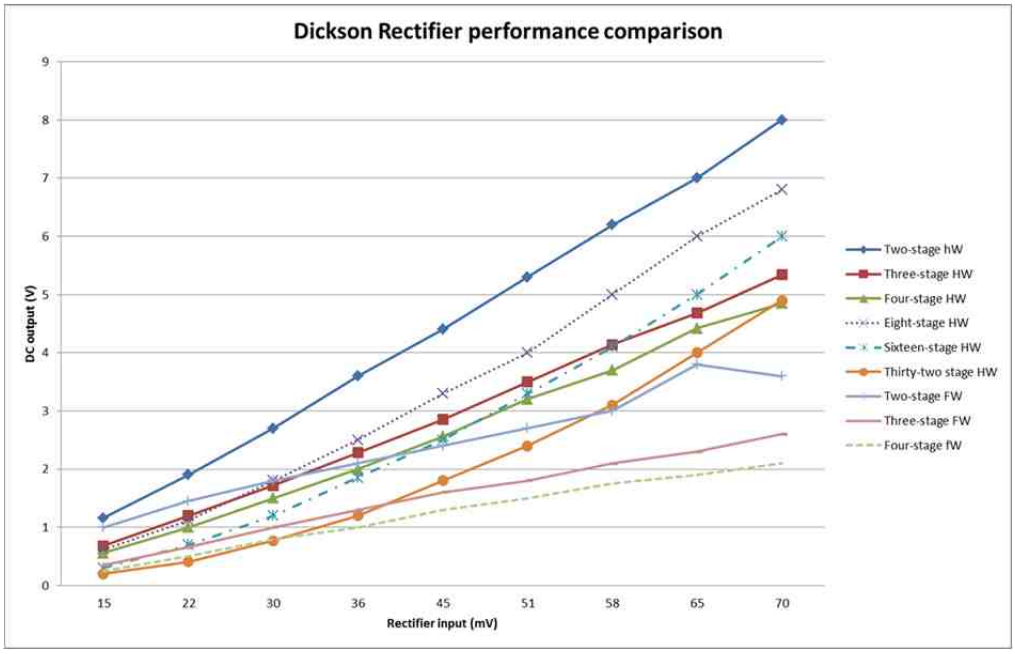

Figure 113. Direct RF-to-DC rectifier performance comparison.

6.3.3.2 Radiated RF-to-DC conversion

Three types of measurement setups were used to determine the capability of the best performing direct RF-to-DC conversion rectifiers to convert an RF signal to DC power. In the first setup, the receiving antenna was connected to the relevant pins on the PGA121M IC package. Measurements were made with a half-wave dipole and an electrically small meander dipole antenna used as the receiving antenna, respectively. The test setup is shown in Figure 114.

المنارة للاستشارات
www.manaraa.com

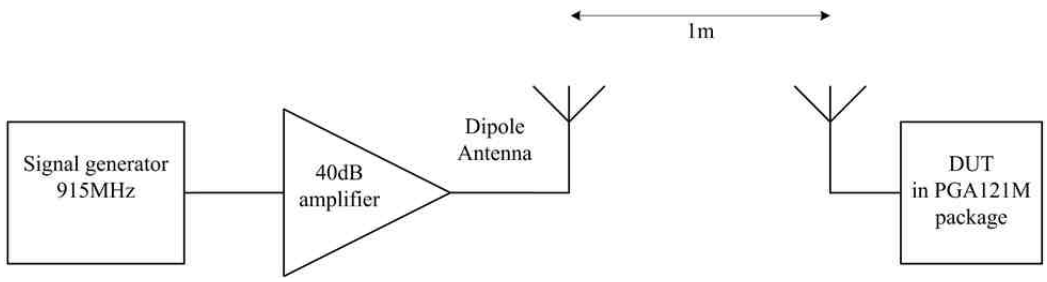

Figure 114. Test setup for radiated RF-to-DC conversion: circuit in PGA package.

The DC output was measured directly at the relevant output pins of the rectifier circuits using a Fluke 87V multi-meter. The transmit frequency was also adjusted to obtain the maximum DC output voltage. For all the measurements, the maximum DC output voltage was obtained at a frequency different from the original designed frequency of 915 MHz.(Table 21). This deviation was attributed to the following:

- The antennas were not perfectly tuned to 915 MHz.
- The antennas were further detuned when they were connected to the pins on the PGA package.

Table 21. RF-to-DC test results with circuit in PGA package.

TX and RX antennas horizontal and inline								
Test piece	**Circuit**	**RX Ant**	**DC output voltage – 0.5 m**			**DC output voltage – 1 m**		
			915 MHz	**Max output**		**915 MHz**	**Max output**	
				V	**Freq (MHz)**		**V**	**Freq (MHz)**
1	Two-stage half-wave	Dipole	1.3	2.6	895	0.7	1.5	901
		Meander	0.1	1.1	946	0.1	0.25	946
2	Three-stage half-wave	Dipole	1.5	1.8	900	1.2	1.5	900
		Meander	0.02	2	983	0.19	1	983
3	Four-stage half-wave	Dipole	3	4	922	1.2	1.4	920
		Meander	0.25	0.5	983	0.15	0.44	983
4	Eight-stage half-wave	Dipole	1	2.3	925	0.5	0.9	953
		Meander	No output recorded					
7	Two-stage full-wave	Dipole	1.9	3	924	1.1	1.7	900
		Meander	No output	0.65	946	No output	0.55	946

المنارة للاستشارات
www.manaraa.com

The IC die was fixed to a 50 Ω test fixture using silver epoxy in the second test setup. The DC output voltage was measured directly at the output of the rectifier using a multimeter as shown in Figure 115. Measurement results with both transmit and receive antennas horizontal and in-line are shown in Table 22.

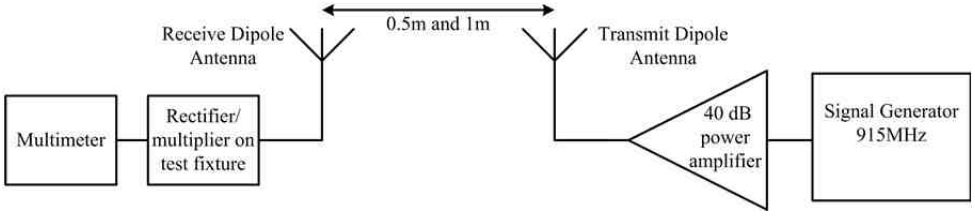

Figure 115. Test setup for RF-to-DC conversion: Circuit on test fixture.

Table 22. DC voltage generated with circuit on 50 Ω test fixture.

TX and RX antennas horizontal and inline								
Test piece	**Circuit**	**RX Ant**	**DC output voltage – 0.5 m**			**DC output voltage – 1 m**		
			915 MHz	**Max output**		**915 MHz**	**Max output**	
				V	**Freq (MHz)**		**V**	**Freq (MHz)**
1	Two-stage half-wave	Dipole	2	4.3	883	1	2.5	881
		Meander	1	1.1	915	0.3	0.5	903
2	Three-stage half-wave	Dipole	5.8	7	887	2.1	3	881
		Meander	0.7	0.8	919	0.23	0.8	904
3	Four-stage half-wave	Dipole	5.3	5.7	885	1.6	2.7	904
		Meander	0.75	0.9	919	0.13	0.8	880
4	Eight-stage half-wave	Dipole	7.9	9	935	2.9	4.3	905
		Meander	1.3	1.5	921	0.2	1.2	881
5	Sixteen-stage half-wave	Dipole	6.5	9.2	935	1.5	2.9	905
		Meander	0.26	0.4	921	No output recorded		
6	Thirty-two-stage half-wave	Dipole	Faulty bonding - No output recorded					
		Meander						
7	Two-stage full-wave	Dipole	2.6	3.6	932	1.2	2.1	905
		Meander	1.2	1.6	929	0.4	1	935
8	Three-stage full-wave	Dipole	Faulty bonding – No output					
		Meander						
9	Four-stage full-wave	Dipole						
		Meander	0.9	1.8	932	0.25	0.4	932

المنارة للاستشارات
www.manaraa.com

Higher voltages were generated when the antennas were not perfectly aligned. Further tests were performed to investigate the effect of misalignment. Significantly higher voltages were generated when the transmit and receive antennas were offset by approximately 40 degrees. The results of these tests are summarized in Table 23.

Table 23. DC voltages generated with antennas oriented for maximum output.

Antenna orientation for max output – TX: Dipole; RX: Meander					
Test piece	**Circuit**	**DC output voltage – 0.5 m**		**DC output voltage – 1 m**	
		Freq (MHz)	**Voltage and Orientation**	**Freq (MHz)**	**Voltage and Orientation**
1	Two-stage half-wave	915	1.3 V at 40°offset from in-line.	903	0.7 V at 40°offset from in-line.
2	Three-stage half-wave	919	0.9 V at 40°offset from in-line.	904	1 V at 40°offset from in-line.
3	Four-stage half-wave	919	1.2 V at 40°offset from in-line.	880	1.2 V at 40°offset from in-line.
4	Eight-stage half-wave	881	3 V at 40°offset from in-line.	881	2.5 V at 40°offset from in-line.
5	Sixteen-stage half-wave	921	0.8 V at 40°offset from in-line.	No output recorded	
6	Thirty-two-stage half-wave	Faulty – No output			
7	Two-stage full-wave	929	1.6 V at 40°offset from in-line.	935	1 V at 40°offset from in-line.
8	Three-stage full-wave	Faulty – no output			
9	Four-stage full-wave	932	1.8 V at 40°offset from in-line.	932	0.5 V at 40°offset from in-line.

Some of the DC voltages generated were unexpectedly high. The test fixture was revised to investigate the effect of the multi-meter leads. The printed circuit board of the ESA was altered to accommodate the IC die directly on the board. The die was fixed to the board using silver epoxy and connections between the copper traces on the board and the bond-pads on the IC were made using a ball bonder. The revised PCB is shown in

المنارة للاستشارات
www.manaraa.com

Figure 116. A 220 μF storage capacitor was added so that the DC voltage generation capabilities of the rectifiers could be measured without the measuring leads being connected to the circuit during transmission of the RF signal. The measurement setup is shown in Figure 117 and the results are shown in Table 24.

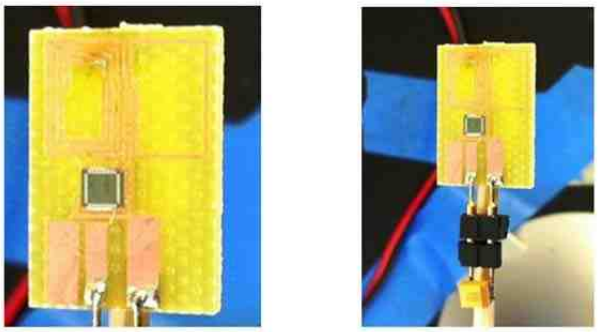

(a) (b)

Figure 116. (a) IC die fixed to antenna PCB (b) Storage capacitor added.

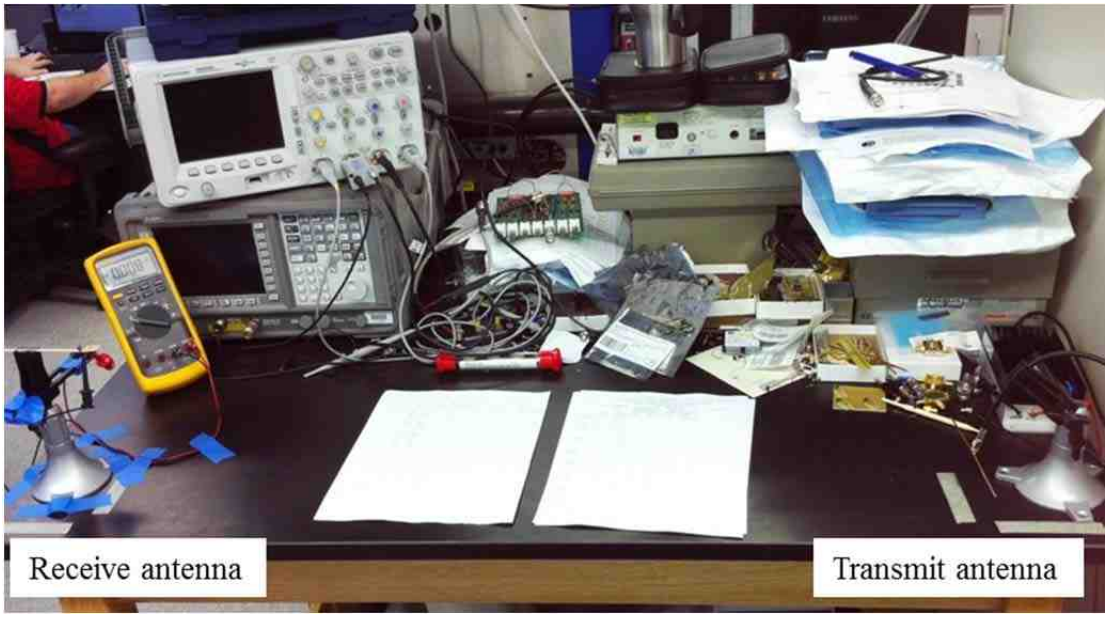

Figure 117. Test setup for determining effect of multi-meter leads.

المنارة للاستشارات
www.manaraa.com

Table 24. DC output voltage of Dickson half-wave rectifiers.

Circuit	Using multimeter leads *(Column 1)*		Using co-ax cable connected directly to output of rectifier *(Column 2)*		Using 220 µF storage capacitor on output of rectifier *(Column 3)*
	V at 915 MHz	Max V and freq (MHz)	V at 915 MHz	Max V and freq (MHz)	DC Voltage at 915 MHz (Measured after 5 minutes of RF transmission)
2-stage half-wave	4.04 V	4.1 V(918)	3.9 V	3.9 V (915)	0.13 V
3-stage half-wave	6.1 V	6.1 V(915)	5.2 V	5.2 V(915)	0.23 V
4-stage half-wave	6.5 V	7.5 V (910)	5.2 V	5.7 V (912)	0.38 V
8-stage half-wave	3.1 V	3.6 V(907)	2.7 V	2.9 V(910)	0.13V

The test results shown in Table 24 were obtained by measuring the DC voltages using the standard multi-meter leads (*Column 1*) and then using a coaxial cable (*Column 2).* These measurements were made during transmission of the RF signal. The third column (*Column 3*) in Table 24 shows the DC voltage measured on the storage capacitor. The RF signal was transmitted for 5 minutes and the DC voltage was measured directly after transmission was suspended. Results are only shown for the 2, 3, 4 and 8-stage rectifiers since they were the only circuits that generated a measurable voltage on the storage capacitor. The effect of the test equipment measuring leads is evident in the results. In the case of 4-stage rectifier a DC voltage of 6.5 V was measured using the multi-meter leads during transmission and only 0.38 V was measured on the storage capacitor. This is an indication of the large errors that are introduced by using measurement leads connected to the test piece during RF transmission. All further tests on the rectifier circuits were performed using a storage capacitor connected to output of the rectifier circuit. The test setup for measuring the DC voltage generated on the storage capacitor is shown in Figure 118.

المنارة للاستشارات
www.manaraa.com

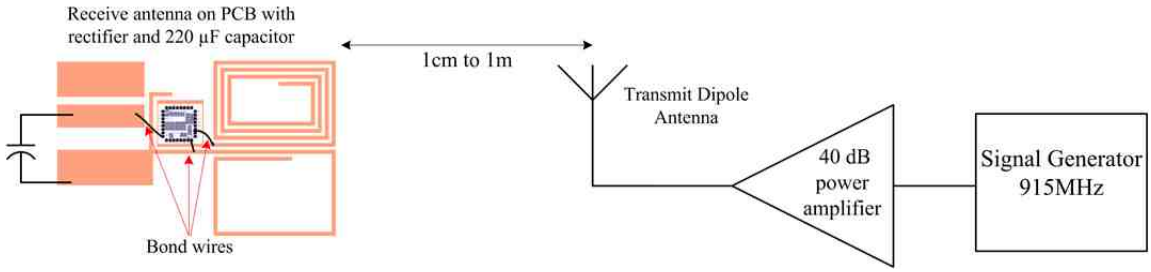

Figure 118. Test setup for measuring DC voltage across storage capacitor.

Both transmit and receive antennas were at the same height of 16.5 cm above the table. The antennas were both horizontal and in-line with each other. In all cases, the transmitter was activated for 1 minute and then switched off. A 1-minute transmission time was used to save time in completing the tests. Prior testing showed a negligible difference between transmitting for 5 minutes and transmitting for 1 minute. The voltage across the storage capacitor (220 µF) was measured within 5 seconds after the transmitter was switched off. The test data is shown in Table 25 and graphically illustrated in Figure 119.

Table 25. DC voltages measured across storage capacitor.

Circuit	TX activated for 1 min. Using 220 µF storage capacitor on output of rectifier. Voltage measured immediately after switching RF off										
	DC output voltage (V)										
	CW 915 MHz signal, -12.2 dBm out of sig gen => 1 W EIRP										
	Distance (m) – antennas inline and at same height										
	1	0.5	0.4	0.3	0.2	0.15	0.13	0.10	0.08	0.05	0.025
4-stage half-wave	0.013	0.02	0.32	0.58	0.93	0.84	0.6	1.2	1.4	2.1	5.5
	CW 915 MHz signal, -7 dBm out of signal gen => 1.5 W EIRP										
4-stage half-wave	0.02	0.06	0.6	0.7	1.1	1.23	1.3	1.84	2.24	3.18	6.4
	CW 915 MHz signal, -7 dBm out of signal gen => 1.5 W EIRP										
2-stage half-wave	0.031	0.012	0.228	0.3	0.48	0.45	0.334	0.6	0.7	1.4	2.7
	CW 915 MHz signal, -7 dBm out of sig gen => 1.5 W EIRP										
3-stage half-wave	0.018	0.04	0.4	0.54	0.48	0.84	0.9	1.4	1.55	2.2	4.5
	CW 915 MHz signal, -7 dBm out of sig gen => 1.5 W EIRP										
8-stage half-wave	0	0	0.17	0.27	0.36	0.28	0.46	0.7	1.33	1.35	2.5

المنارة للاستشارات
www.manaraa.com

A powering range of up to 7 cm is possible if a DC supply voltage of 2 V is used and a range of up to 20 cm is possible if a DC supply voltage of 1 V is used to drive the rest of the circuits. The test bench affected the performance of the rectifier circuits. Better performance was obtained when the transmitting antenna (wire dipole) was 5 cm above the table than when it was 16.5 cm above the table. The receiving antenna was kept at a height of 16.5 cm above the table. Further tests were performed to investigate the effect of the table. The four-stage rectifier produced the highest DC voltage that was on average 0.6 V more than that produced by the next best performer, which was the three-stage rectifier. Most of the further tests and evaluations were performed using the four-stage Dickson rectifier.

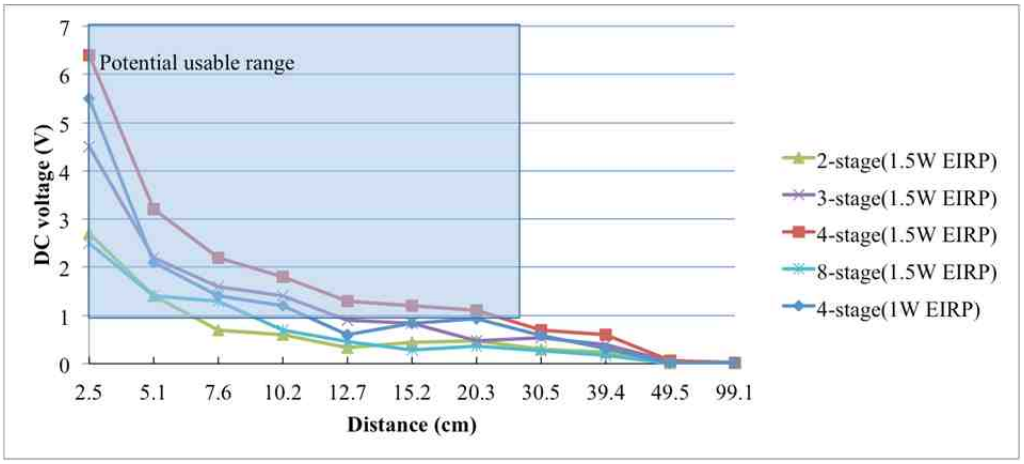

Figure 119. Potential range for powering of implantable device.

More detailed simulations were performed to compare the performance of the 4-stage Dickson rectifier with measured results. Typical input voltages to the rectifier at different distances were obtained and used in the simulations. The input voltage was measured using an electrically small meander dipole antenna (ESA) connected to an Agilent oscilloscope. A half-wavelength dipole antenna was used as the transmit antenna.

المنارة للاستشارات
www.manaraa.com

Both transmit and receive antennas were at the same height of 16.5 cm above the test bench. The antennas were both horizontal and in-line with each other. A -2 dBm, 915 MHz sinusoidal signal was generated by the signal generator and used as input to the power amplifier. Cable losses were measured as 2 dB. The effective radiated power of the dipole antenna was calculated by adding the 40 dB amplification provided by the amplifier to the -2 dBm signal from the signal generator and subtracting the cable losses, resulting in a radiated power of 36 dBm (4 W). The measurements were repeated using an Agilent E4402B spectrum analyzer as verification. The test setup is shown in Figure 120 and the measured results shown in Figures 121 and 122.

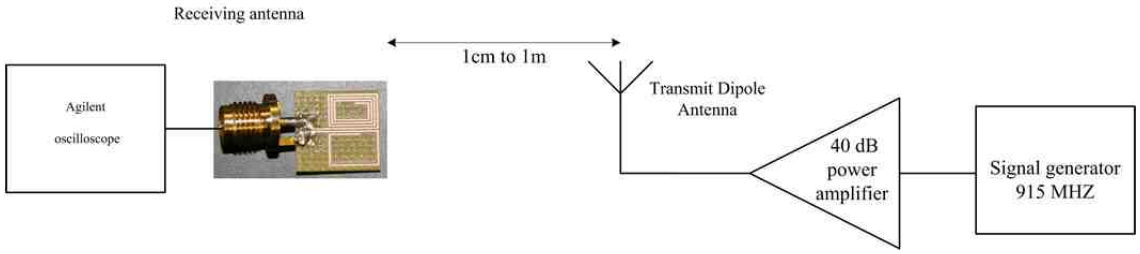

Figure 120. Test setup for measuring input voltage to rectifier.

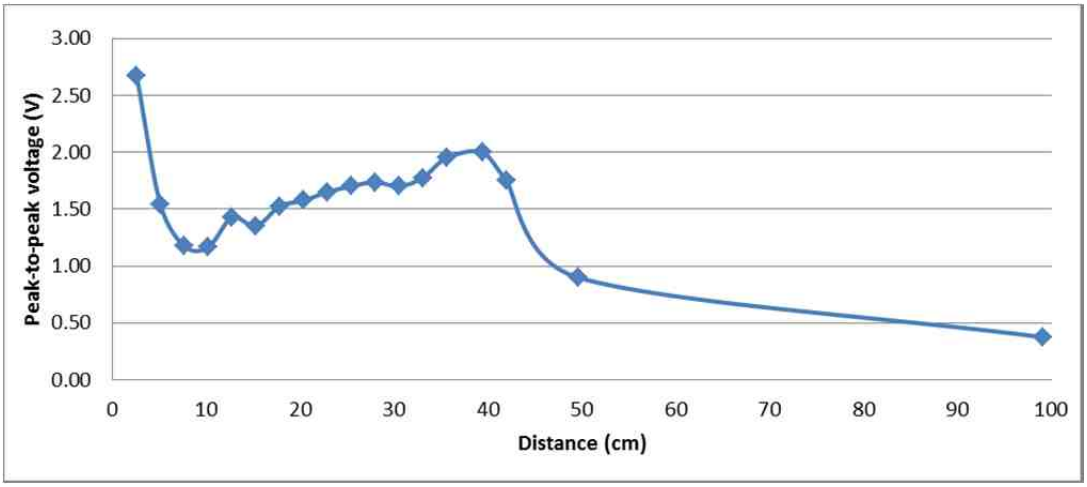

Figure 121. Output voltage of ESA measured on oscilloscope.

المنارة للاستشارات
www.manaraa.com

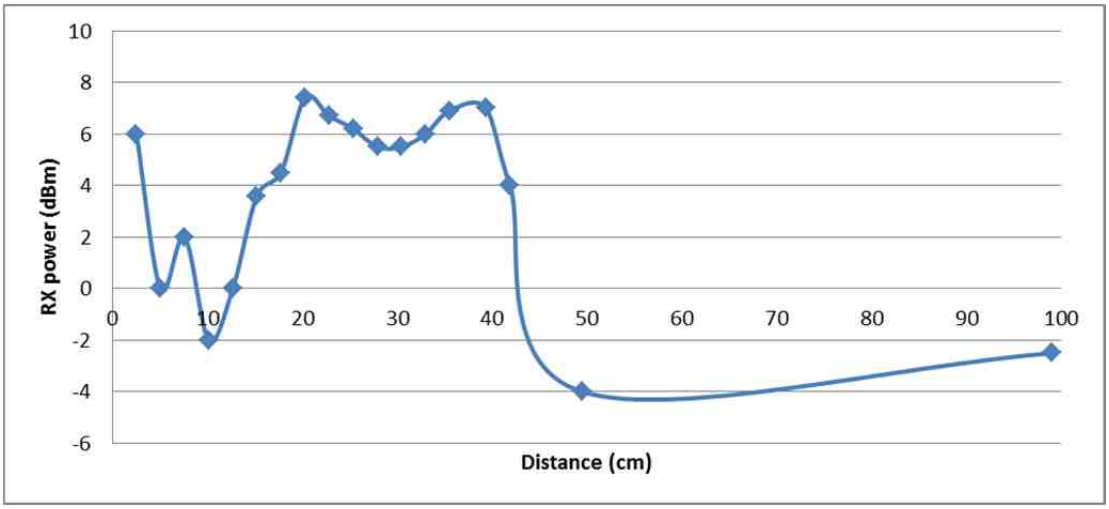

Figure 122. Output power of ESA measured on spectrum analyzer.

The received voltage measured with the oscilloscope and the received power measured with the spectrum analyzer follow a similar pattern as the DC voltage measured at the output of the rectifier. The received voltage measured at the output of the ESA was used as input to the rectifier circuit in the simulations. Simulations were performed using ADS from Agilent technologies. Two measurement cases and the simulated values are shown in Figure 123. In the first case, the transmitter was activated for 1 minute and then switched off. In the second case, the transmitter was activated for 5 minutes and then switched off. The voltage across the storage capacitor (220 μF) was measured directly after the transmitter was switched off.

المنارة للاستشارات
www.manaraa.com

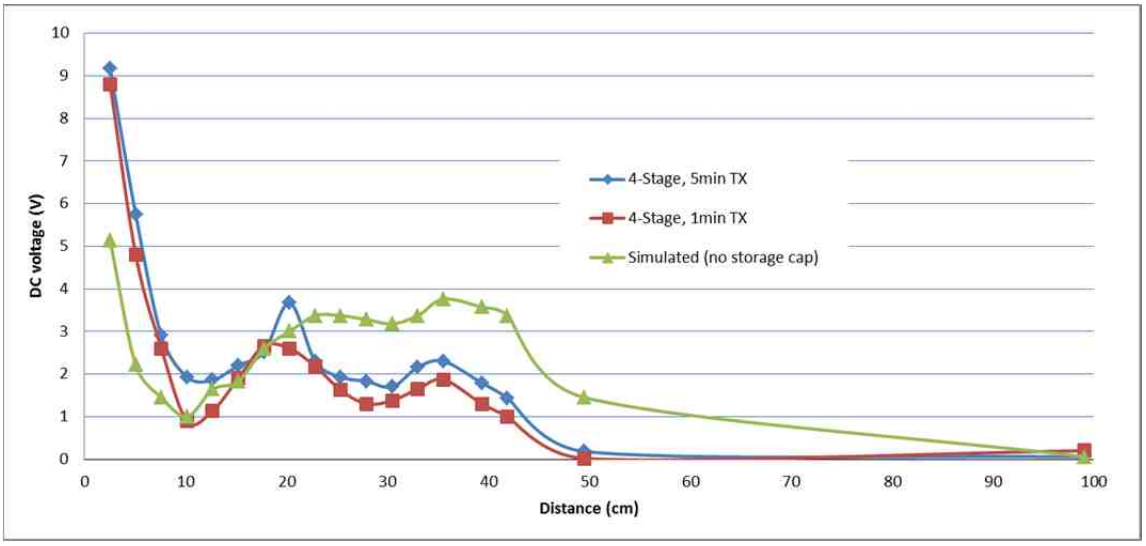

Figure 123. Comparison of simulated and measured DC voltages at output of 4-stage Dickson rectifier.

Simulations were also attempted with a 220 μF storage capacitor, but were not successful. One simulation over a time of 10 ms takes almost 4 hours to complete and shows that the capacitor is still charging. The simulated dc output voltage is only 7.9 mV after 10.001 ms.

The reason for the increase in dc output voltage at 20 and 38 cm is still not clear. The ESA was used as receiving antenna, without the rectifier connected, and measurements showed that the increase in dc output voltage is not due to harmonics. The received power at a distance of 20 cm was 7.4 dBm at 915 MHz, -49 dBm at 1.83 GHz and no signal at 2.745 GHz.

Electromagnetic waves are reflected by any conducting surface that lies within the first Freznel zone of the signal. The first Fresnel zone is a concentric ellipsoid shaped volume that contains the strongest signals between the transmitter and receiver and the radius of the zone was calculated using

المنارة للاستشارات
www.manaraa.com

$$r = \sqrt{\frac{\lambda SD}{S+D}} \tag{6.7}$$

where r is the radius in meters, λ is the wavelength in meters, S is the distance from the transmitter in meters and D is the distance from the receiver in meters [68]. Reflective surfaces that lie within the first Freznel zone will reflect waves that are in-phase with the direct signal and will result in constructive interference and a stronger received signal. A hypothesis was formulated that the increased DC voltages observed at 20 and 38 cm distances was due to constructive interference. The hypothesis was tested by repeating the measurements and removing all reflecting surfaces and equipment outside the radius of the first Fresnel zone of 28.6 cm.

Tests were performed to compare the performance of the 4-stage rectifier with small meander antenna in different locations. Four scenarios were compared: over a test bench, outside in free space, and in different locations in the lab with the antennas at a height of 1.5 m and separated from surrounding equipment by at least 0.6m. In the test bench setup, both transmit and receive antennas were at the same height of 16.5 cm above the table. Free space measurements were taken on a balcony attached to the research building. Both transmit and receive antennas were at a height of 1.5 m above ground level and no other objects were within the maximum first Fresnel zone radius of 28.6 cm. In all cases, the antennas were horizontal and in-line with each other. A -2 dBm, 915 MHz sinusoidal signal was generated by the waveform generator and used as input to the power amplifier. Cable losses were measured as 2 dB resulting in an EIRP of 36 dBm (4 W). The results of the tests are shown in Figure 124.

المنارة للاستشارات
www.manaraa.com

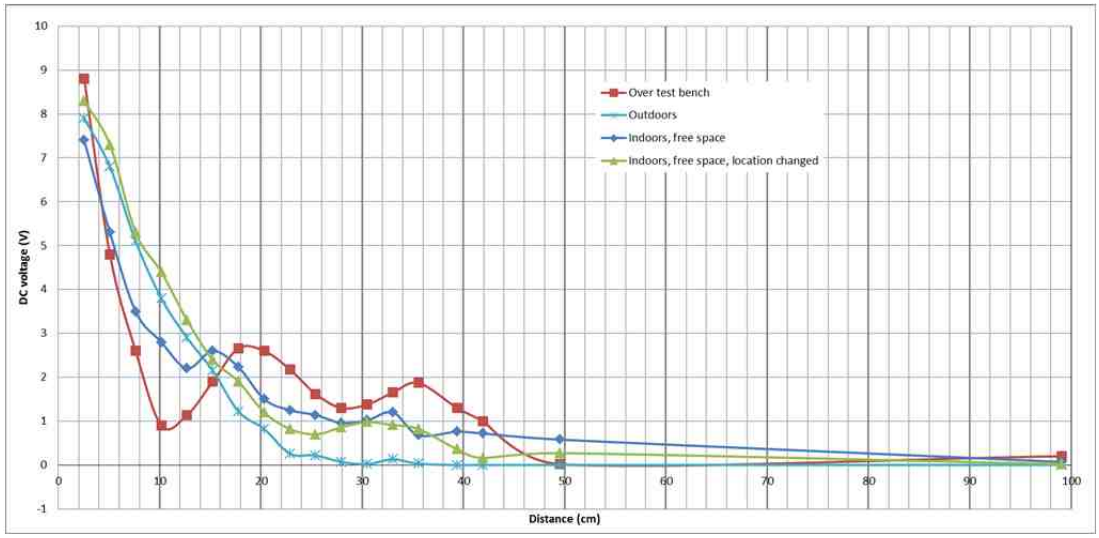

Figure 124. DC voltage generated with distance between antennas, indoors and outdoors.

The results of the outdoor tests proved the hypothesis made previously that the increase in DC voltage generated at certain distances are due to reflections and constructive interference from objects that are in close proximity to the test setup. All the indoor tests showed sudden increases of the DC voltages at distances where it was expected that the voltages would be less. The indoor tests show a potential usable range of approximately 18 cm if 2 V DC voltage is used and a potential usable range of approximately 30 cm if 1 V DC is used. No load was connected to the storage capacitor. Further tests were performed with the oscillator connected to the output of the regulator. These tests are discussed in Chapter 7.

6.4 Voltage Regulator

6.4.1 Background

The DC voltage that was generated by the RF-to-DC rectifier circuit will increase and decrease in accordance with the peak voltage of the received RF signal. The peak voltage of the received signal was affected by the power of the transmitter, the gain of the

المنارة للاستشارات
www.manaraa.com

transmit and receive antennas, the distance between the antennas, and any objects in the vicinity that can cause reflections. The oscillation frequency of the oscillator that forms part of the sensing network is affected by a change in the supply voltage. Therefore, it was necessary to regulate the output of the rectifier to provide a constant DC voltage and to limit the ripple voltage associated with the rectified signal.

A regulator, with reference circuit, is part of the standard cell library used for integrated circuit design at the University of Louisville. This circuit was successfully implemented by Matt Turner [67] for an inductively coupled pressure sensing system. The regulator circuit was used for the system that is described in this dissertation.

6.4.2 Simulation and Layout

The regulator circuit that is available from the standard cell library regulates voltage at 2.7 V DC. For this project, the reference resistor and the adjustment resistor were removed from the chip to gain more control over the regulating voltage. The circuit was simulated using T-Spice from Tanner tools to verify its suitability for use in this application. The circuit schematic is shown in Figure 125. Line-regulation simulations were performed using different resistance values for R_ref and R_adj to evaluate the effect on the regulated output voltage (Figures 126 to 128). A load of 100 kΩ was connected to the output of the regulator.

المنارة للاستشارات
www.manaraa.com

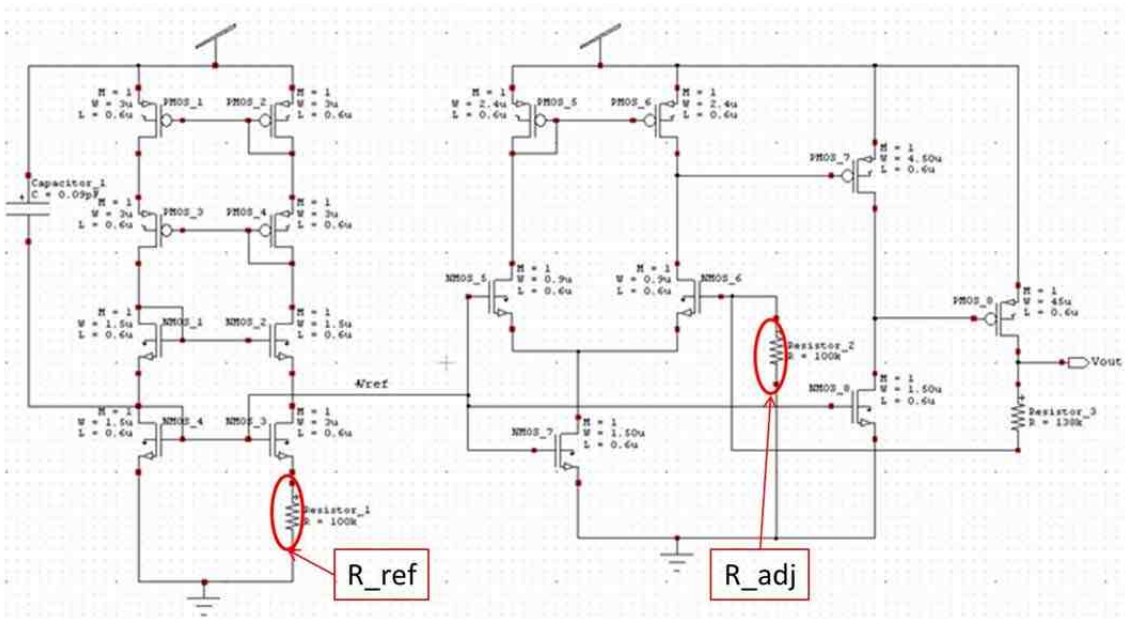

Figure 125. Regulator circuit schematic with voltage reference on the left and regulator on the right. R_ref and R_adj taken off-chip.

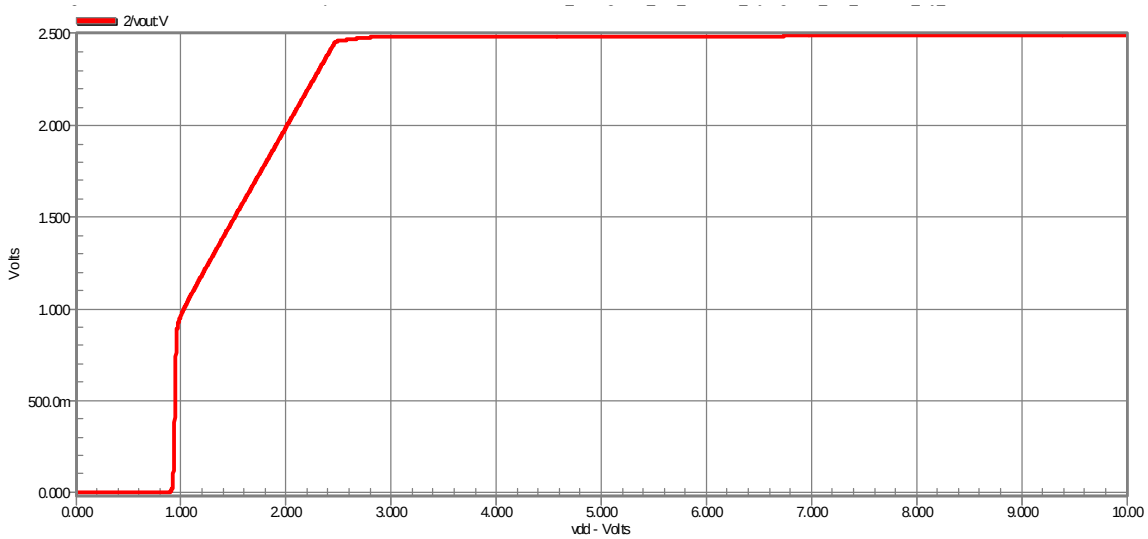

Figure 126. Simulated line regulation: regulated voltage with R_adj = R_ref = 100 kΩ.

المنارة للاستشارات
www.manaraa.com

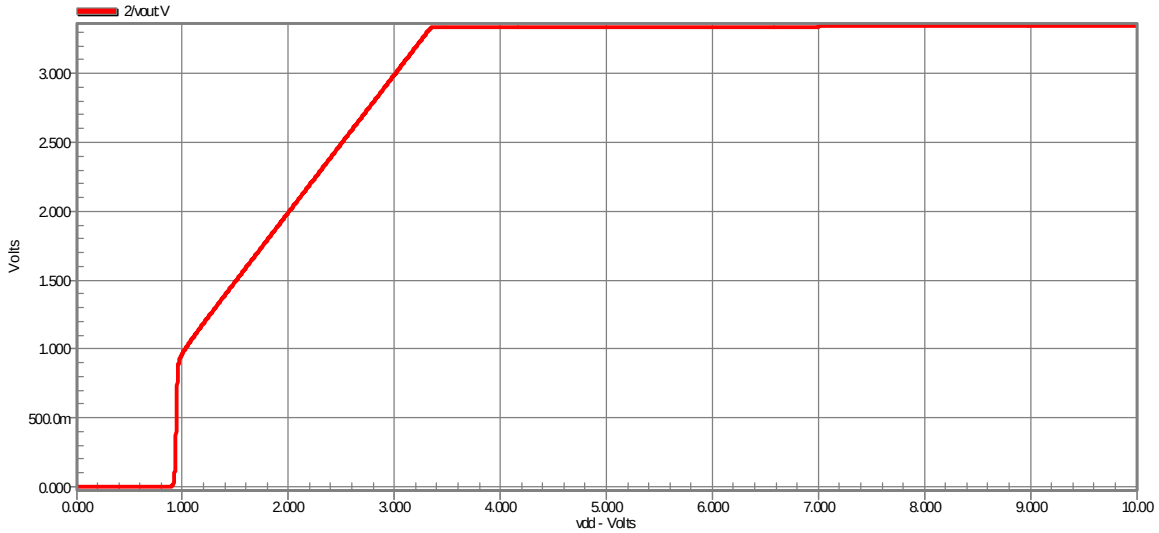

Figure 127. Simulated line regulation: regulated voltage with R_adj = R_ref =68 kΩ.

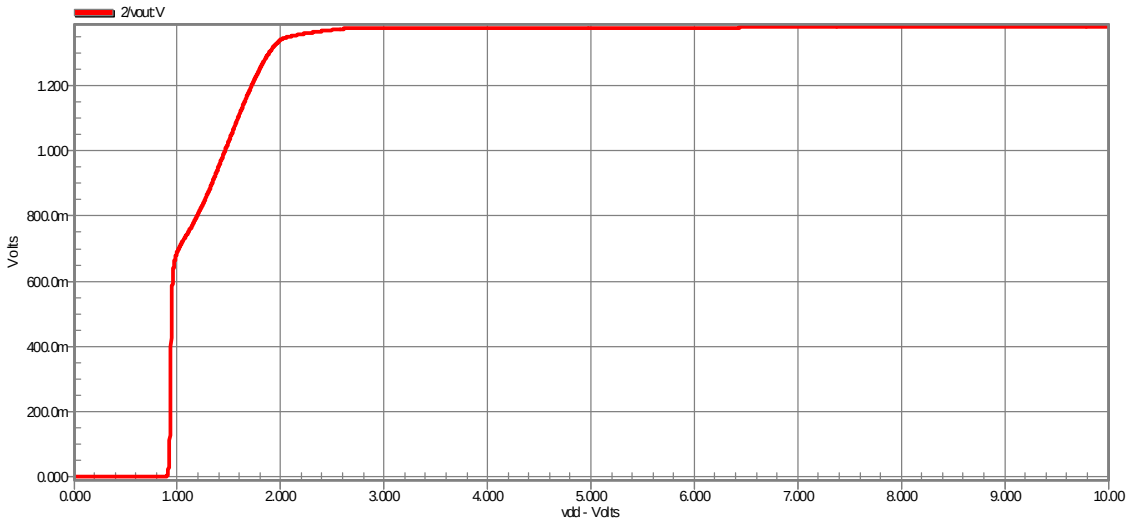

Figure 128. Simulated line regulation: regulated voltage with R_adj = R_ref =270 kΩ.

The simulations suggested that the regulated voltage can be adjusted from 1.4 V to 3.5 V by simply changing the values of R_adj and R_ref. Keeping the supply voltage constant at 5 V and varying the load from 1 kΩ to 1 MΩ also simulated the load regulation. The simulated load regulation results are shown in Figure 129. The circuit

المنارة للاستشارات
www.manaraa.com

layout was implemented with L-Edit from Tanner Tools and was fabricated using the 0.5µm CMOS process from On Semiconductor through the MOSIS service.

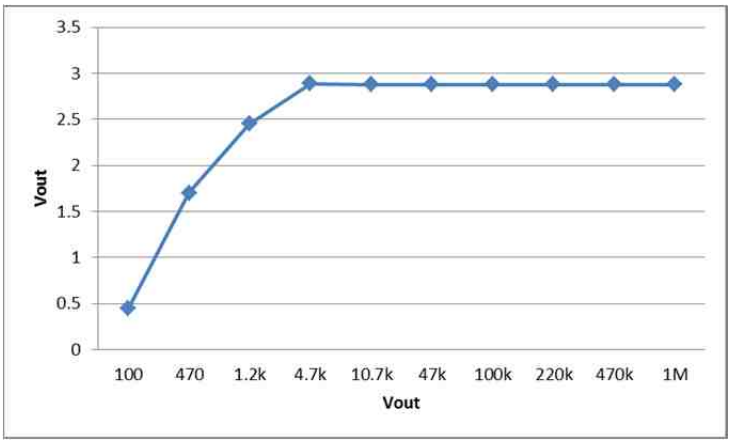

Figure 129. Simulated load regulation.

The simulations were verified with measurements made in the laboratory. The regulator was supplied with an input voltage from a DC power supply that was varied from 1 to 10 V. Different resistance values were used for R_ajd and R_ref and the output voltage of the regulator was measured using a Fluke multi-meter. The results are shown in Figure 130.

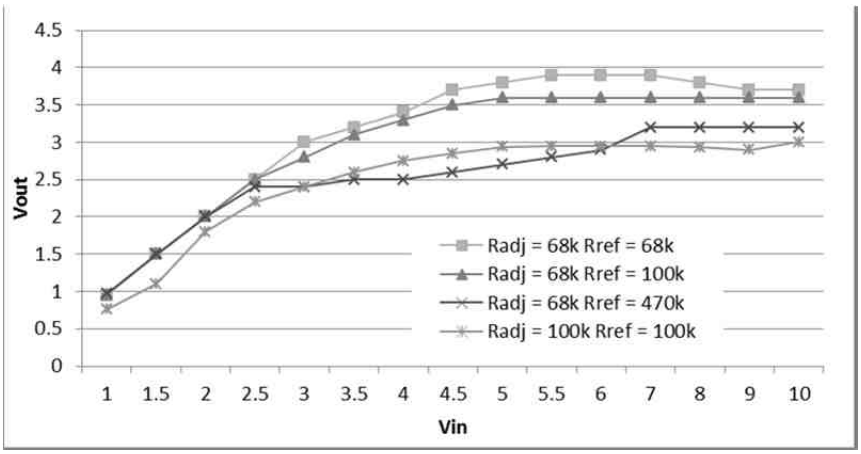

Figure 130. Measured line-regulation with different resistance values for Radj and Rref.

المنارة للاستشارات
www.manaraa.com

The performance of this regulator was compared to the performance of two other regulators that were implemented at the University of Louisville. Students James Willett and Adam Cahill, as part of a class project, implemented the first design in 2009. Matt Turner, as part of his PhD dissertation, implemented the second design in 2009. The designs are identical in terms of circuit configuration and only differ with respect to the resistors. In the first two designs, the resistor values are different. In the last design, the voltage reference resistor (Resistor_1/R_{ref}) and the voltage regulator resistor (Resistor_2/R_{adj}), were taken off-chip. The resistor values used are shown in Table 26. These values were obtained from the L-Edit SPICE extraction files. All resistors were laid out and fabricated using high resistance poly-silicon. The layout of each circuit is shown in Figure 131. Load regulation and line regulation of each regulator were measured and the results are shown in Figures 132 to 134. The regulator developed by Turner was part of a larger integrated circuit and the load could not be varied externally. The load regulation shown for the Turner regulator in Figure 133 is from measurements made during the development of that system

Table 26. Resistor values of regulator circuits.

	Willet/Cahill	Turner	Faul
Resistor_1/R_{ref}	106 kΩ	114 kΩ	Off-chip
Resistor_2/R_{adj}	202 kΩ	114 kΩ	Off-chip
Resistor_3	338 kΩ	157 kΩ	157 kΩ

المنارة للاستشارات
www.manaraa.com

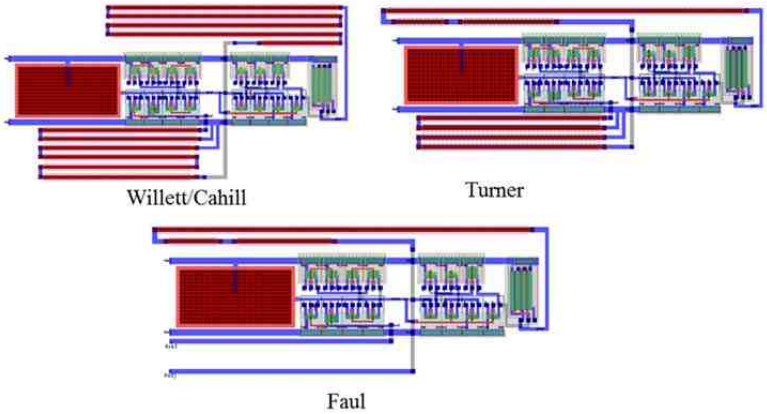

Figure 131. Regulator circuit layout.

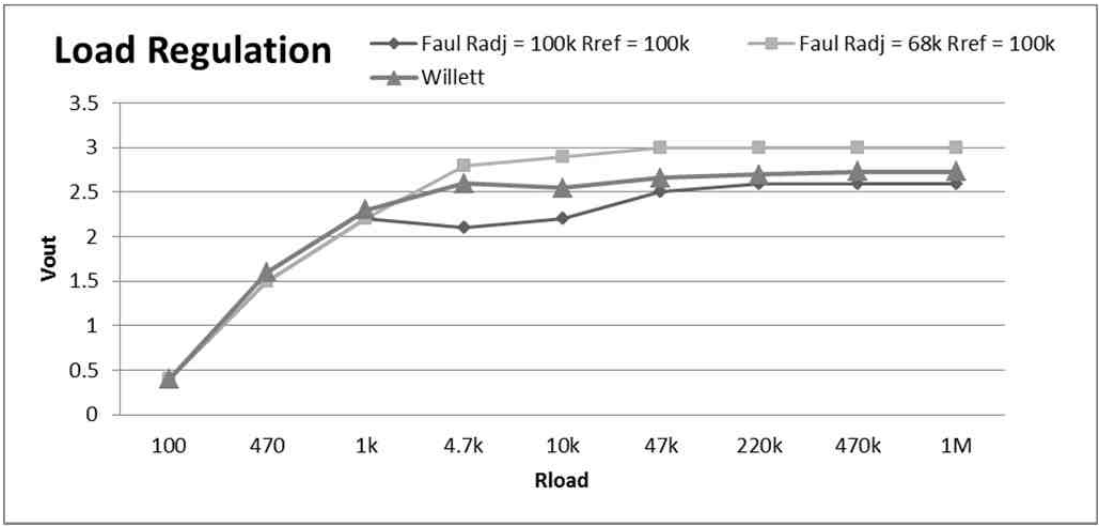

Figure 132. Load regulation comparison.

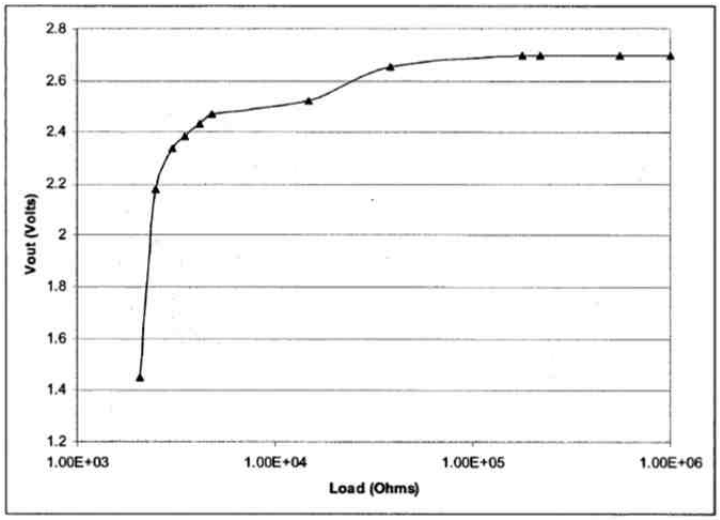

Figure 133. Load regulation – Turner regulator [67].

المنارة للاستشارات
www.manaraa.com

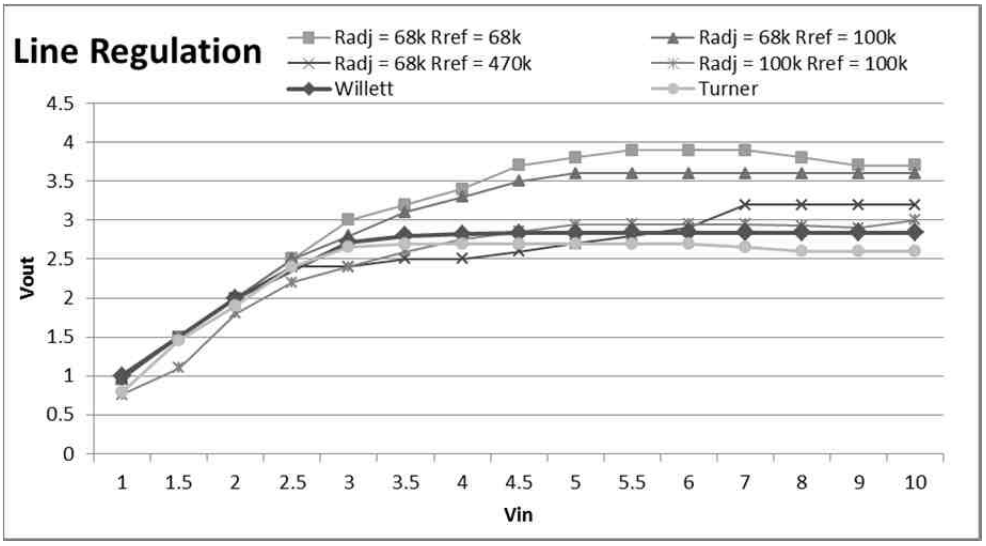

Figure 134. Line regulation comparison.

Load and line regulation for the regulator with off-chip reference and adjustment resistors were not as consistent and stable as those that had integrated resistances, as illustrated in Figure 134. Therefore, further implementation of the regulator was performed with on-chip resistors. The layout was performed in L-Edit from Tanner Tools (Figure 135) and the regulator was fabricated using the 0.5 µm CMOS process from On-Semiconductor through the MOSIS service. A resistance value of 114 kΩ was used for both Radj and Rref to provide a regulated output voltage of 2.5 V. Load regulation and line regulation were measure in the laboratory. Comparisons of the measured and simulated values are shown in Figures 136 and 137.

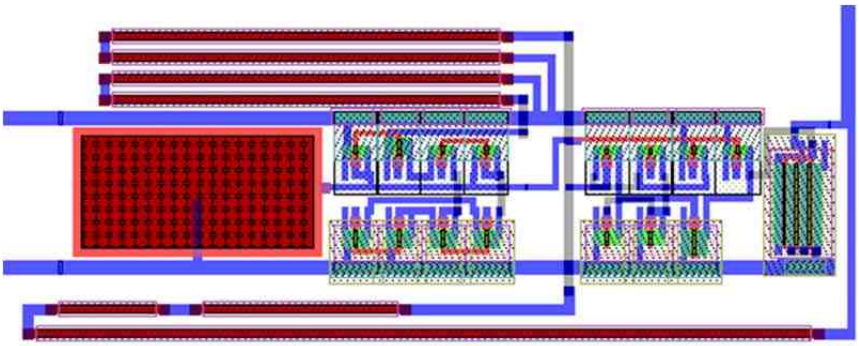

Figure 135. Regulator layout with Radj=114 kΩ and Rref = 114 kΩ.

المنارة للاستشارات
www.manaraa.com

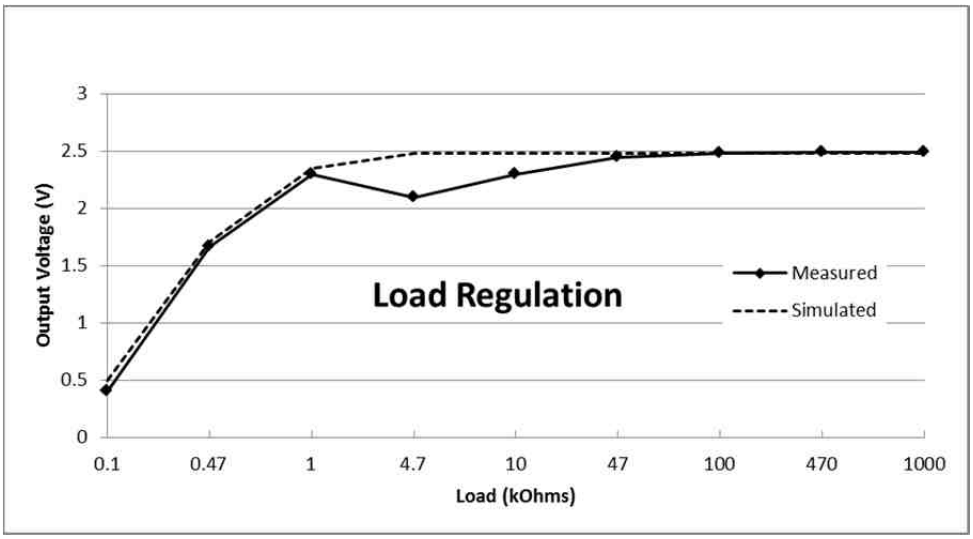

Figure 136. Comparison of simulated and measured load regulation.

The measured and simulated load regulation values differ by less than 0.1 V except for a drop in the measured regulated voltage at a load of 4.7 kΩ where the difference is 0.4 V. The measured and simulated load regulation values are within 0.036 V for loads in excess of 47 kΩ. The measured and simulated line regulation values differ by a maximum of 0.07 V and are within 0.04 V for input voltages greater than 3 V. The regulator circuit was used in all further IC versions.

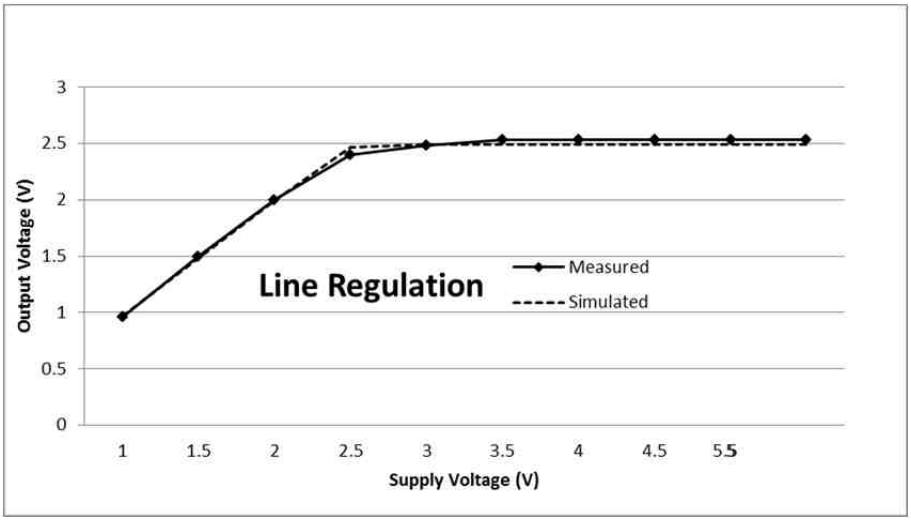

Figure 137. Comparison of measured and simulated line regulation.

المنارة للاستشارات
www.manaraa.com

CHAPTER 7. SYSTEM TESTING AND RESULTS

7.1 IC pin layout and bonding diagram

Several test pieces were fabricated using the 0.5 µm CMOS process from On Semiconductor through the MOSIS service. The test pieces were based on the designs that were fabricated and tested previously and described in Chapter 6. The chip contained a four-stage Dickson rectifier using Schottky diodes, the regulator circuit, a 10 nH planar inductor and three Colpitts oscillator designs. The oscillator circuits used identical configurations; however, different MOSFET gate widths were used for each of the designs. The circuit layout is shown in Figure 138. The fabricated bonding diagram is shown in Figure 139 with pin descriptions in Table 27.

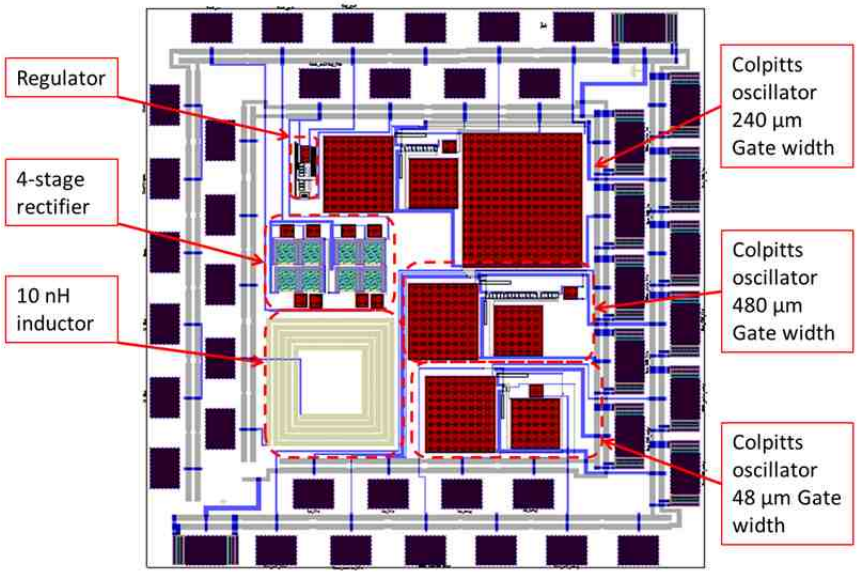

Figure 138. Final test circuit layout.

المنارة للاستشارات
www.manaraa.com

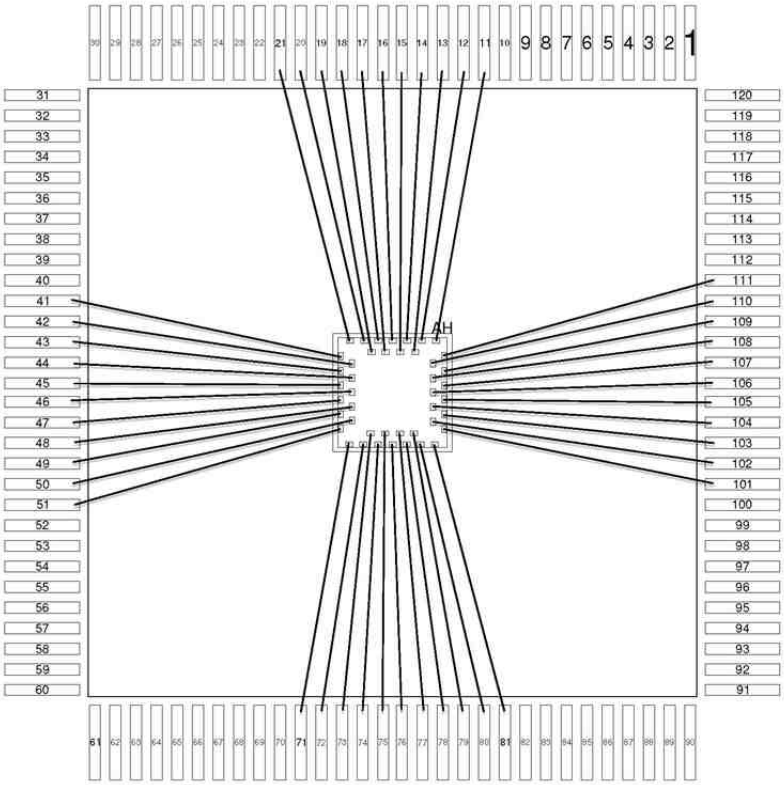

Figure 139. Bonding diagram (IC 89274, MOSIS run V35G-AH).

Table 27. Pin descriptions for test IC.

Pin	Description	Pin	Description
11	GND bus	71	VDD bus
12	La – 240 µm gate width osc	72	Output – 480 µm gate width osc
13	Out – 240 µm gate width osc	73	La – 480 µm gate width osc
14	Lb – 240 µm gate width osc	74	NMOS source – 480 µm gate width osc
15	NMOS source – 240 µm gate width osc	75	Lb – 480 µm gate width osc
17	Regulator output	76	NMOS Source – 48 µm gate width osc
18	Regulator gnd	77	La – 48 µm gate width osc
19	Rectifier out/Regulator VDD	79	Lb – 48 µm gate width osc
20	Rectifier ground	80	Output – 48 µm gate width osc
21	Rectifier input	101	GND – 48 µm gate width osc
41	Calibration short	102	VDD – 48 µm gate width osc
43	Calibration short/open	103	NMOS gate – 48 µm gate width osc
45	Calibration open	104	GND – 480 µm gate width osc
47	Calibration load (50 Ohm)	105	VDD – 480 µm gate width osc
48	Inductor - La	106	NMOS gate – 480 µm gate width osc
49	Calibration load (50 Ohm)	108	GND – 240 µm gate width osc
50	Inductor - Lb	109	VDD – 240 µm gate width osc
		110	NMOS gate – 240 µm gate width osc

المنارة للاستشارات
www.manaraa.com

7.2 Final Circuit Testing

7.2.1 Dickson rectifier/multiplier and regulator

A four-stage Dickson rectifier/multiplier circuit, consisting of Schottky diodes and 1 pF capacitors, were included on the IC. The circuit schematic is shown in Figure 140. The regulator circuit schematic is shown in Figure 141.

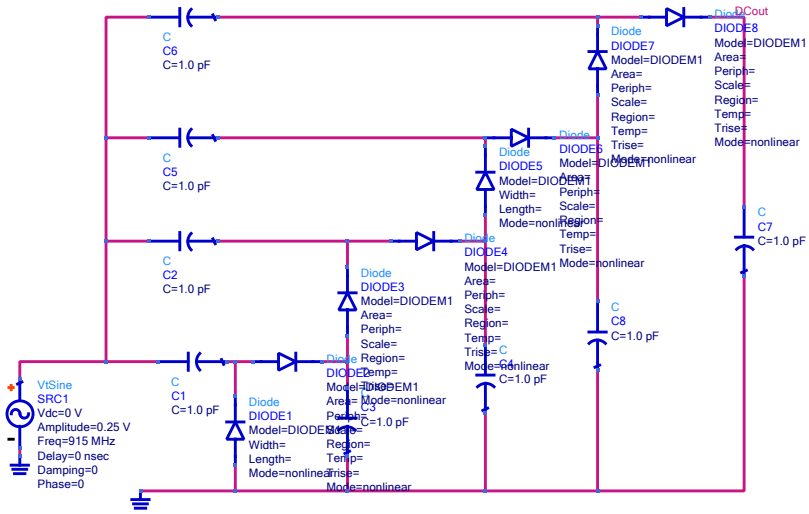

Figure 140. Four-stage Dickson rectifier/multiplier.

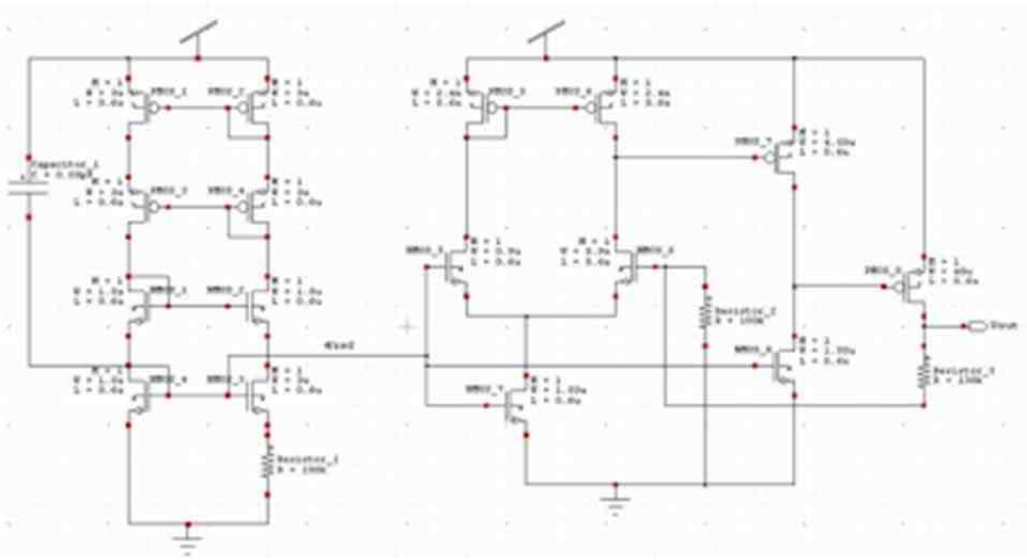

Figure 141. Voltage regulator with reference.

المنارة للاستشارات
www.manaraa.com

The rectifier/multiplier and regulator operations were tested by connecting a small meander dipole antenna to the input of the rectifier. A 220 µF capacitor was connected to ground between the output of the rectifier and the input to the regulator. A 915 MHz, -7dBm signal was generated from an Agilent signal generator and used as input to a Mini-Circuits ZHL-4240 amplifier with 915 MHz dipole antenna connected to the output of the amplifier. The test setup is shown in Figure 142. A regulated voltage of 2.6 V was measured at the output of the regulator when the antennas were separated by approximately 2.5 cm.

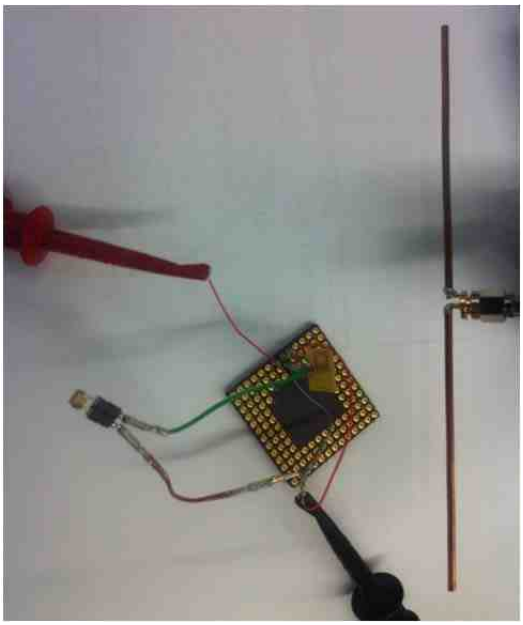

Figure 142. Rectifier/regulator test setup.

7.2.2 Spiral inductor

A spiral inductor was included on the IC. The network analyzer was calibrated using the on-chip calibration ports. The single port S-parameters of the inductor were measured using the network analyzer. The test setup is shown in Figure 143. The test results are shown in Figure 144 and show an inductance value of 6.86 nH that is 30% less

المنارة للاستشارات
www.manaraa.com

than the designed value of 10 nH. Calculations used for the design did not take into account the parasitic components associated with the die and package.

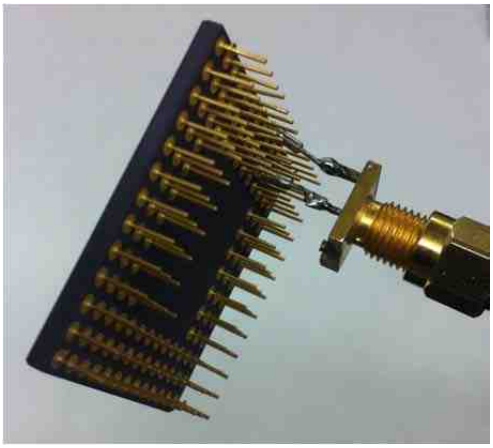

Figure 143: Spiral inductor test setup.

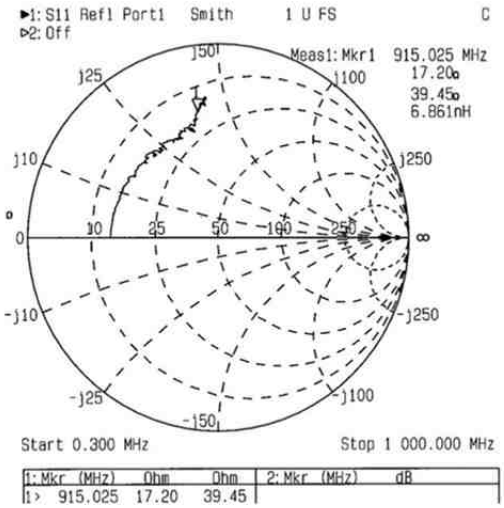

Figure 144: Spiral inductor S11 measurements.

7.2.3 Colpitts oscillator

Three oscillator circuits, with different transistor gate widths, were included on the chip. A variable capacitor (2.5 – 6 pF) was connected between the transistor source

المنارة للاستشارات
www.manaraa.com

terminal and ground. This capacitor represented the pressure sensor. An external inductor was connected in the position as shown in Figure 145.

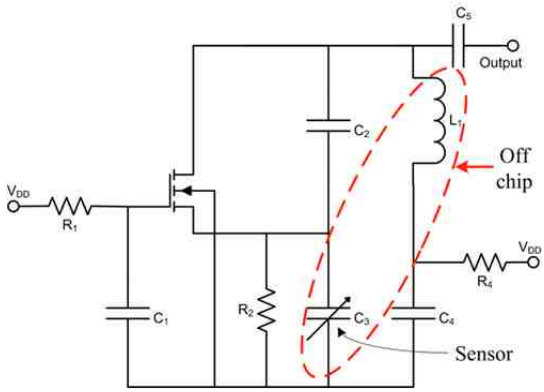

Figure 145. Colpitts oscillator circuit schematic.

Various inductance values were used and the frequency of oscillation, if present, was recorded using a spectrum analyzer. The oscillators were initially tested in a PGA121 test fixture. The results are shown in Table 28. The oscillator, with a transistor gate width of 240 µm, is the only one that includes a 100 pF blocking capacitor on chip. This capacitor was removed from the other circuits due to space limitations on the chip. An external 100 pF capacitor was connected between one terminal of the inductor and ground to test the other two oscillators. Other inductance values between 27 nH to 820 nH were connected to the oscillators but no frequency of oscillation was detected.

Table 28. Oscillator output frequency and power with different inductors.

Oscillator	**Output frequency and power**	
	50 turn coil (28 µH)	**Wire wound inductor (10 µH)**
48 µm gate width	7 MHz, -15 dBm	12.9 MHz, -13 dBm
240 µm gate width	7.65 MHz, -19 dBm	13.45 MHz, -17.4 dBm
480 µm gate width	None	None

المنارة للاستشارات
www.manaraa.com

The 240 µm gate width oscillator was tested by connecting the components directly to the pins of the IC. The test setup is shown in Figure 146. The oscillation frequency and DC characteristics of the 240 µm oscillator was measured with the 10 µH wire wound inductor as shown in Table 29. The oscillator failed to operate with any other inductance value; however the tests did show that the oscillator worked with certain inductance values.

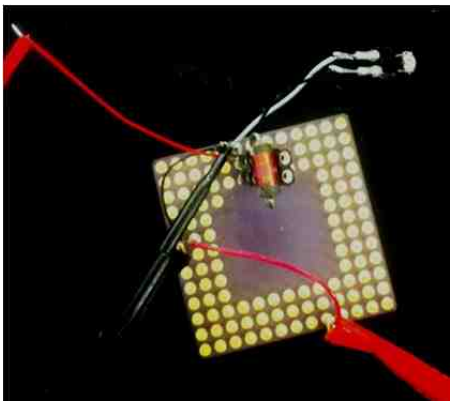

Figure 146. Oscillator test setup.

Table 29. Oscillation frequency and DC characteristics of Colpitts oscillator.

Parameter						
Frequency	*Power*	*Vdd*	*Idd*	*Vd*	*Vs*	*Vds*
16 MHz	-18 dBm	5 V	650 µA	4.6 V	3.55 V	1.05 V

The oscillator die was fixed to an eight pin package and the 240 µm gate width oscillator was connected to pins of the package using gold bond wires. An external inductor of 10 µH was connected and a pressure sensor from VTI Technologies. The package with external components is shown in Figure 147.

المنارة للاستشارات
www.manaraa.com

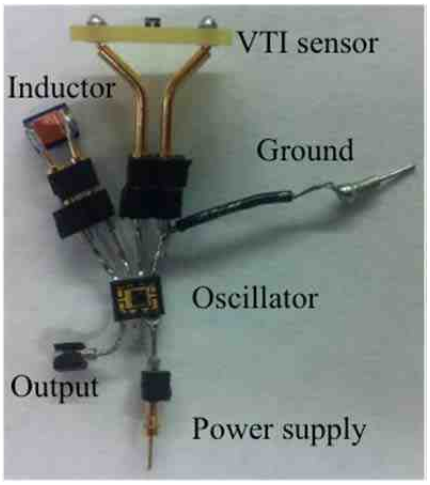

Figure 147. Oscillator in eight pin package.

The oscillator performance was tested by powering the oscillator from a DC power supply. The current was measured for different voltage levels and the output frequency was measured using a spectrum analyzer. The oscillator provided a stable output signal at a frequency of 15.3 MHz. The oscillator started at a voltage of 1.2 V and drew 74 µA. The power consumption of the oscillator is shown in Figure 148.

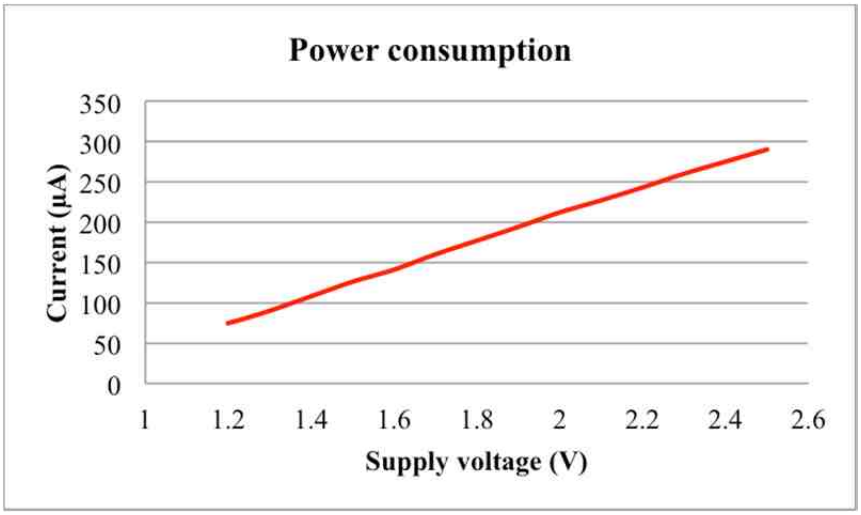

Figure 148. Colpitts oscillator power consumption.

المنارة للاستشارات
www.manaraa.com

7.2.4 System performance

Tests were performed on the packaged die with the ESA connected. A 1.5W, 915MHz signal was transmitted using the half-wave dipole antenna. The regulator was bypassed in order to get the oscillator to operate. The oscillator was powered directly from a 220µF capacitor connected at the output of the rectifier/multiplier. A variable capacitor (1 to 6pF) was connected to the oscillator to represent the pressure sensor. A 3.9µH inductor was externally connected to the relevant pins on the PGA package. The output of the oscillator was measured using a high impedance probe connected to a spectrum analyzer. The measured oscillator frequency was compared to calculated and simulated values. The simulations were performed using ADS from Agilent Technologies. Harmonic balance and transient analysis simulations were performed. The test setup is shown in Figure 149 and the measured and simulated spectra are shown in Figures 150 and 151. The results are summarized in Table 30.

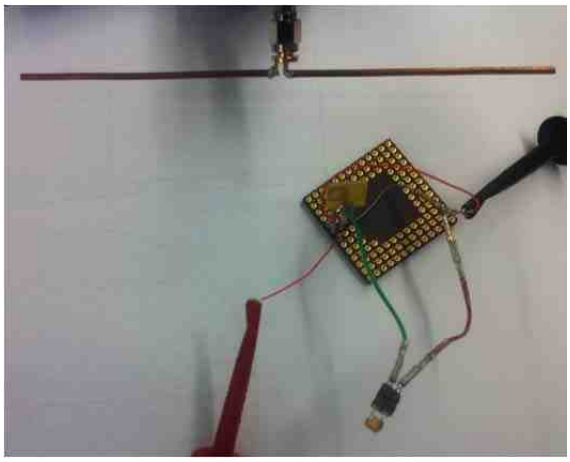

Figure 149. Oscillator powered from dipole antenna.

المنارة للاستشارات
www.manaraa.com

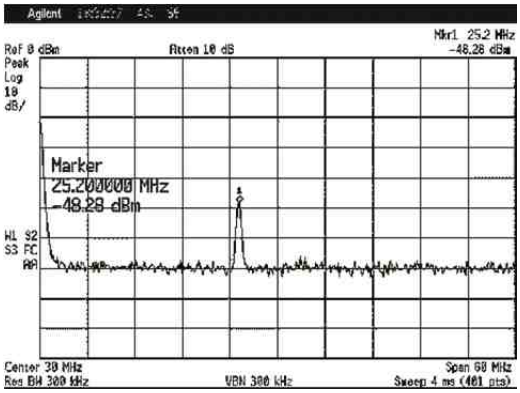

Figure 150. Measured oscillator output spectrum.

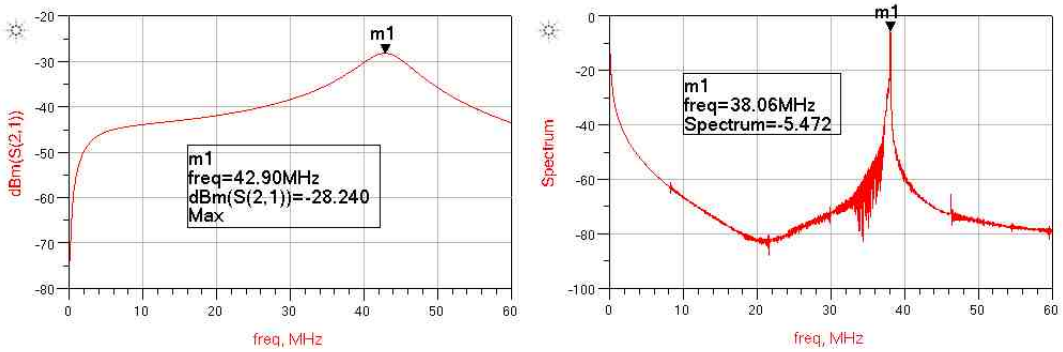

Figure 151. Simulated spectra: (a) Harmonic balance (b) Transient analysis.

Table 30. Comparison of calculated, simulated and measured oscillator frequency.

	Calculated	Simulated		Measured
		S-parameter	Transient	
Oscillator frequency – L = 3.9 µH, Var C = 3 pF, Vdd = 2 V	51 MHz	42.9 MHz	38 MHz	25.2 MHz

The measured oscillation frequency is half the calculated frequency and 50% lower than the simulated transient analysis. The calculated value did not take into account the parasitic elements associated with the layout and the package. Machado et al. observed a similar trend when designing a fully integrated Colpitts oscillator[69]. The

المنارة للاستشارات
www.manaraa.com

calculated, simulated, and measured oscillation frequencies were 850, 715, and 706 MHz respectively.

The two antennas were moved further apart and the output power of the oscillator was measured as a function of the distance between the two antennas. The output power was measured directly at the output of the oscillator using a high impedance probe connected to a spectrum analyzer. The maximum powering distance, as shown in Figure 152, was approximately 4.3cm.

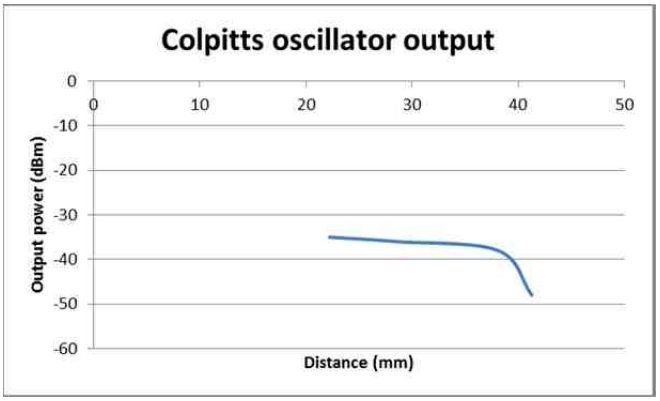

Figure 152. Colpitts oscillator output power vs range.

Two circuit dies were fixed to 8-pin surface mount packages using silver epoxy and the relevant bond pads were connected to the package connections using a ball bonder with gold bonding wire. One packaged die served as the energy harvesting block and the other served as the sensing and transmission block. The packaged dies with external connections are shown in Figure 153.

المنارة للاستشارات
www.manaraa.com

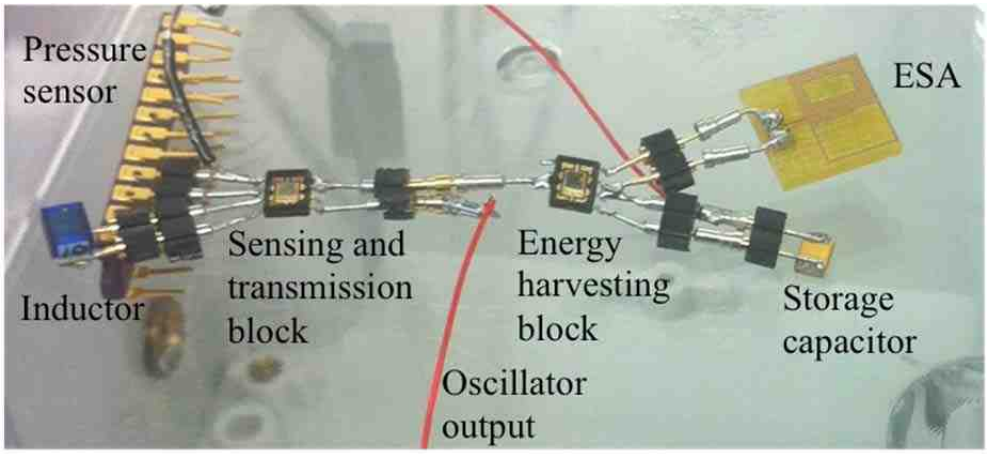

Figure 153. Final packaged die test configuration.

The oscillator was first tested as a standalone unit with power supplied by a dc power supply. A commercial pressure sensor from VTI Technologies was used. The characteristic capacitance of the pressure sensor was measured to be 11 pF at atmospheric pressure. A constant DC voltage of 2 V was supplied to power the oscillator. The frequency was measured directly at the output of the oscillator with a high impedance probe connected to a spectrum analyzer. Comparisons between the measured and theoretical values are shown in Table 31 and graphically illustrated in Figure 154. The measured oscillation frequencies were on average 30% lower than the calculated frequencies. The calculated values did not take into account the parasitic components associated with the package and die. Metal traces on the die and the package add inductive and capacitive components that change the effective component values associated with the oscillator, resulting in changes to the oscillation frequency. The parasitic component values associated with the package were not available and could not be measured with the equipment that was available in the laboratory.

المنارة للاستشارات
www.manaraa.com

Table 31. Comparison of measured and calculated oscillator frequency.

Inductance (μH)	Supply voltage (V)	Sensor capacitance	Oscillation frequency		
			Measured	Calculated	Difference
10	2	11 pF	14.3 MHz	20 MHz	5.7MHz
6.8	2	11 pF	19.3 MHz	24 MHz	4.7MHz
3.9	2	11 pF	25.8 MHz	32 MHz	6.2MHz

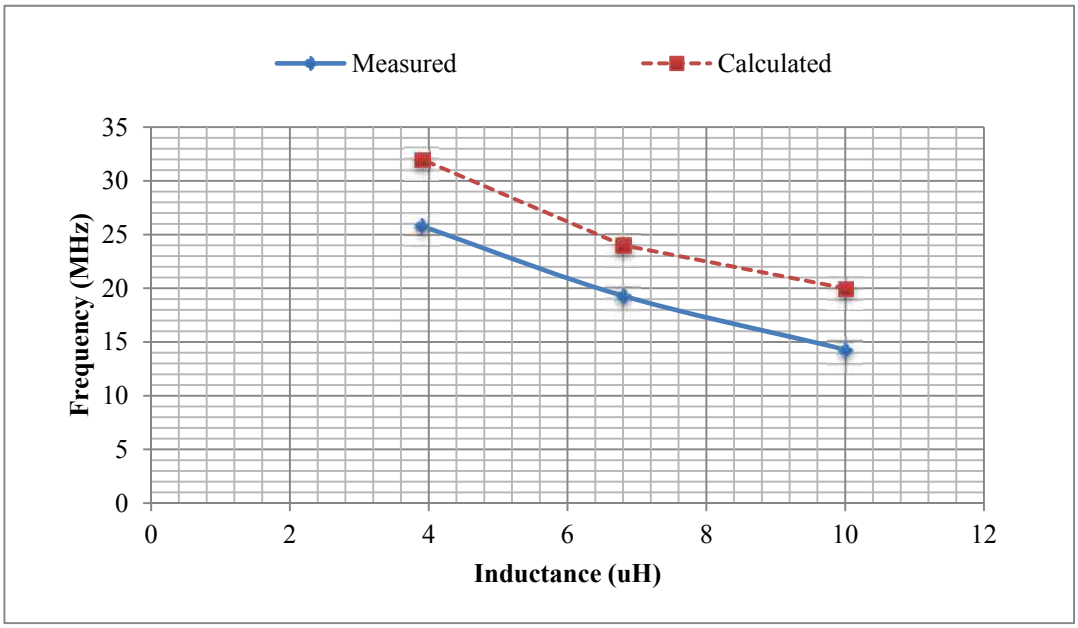

Figure 154. Comparison of calculated and measured oscillation frequencies.

Tests were performed on the complete system inside a metal container to eliminate RF interference. The oscillator was powered from the output of the RF rectifier circuit that was connected to an electrically small antenna. The regulator was bypassed since it was not able to provide a regulated voltage below 2.5 V. A 4 W signal was transmitted using a half-wave dipole antenna. The setup inside the metal container is shown in Figure 155. The oscillator failed to operate with the ESA connected to its output through the SMA connector. A single wire with a length of 11 cm was soldered to the output of the oscillator to serve as an antenna. The output signal of the oscillator was measured by placing the high impedance probe next to the wire.

المنارة للاستشارات
www.manaraa.com

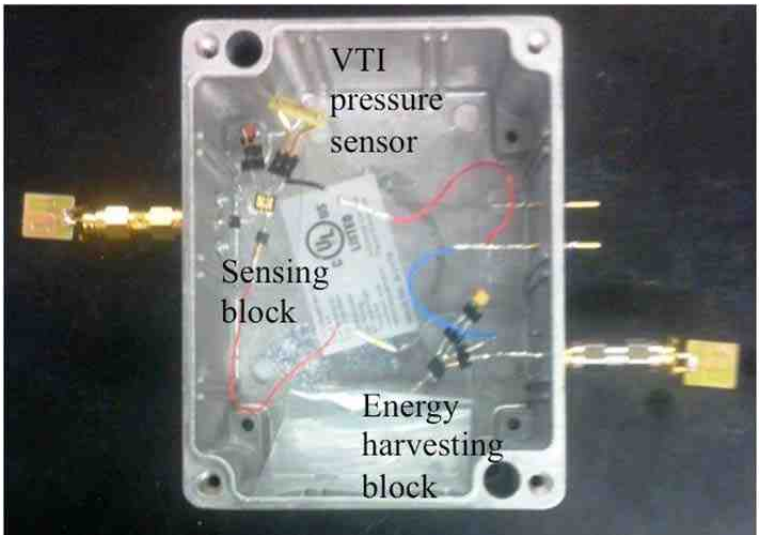

Figure 155. System test setup in metal container.

The results are given in Table 32. The transmit power was 4 W. The LC tank of the oscillator consisted of an external inductance of 10 uH and the VTI pressure sensor with a capacitance of 11 pF. The theoretical oscillation frequency is 20 MHz with these parameters. A maximum powering distance of 6.4 cm was obtained.

Table 32. Oscillation frequency and output power vs powering distance.

Powering distance (cm)	Oscillation frequency, Output Power
2.75	15.3 MHz, -42 dBm
5.5	15.3 MHz, -45 dBm
6.4	15.3 MHz, -47 dBm

The powering versus sensing range was tested using the setup shown in Figure 156. A 1.5 W, 915 MHz signal was transmitted using the dipole antenna. The oscillator output was connected to a wire with a length of 11 cm. This wire was used as the transmitting antenna of the oscillator. A coil was connected to the input of the spectrum analyzer and was used to pick up the signal from the oscillator. The oscillator output at 15.53 MHz, -60 dBm was detected at a maximum distance of 12.4 cm. The maximum distance between the transmitting antenna and the sensor was 6 cm.

المنارة للاستشارات
www.manaraa.com

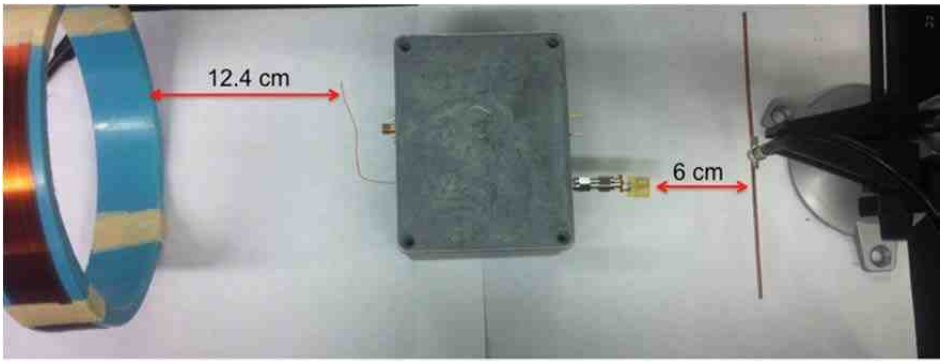

Figure 156. Test setup to determine powering and sensing range.

The results of these tests verified that the powering range is the limiting factor in the operation of RF powered telemetry systems. The metal container also served as a pressure chamber. The chamber was connected to a hand pressure-vacuum pump and the frequency versus pressure was measured. The results are shown in Figure 157. The oscillation frequency changed linearly with increasing and decreasing pressure and showed that it was possible to wirelessly power the system and measure pressure. The Pearson correlation coefficient was -0.9988, -0.9969 and -0.9993 for increasing pressure 1, decreasing pressure and increasing pressure 2 respectively. The frequency changed from 15.25 MHz at a pressure of 22 mmHg to 15 MHz at a pressure of 200 mmHg.

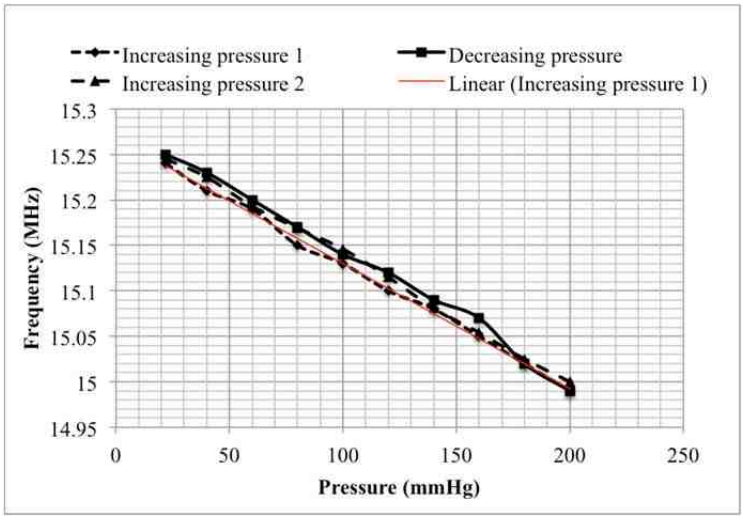

Figure 157. Oscillation frequency with changing pressure.

المنارة للاستشارات
www.manaraa.com

CHAPTER 8. CONCLUSION AND FUTURE WORK

8.1 Conclusion

A novel electrically small antenna was designed using an iterative approach based on designs found in the literature. A meander line electrically small dipole antenna provided the best performance. The design allows for tuning of the resonant frequency and input impedance of the antenna by trimming the arms of the antenna. The antenna was fabricated on FR-4 printed circuit board as shown in Figure 156.

Figure 158. Size of ESA compared to half-wave dipole and a penny.

A four-stage half-wave Dickson rectifier/multiplier circuit provided the best rectifier performance and was used to rectify the incident RF signal and multiply the DC voltage. The circuit provided a DC voltage of 1 V when connected to the ESA and powered at a distance of 20 cm. The rectifier/multiplier was connected, through a storage capacitor, to a regulator circuit. The regulator provided a 2.6 V regulated output voltage and provided good line and load regulation at this voltage. The voltage of 2.6 V was too

المنارة للاستشارات
www.manaraa.com

high to provide a usable supply voltage for the oscillator and the regulator was bypassed in the final tests to show proof-of-concept.

A Colpitts oscillator was used to sense the pressure and provide an oscillation frequency that was proportional to the pressure. This oscillator provided an oscillation frequency that changed linearly with increasing and decreasing pressure. The Colpitts oscillator also did not suffer from frequency lock-in, which is a problem in other types of oscillators. The desired operating distance of 1m was not achieved using the electrically small antenna; however, the performance of the system compares well with current state of the art systems as illustrated in Table 33. An operating distance in excess of 1 m was achieved using a half-wave dipole antenna as the sensor antenna.

Table 33. Comparison with current state of the art.

Ref	**Reader Freq**	**Sensor antenna and size**	**Technology**	**Reader power, Range**	
[20]	5.8 GHz	On chip antenna at 5.8 GHz. *(ka=0.36)*	180 nm CMOS	4 W, 7.5 cm	
[22]	3 GHz	LTCC loop: 6 mm x 3 mm (*Scaled from Figure*) (*ka* = 0.38)	130 nm CMOS	1.5 W, 5 cm	
[19]	2.4 GHz	1 cm diameter loop (*ka=0.5*)	130 nm CMOS	1.5 cm, 40 mW	
[70]	915 MHz	Impinj button 9 mm diameter (*ka=0.17*)	Not stated	4 W assumed – max output of Impinj reader 12 cm – correspondence with author	
This work	915 MHz	ESA: 7 mm x 10 mm (*ka*=0.19)	500 nm CMOS	1.5 W, 5.4 cm	4 W, 6.4 cm
	Half-wave dipole antenna used as sensor antenna to compare with performance of ESA			1.5 W, 41 cm	4 W, 104 cm

المنارة للاستشارات
www.manaraa.com

8.2 Future work

Investigating and implementing several changes can improve the RFID-based telemetry system. The first would be to have the complete system on only one IC die. This should also include the inductor that is currently not on the chip. Further research into the design and fabrication of planar spiral IC inductors is needed to successfully implement an oscillator design with an on-chip inductor.

The oscillator circuit should be optimized to operate at a lower supply voltage and current. This should be possible by increasing the gate width of the transistor even further and making use of another fabrication process through the MOSIS service. Machado et al. [69]have shown that is possible to implement a fully integrated 800 MHz Colpitts oscillator using the 130 nm CMOS process from IBM through MOSIS. The oscillator is able to operate at a supply voltage as low as 100 mV.

Lowering the junction voltage of the Schottky diodes that are used in the rectifier/multiplier circuits should be investigated. A reduction in the junction voltage can be achieved using a different fabrication process. The leakage current of the diodes should also be minimized.

The efficiency of the electrically small antenna can be improved. More accurate simulations should be attempted and different configurations can be investigated. Usage of genetic algorithms should be considered. Different substrates can also be explored for fabrication of the antenna.

المنارة للاستشارات
www.manaraa.com

REFERENCES

[1] J. Aebersold, Jackson, D., Crain, M., Naber, J., Kaplan, H., Roussel, T., M., Keynton, R., Walsh, K., Van der Pol, P., Tezel, G., "Development of a RFID-based Wireless Pressure Sensing Prototype to Prevent the Progression of Glaucoma," presented at the ARVO Annual Meeting, 2008.

[2] A. M. Sodagar, K. D. Wise, and K. Najafi, "A Wireless Implantable Microsystem for Multichannel Neural Recording," *Microwave Theory and Techniques, IEEE Transactions on,* vol. 57, pp. 2565-2573, 2009.

[3] S. K. Kelly, D. B. Shire, C. Jinghua, P. Doyle, M. D. Gingerich, W. A. Drohan*, et al.*, "Realization of a 15-channel, hermetically-encased wireless subretinal prosthesis for the blind," in *Engineering in Medicine and Biology Society, 2009. EMBC 2009. Annual International Conference of the IEEE*, 2009, pp. 200-203.

[4] J. T. Lin, D. Jackson, J. Aebersold, K. M. Walsh, J. Naber, and W. Hnat, "A High Gauge Factor Capacitive Strain Sensor and its Telemetry Application in Biomechanics," in *University/Government/Industry Micro/Nano Symposium, 2008. UGIM 2008. 17th Biennial*, 2008, pp. 98-101.

[5] M. M. Ahmadi and G. A. Jullien, "A Wireless-Implantable Microsystem for Continuous Blood Glucose Monitoring," *Biomedical Circuits and Systems, IEEE Transactions on,* vol. 3, pp. 169-180, 2009.

[6] E. Y. Chow, A. L. Chlebowski, S. Chakraborty, W. J. Chappell, and P. P. Irazoqui, "Fully Wireless Implantable Cardiovascular Pressure Monitor Integrated with a Medical Stent," *Biomedical Engineering, IEEE Transactions on,* vol. 57, pp. 1487-1496, 2010.

[7] E. Y. Chow, A. L. Chlebowski, and P. P. Irazoqui, "A Miniature-Implantable RF-Wireless Active Glaucoma Intraocular Pressure Monitor," *Biomedical Circuits and Systems, IEEE Transactions on,* vol. 4, pp. 340-349, 2010.

[8] F. Graichen, R. Arnold, A. Rohlmann, and G. Bergmann, "Implantable 9-Channel Telemetry System for In Vivo Load Measurements With Orthopedic Implants," *Biomedical Engineering, IEEE Transactions on,* vol. 54, pp. 253-261, 2007.

المنارة للاستشارات
www.manaraa.com

[9] T. Kakaday, A. W. Hewitt, N. H. Voelcker, J. S. Li, and J. E. Craig, "Advances in telemetric continuous intraocular pressure assessment," *Br J Ophthalmol,* vol. 93, pp. 992-6, Aug 2009.

[10] W. L. Stutzman, *Antenna Theory and Design*, 2 ed. New York: John Wiley & Sons, 1998.

[11] C. C. Collins, "Miniature Passive Pressure Transensor for Implanting in the Eye," *Biomedical Engineering, IEEE Transactions on,* vol. BME-14, pp. 74-83, 1967.

[12] R. Want, "An introduction to RFID technology," *Pervasive Computing, IEEE,* vol. 5, pp. 25-33, 2006.

[13] C. A. Balanis, *Antenna theory: analysis and design*: John Wiley, 2005.

[14] K. Opasjumruskit, T. Thanthipwan, O. Sathusen, P. Sirinamarattana, P. Gadmanee, E. Pootarapan*, et al.*, "Self-powered wireless temperature sensors exploit RFID technology," *Pervasive Computing, IEEE,* vol. 5, pp. 54-61, 2006.

[15] F. Kocer and M. P. Flynn, "A new transponder architecture with on-chip ADC for long-range telemetry applications," *Solid-State Circuits, IEEE Journal of,* vol. 41, pp. 1142-1148, 2006.

[16] U. Karthaus and M. Fischer, "Fully integrated passive UHF RFID transponder IC with 16.7 microW minimum RF input power," *Solid-State Circuits, IEEE Journal of,* vol. 38, pp. 1602-1608, 2003.

[17] A. Vaz, A. Ubarretxena, I. Zalbide, D. Pardo, H. Solar, A. Garcia-Alonso*, et al.*, "Full Passive UHF Tag With a Temperature Sensor Suitable for Human Body Temperature Monitoring," *Circuits and Systems II: Express Briefs, IEEE Transactions on,* vol. 57, pp. 95-99, 2010.

[18] R. Kubendran, H. Krishnan, B. Manola, S. W. M. John, W. J. Chappell, and P. P. Irazoqui, "A generic miniature multi-feature programmable wireless powering headstage ASIC for implantable biomedical systems," in *Engineering in Medicine and Biology Society,EMBC, 2011 Annual International Conference of the IEEE*, 2011, pp. 5617-5620.

[19] S. Yi-Chun, S. Tueng, and B. P. Otis, "A 2.3 uW Wireless Intraocular Pressure/Temperature Monitor " *Solid-State Circuits, IEEE Journal of,* vol. 46, pp. 2592-2601, 2011.

[20] S. Radiom, M. Baghaei-Nejad, G. Vandenbosch, Z. Li-Rong, and G. Gielen, "Far-field RF powering system for RFID and implantable devices with monolithically integrated on-chip antenna," in *Radio Frequency Integrated Circuits Symposium (RFIC), 2010 IEEE*, 2010, pp. 113-116.

[21] F. Kocer and M. P. Flynn, "An RF-powered, wireless CMOS temperature sensor," *Sensors Journal, IEEE,* vol. 6, pp. 557-564, 2006.

المنارة للاستشارات
www.manaraa.com

[22] E. Y. Chow, Y. Chin-Lung, O. Yuehui, A. L. Chlebowski, P. P. Irazoqui, and W. J. Chappell, "Wireless Powering and the Study of RF Propagation Through Ocular Tissue for Development of Implantable Sensors," *Antennas and Propagation, IEEE Transactions on,* vol. 59, pp. 2379-2387, 2011.

[23] J. P. Curty, N. Joehl, F. Krummenacher, C. Dehollain, and M. J. Declercq, "A model for micro-power rectifier analysis and design," *Circuits and Systems I: Regular Papers, IEEE Transactions on,* vol. 52, pp. 2771-2779, 2005.

[24] J. P. Curty, N. Joehl, C. Dehollain, and M. J. Declercq, "Remotely powered addressable UHF RFID integrated system," *Solid-State Circuits, IEEE Journal of,* vol. 40, pp. 2193-2202, 2005.

[25] C. Occhiuzzi, G. Contri, and G. Marrocco, "Design of Implanted RFID Tags for Passive Sensing of Human Body: The STENTag," *Antennas and Propagation, IEEE Transactions on,* vol. 60, pp. 3146-3154, 2012.

[26] L. J. Chu, "Physical Limitations of Omni-Directional Antennas," *Journal of Applied Physics,* vol. 19, pp. 1163-1175, 1948.

[27] H. A. Wheeler, "Fundamental Limitations of Small Antennas," *Proceedings of the IRE,* vol. 35, pp. 1479-1484, 1947.

[28] G. Marrocco, A. Fonte, and F. Bardati, "Evolutionary design of miniaturized meander-line antennas for RFID applications," in *Antennas and Propagation Society International Symposium, 2002. IEEE*, 2002, pp. 362-365 vol.2.

[29] G. Marrocco, "Gain-optimized self-resonant meander line antennas for RFID applications," *Antennas and Wireless Propagation Letters, IEEE,* vol. 2, pp. 302-305, 2003.

[30] S. R. Best and J. D. Morrow, "On the significance of current vector alignment in establishing the resonant frequency of small space-filling wire antennas," *Antennas and Wireless Propagation Letters, IEEE,* vol. 2, pp. 201-204, 2003.

[31] K. Gosalia, M. S. Humayun, and G. Lazzi, "Impedance Matching and Implementation of Planar Space-Filling Dipoles as Intraocular Implanted Antennas in a Retinal Prosthesis," *Antennas and Propagation, IEEE Transactions on,* vol. 53, pp. 2365-2373, 2005.

[32] E. Jordan and K. Balmain, *Electromagnetic Waves and Radiating Systems*. New York: Prentice-Hall, 1968.

[33] V. F. Fusco, *Foundations of Antenna Theory and Techniques*: Pearson Prentice-Hall, 2005.

[34] C. Yawen, M. Q. H. Meng, K. L. Wu, and W. Xiaona, "Experimental Study of Radiation Efficiency from an Ingested Source inside a Human Body Model[*]," in *Engineering in Medicine and Biology Society, 2005. IEEE-EMBS 2005. 27th Annual International Conference of the*, 2005, pp. 7754-7757.

المنارة للاستشارات
www.manaraa.com

[35] J. F. Naber, "Range of commercial RFID devices," *Private communication,* 2010.

[36] K. Gosalia, G. Lazzi, and M. Humayun, "Investigation of a microwave data telemetry link for a retinal prosthesis," *Microwave Theory and Techniques, IEEE Transactions on,* vol. 52, pp. 1925-1933, 2004.

[37] C. Coleman, *An Introduction to Radio Frequency Engineering*. New York: Cambridge University Press, 2004.

[38] C. Paul, *Electromagnetics for Engineers*. New York: J. Wiley & Sons, 2004.

[39]. *Dielectric properties of body tissues*. Available: http://niremf.ifac.cnr.it/tissprop

[40] P. V. Nikitin and K. V. S. Rao, "Performance limitations of passive UHF RFID systems," in *Antennas and Propagation Society International Symposium 2006, IEEE*, 2006, pp. 1011-1014.

[41] R. C. Hansen, *Electrically Small, Superdirective, and Superconducting Antennas*: John Wiley & Sons, 2006.

[42] R. E. Collin and S. Rothschild, "Evaluation of antenna Q," *Antennas and Propagation, IEEE Transactions on,* vol. 12, pp. 23-27, 1964.

[43] J. S. McLean, "A re-examination of the fundamental limits on the radiation Q of electrically small antennas," *Antennas and Propagation, IEEE Transactions on,* vol. 44, p. 672, 1996.

[44] A. K. Skrivervik, J. F. Zurcher, O. Staub, and J. R. Mosig, "PCS antenna design: the challenge of miniaturization," *Antennas and Propagation Magazine, IEEE,* vol. 43, pp. 12-27, 2001.

[45] S. E. Sussman-Fort and R. M. Rudish, "Non-Foster Impedance Matching of Electrically-Small Antennas," *Antennas and Propagation, IEEE Transactions on,* vol. 57, pp. 2230-2241, 2009.

[46] N. Tesla, "Experiments with Alternate Currents of Very High Frequency and their Application to Methods of Artificial Illumination," *American Institute of Electrical Engineers, Transactions of the,* vol. VIII, pp. 266-319, 1891.

[47] G. De Vita and G. Iannaccone, "Design criteria for the RF section of UHF and microwave passive RFID transponders," *Microwave Theory and Techniques, IEEE Transactions on,* vol. 53, pp. 2978-2990, 2005.

[48] S. Mandal and R. Sarpeshkar, "Low-Power CMOS Rectifier Design for RFID Applications," *Circuits and Systems I: Regular Papers, IEEE Transactions on,* vol. 54, pp. 1177-1188, 2007.

[49] A. Faul, M. Turner, and J. Naber, "Implantable wireless microsystems for the measurement of intraocular pressure," in *Circuits and Systems (MWSCAS), 2011 IEEE 54th International Midwest Symposium on*, 2011, pp. 1-4.

المنارة للاستشارات
www.manaraa.com

[50] B. Razavi, *RF Microelectronics*: Prentice Hall, 1998.

[51] B. Razavi, *Fundamentals of Microelectronics*: Wiley, 2006.

[52] I. Balaz, Z. Brezovic, M. Minarik, V. Kudjak, and V. Stofanik, "Barkhausen criterion and another necessary condition for steady state oscillations existence," in *Radioelektronika (RADIOELEKTRONIKA), 2013 23rd International Conference*, 2013, pp. 151-155.

[53] R. Adler, "A study of locking phenomena in oscillators," *Proceedings of the IEEE,* vol. 61, pp. 1380-1385, 1973.

[54] B. Razavi, "A study of injection pulling and locking in oscillators," in *Custom Integrated Circuits Conference, 2003. Proceedings of the IEEE 2003*, 2003, pp. 305-312.

[55] L. Xiaolue and J. Roychowdhury, "Analytical equations for predicting injection locking in LC and ring oscillators," in *Custom Integrated Circuits Conference, 2005. Proceedings of the IEEE 2005*, 2005, pp. 461-464.

[56] K. Finkenzeller, *RFID Handbook*, 2 ed.: Wiley, 2003.

[57] B. van der Pol, "The Nonlinear Theory of Electric Oscillations," *Proceedings of the IRE,* vol. 22, pp. 1051-1086, 1934.

[58] B. Mesgarzadeh and A. Alvandpour, "A study of injection locking in ring oscillators," in *Circuits and Systems, 2005. ISCAS 2005. IEEE International Symposium on*, 2005, pp. 5465-5468 Vol. 6.

[59] R. J. Baker, *CMOS Circuit Design, Layout and Simulation*, 2 ed.: Wiley-Interscience, 2005.

[60] R. D. Middlebrook, "Measurement of loop gain in feedback systems," *Int. J. Electronics,* vol. 38, p. 27, 1975.

[61]. *The MOSIS Service*. Available: http://www.mosis.com/

[62]. *Bausch & Lomb, Inc.* Available: http://www.bausch.com

[63] E. L. Holzman, "Wideband measurement of the dielectric constant of an FR4 substrate using a parallel-coupled microstrip resonator," *Microwave Theory and Techniques, IEEE Transactions on,* vol. 54, pp. 3127-3130, 2006.

[64] O. Staub, J. F. Zürcher, and A. Skrivervik, "Some considerations on the correct measurement of the gain and bandwidth of electrically small antennas," *Microwave and Optical Technology Letters,* vol. 17, pp. 156-160, 1998.

[65]. *Integrated Spiral Inductor Calculator*. Available: http://www-smirc.stanford.edu/spiralCalc.html

المنارة للاستشارات
www.manaraa.com

[66] H. Nakamoto, D. Yamazaki, T. Yamamoto, H. Kurata, S. Yamada, K. Mukaida*, et al.*, "A Passive UHF RF Identification CMOS Tag IC Using Ferroelectric RAM in 0.35-μm Technology," *Solid-State Circuits, IEEE Journal of,* vol. 42, pp. 101-110, 2007.

[67] M. J. Turner, "Development of a wireless microsystem for the episcleral measurement of intraocular pressure," Ph.D. dissertation, Electrical and Computer Engineering, University of Louisville, Louisville, 2010.

[68] W. Stallings, *Wireless Communications and Networks*, Second ed.: Pearson, 2005.

[69] M. B. Machado, M. C. Schneider, and C. Galup-Montoro, "Design of a Fully Integrated Colpitts Oscillator Operating at Vdd below 4kT/q," in *presented at Circuits and Systems (LASCAS), 2014 5th IEEE Latin American Symposium on*, Feb. 2014.

[70] X. Qing, Z. N. Chen, and C. K. Goh, "UHF near-field RFID reader antenna with capacitive couplers," *Electronics Letters,* vol. 46, pp. 1591-1592, 2010.

المنارة للاستشارات
www.manaraa.com

CURRICULUM VITAE

André J. Faul
5400 Tarrant Lane
Crestwood KY, 40014
502-852-0131 (office)
502-930-5447 (cell)
andre.faul@louisville.edu

EDUCATION

PhD - Electrical Engineering University of Louisville, Louisville, KY Dissertation Topic – Next Generation RFID Telemetry Design for Biomedical Implants.	*2014*
BEng Hons (Electronic Engineering) University of Pretoria, Pretoria, South Africa Courses: Ionospheric Propagation, VHF and UHF Propagation, Microwave Antennae, Applied Reliability Engineering, Process Automation, Bio-systems, Introduction to Radar Systems, Opto-electronics	*1987*
BEng (Electronic Engineering) University of Pretoria, Pretoria, South Africa	*1983*

EMPLOYMENT HISTORY

Instructor, Term Department of Electrical and Computer Engineering, Speed School of Engineering, University of Louisville, Louisville, KY	*Oct 2001 - current*
Director Encon Engineering Projects, Pretoria, South Africa.	*May 1998- Sept 2000*
Associate Encon Engineering Projects, Pretoria, South Africa.	*Jun 1996- April 1998*
Senior Engineer Raath and Van Zyl Consulting Engineers, Pretoria, South Africa	*Oct 1989- May 1996*

المنارة للاستشارات
www.manaraa.com

Senior Engineer Grinaker Systems Technologies, Pretoria, South Africa	*Feb 1989-* *Sept 1989*
Engineer Van Themaat, Raath & Van Zyl Consulting Engineers, Pretoria, South Africa	*Sept 1986-* *Jan 1989*
Engineer Department of Posts and Telecommunications, South African Government, Pretoria, South Africa	*Jan 1985-* *Aug 1986*
Officer with the rank of Lieutenant Signal Corp, South African Defence Force	*Jan 1983-* *Dec 1984*

Honors

Eta Kappa Nu Honour Society	*2004*
Golden Key International Honour Society	*2006*
Thomas Murray Outstanding ECE Teaching Award	*2011*

CAREER EXPERIENCE

Department of Electrical and Computer Engineering, Speed Engineering School, University of Louisville, Louisville, KY

Teaching	Taught the following courses: • Communications and Modulation and Lab(ECE550/551) • Communications and Modulation and Lab(EE470/475). This is a distance course delivered to Western Kentucky University via Interactive TV. • Instrumentation Electronics and Lab (ECE535/536) • Network Analysis II (ECE320) • Electronics I and Lab(ECE333/334) • Logic Design and Lab(ECE210/211) • Introduction to Electrical Engineering (ECE252) • Capstone Design in ECE;CUE (ECE497) Changed all courses to web-assisted courses and designed the web sites for each with Blackboard technology.
Service – ECE Department	• Served on the Subcommittee on Measurement
Research	• PhD dissertation: Next Generation RFID Telemetry Designs for Biomedical Implants. The goal of this work is to extend the range of current Radio Frequency Identification (RFID) based telemetry systems for wireless monitoring of physiological parameters in humans and animals. It is proposed that the range can be increased to over 100cm by developing a much higher frequency RFID telemetry system. • Independent study – Control and data collection of an Artificial Vasculature Device using Labview.

المنارة للاستشارات
www.manaraa.com

Consulting Work	• Served as consultant to the Louisville Metro Council on the acquisition and implementation of a Public Safety Radio Communication System (2005 – 2006) • Consulting Engineer: Consulting work involved design of and project management for the implementation of access control, perimeter security and radio communication systems. (Sept. 1986 – Sept. 2000)
Grants Awarded	• Co-Investigator: Next Generation RFID Telemetry Designs for Biomedical Implants. Clinical and Translational Science Pilot Grant Program (Basic Translational) - $50,000.00. PI: Dr. John Naber. (May 2010 – May 2011)

Encon Engineering Projects, Pretoria, South Africa

Consulting Engineering	Was responsible for electronic projects and electronic sections of multi-disciplinary projects. The work comprised a wide spectrum and included the following elements: • Reporting to and negotiating with clients. • Identification and formulation of problems. Analysis of factors that might have practical, economical, social or statutory implications. • Detail design of multi-million dollar electronic security systems (including data acquisition and central control), access control systems and radio communication systems, writing specifications, creating drawings, compiling tender documents and cost estimates. Technologies implemented included Closed Circuit TV, microwave fences, active infrared barriers, short circuit and non-lethal shock fences, taut-wire detection fences and fiber-optic data and video communications. • Execution of projects, i.e. construction, operation and maintenance. Decision-making regarding the effective use of people, materials, machinery and other resources.

المنارة للاستشارات
www.manaraa.com

Project Management	Project involvement included the following: • Defence Headquarters - Access control system. Design. • Mossgas Synfuels - Security and access control system. Vertical deployment of security system (microwave detection and non-lethal shock fence) on wall structure. Project value in excess of $3,000,000.00. Design, supervision during installation, acceptance testing. • Johannesburg International Airport Fuel Depot - Security system (active infrared detection, data communication). Design, supervision during installation, acceptance testing. • Six major oil depots - Design of security system, supervision during installation, acceptance testing. Total project value $5,000,000.00 • Eastern Cape Provincial Administration - Radio communication network planning and maintenance management. Involved the design and implementation of a VHF system that was linked using UHF repeaters to cover an area of approximately 150,000 km^2. • Johannesburg and Durban International Airports - Design of security and access control systems, supervision during installation, acceptance testing. • Seven Army Depots - Design of security systems, supervision during installation, acceptance testing and maintenance management. Total project value $8,000,000.00. • Defence Force Ammunition Depots - Development of maintenance plan for security systems, maintenance management. • Lonrho Platinum Mine - Project management and quality control of integrated security management system. Project value $3,500,000.00.

Grinaker Systems Technologies

Engineering Design	• Did detail design and manufacture of an antenna-switching matrix. The unit had to be capable of switching up to eight antennae to any of up to twelve transceivers and covered the frequency band from 3MHz to 1200MHz. • Was responsible for giving system-engineering inputs in compliance with MIL-standards (USA) for various projects. These inputs included configuration management, quality control, project planning and preparation of acceptance test procedures

المنارة للاستشارات
www.manaraa.com

	Van Themaat, Raath and Van Zyl Consulting Engineers
Consulting Engineering	Was responsible to the Director: Electronics for certain electronic projects and electronic sub-sections of multi-disciplinary projects. The work comprised a wide spectrum and included the following elements: • Reporting to and negotiating with clients. • Identifying and formulating of problems. Analysis of factors that might have practical, economical, social or statutory implications. • Detail design multi-million dollar electronic security systems (including data acquisition and central control) and access control systems, writing specifications, creating drawings, compiling tender documents and cost estimates. • Execution of projects, e.g. construction, operation and maintenance. Decision-making regarding the effective use of people, materials, machinery and other resources. • Project management.
	Involvement in projects included the following: • Project Herder - Security and access control systems for two Air Force Bases. • Development Bank - Access control system. • Transvaal Provincial Administration Head Office - Access control system. • Rand Water Board Head Office - Access control system. • Rand Water Board Pump Station - Security and access control system. • Appointed as site agent at an Air Force Base from May 1988 to January 1989 to supervise the supply, installation, commissioning and maintenance of a security and access control system. The total contract value was $1,200,000.00. Responsibilities included the following: • General site supervision. • Technical inputs and approval of technical changes and financial variations. • Preparation of progress reports and invoices

المنارة للاستشارات
www.manaraa.com

Department of Posts and Telecommunications

Electrical Engineering	• Basic orientation program took place from January 1985 to July 1985. During this period a database was developed that was used as a planning aid for the installation of new electronic telephone exchanges. • Appointed as Engineer: Diginet and Data Test Centers in August 1985. Responsible for the operation and administration of data test centers in the Northern Transvaal Region. Supervise the general functioning of the Data Test centers; define repair priorities and client liaison with regard to data service problems. • Responsible for the planning and commissioning of a digital data-switching network in the Northern Transvaal Region. This included supervision of the installation of new equipment, co-ordination of the awarding of data links and supervision of two senior technicians and technicians.

South African Defence Force

Signals Officer	Basic training took twelve weeks after which the "R9 Advanced Course" followed. The course consisted of two parts, i.e. Tactical Communications Equipment and Mobile Command and Control Equipment. The course included theoretical and practical aspects of tactical HF and VHF communication equipment, voice and data.
	Signals Officers course started in August 1983. The course focussed on command and control skills, leadership, management and military science. Commission with the rank of lieutenant followed after successful completion of the course.
	Appointed as Signals Officer at 5 Reconnaissance Regiment in December 1983 and commanded a staff complement of twenty-two people. Duties included the following: • Control and co-ordination of all activities regarding radio communication in the Unit. General administration, merit rating and primary supervision. • Allocating frequencies for VHF communication. • Determining suitable frequencies for 24 hour HF communication. This was done by using ionospheric propagation profiles as supplied by the CSIR (Council for Scientific and Industrial Research). • Allocation of suitable call signs and code names. Training of staff. This training comprised the use of communication equipment as well as the basic principles of radio communication.

المنارة للاستشارات
www.manaraa.com

Publications

Peer Reviewed Publications
A.J. Faul and J.F. Naber, "Design and Test of a 915MHz, RFID-based Pressure Sensor for Glaucoma" in *Circuits and Systems (LASCAS), 2014 5th IEEE Latin American Symposium on, 2014.*
A. J. Faul, D. Jackson and J.F. Naber, "Analysis of frequency lock-in using integrated colpitts and multivibrator oscillators for RFID-based telemetry," in *Circuits and Systems (MWSCAS), 2010 53rd IEEE International Midwest Symposium on*, 2010, pp. 422-425
Peer Reviewed Presentations
A. J. Faul, D. Jackson and J.F. Naber, "Analysis of frequency lock-in using integrated colpitts and multivibrator oscillators for RFID-based telemetry." Poster presented at the 53rd IEEE International Midwest Symposium on Circuits and Systems (MWSCAS), Seattle, WA, Aug 2010
Invited Publications
Faul, A., M. Turner, and J. Naber, "Implantable wireless microsystems for the measurement of intraocular pressure" in *Circuits and Systems (MWSCAS), 2011 IEEE 54th International Midwest Symposium on*. 2011.

Professional Memberships

Institute of Electrical and Electronics Engineers - IEEE	*Current*
South African Association of Consulting Engineers – SAACE	*1996-2001*
South African Institute of Electrical Engineers – SAIEI	*1986-2001*
Engineering Council of South Africa - ECSA (previously the South African Council for Professional Engineers)	*1990-2001*

المنارة للاستشارات
www.manaraa.com